Experimental Modeling of Group 5 Metal Oxide Catalysts

von Diplom-Chemiker

Alexander Hermann Horst Uhl

aus Saarbrücken

von der Fakultät II - Mathematik und Naturwissenschaften
der Technischen Universität Berlin
zur Erlangung des akademischen Grades

Doktor der Naturwissenschaften
- Dr. rer. nat. -

genehmigte Dissertation

Promotionsausschuss:

Vorsitzender:	Prof. Dr. Reinhard Schomäcker
Gutachter:	Prof. Dr. Dres. h.c. mult. Helmut Schwarz
Gutachter:	Prof. Dr. Hans-Joachim Freund
Gutachter:	Prof. Dr. Christian Limberg

Tag der wissenschaftlichen Aussprache: 29. September 2008

Berlin 2008
D 83

What's the frequency, Kenneth?
(R.E.M., 1994)

Abstract

The aim of this work is to study relevant heterogeneous catalysts, namely the oxides of niobium and vanadium. Using the surface science approach, well-defined models can be prepared and investigated at the atomic level. Experimental methods comprise infrared spectroscopy, thermal desorption spectroscopy, scanning tunneling microscopy, photoelectron spectroscopy, and low energy electron diffraction. Niobia model catalysts prepared within this work include niobia films grown on $Cu_3Au(100)$, niobia-supported cobalt, and alumina-supported niobia. The niobia monolayer reveals a sandwich structure, where niobium cations are surrounded by a bottom and a top oxygen layer, yielding a stoichiometry of Nb_2O_5. A bridging oxygen termination was found for the monolayer, while the multilayer films exhibit niobyl groups. Cobalt exhibits a strong interaction with niobia, including eventual migration into the film. This strong metal-support interaction is a typical property of niobia. However, both terminations are found to coexist for alumina-supported niobia particles. In general, the results are very similar to those previously found for alumina-supported vanadia. The second system investigated is ceria-supported vanadia. Structural results comprise a coverage-dependence of the oxidation state of vanadium and of the vanadyl stretching vibration. Due to a strong interaction with ceria, vanadia is fully dispersed as VO_4 monomers at low coverage. The results of a subsequent reactivity study with respect to the oxidative dehydrogenation of methanol are discussed on this basis. In particular, the VO_4 monomer is identified as the origin of the methanol-to-formaldehyde conversion at a temperature as low as 340 K.

Kurzzusammenfassung

Die vorliegende Arbeit widmet sich der Untersuchung wichtiger heterogener Katalysatoren, namentlich den Oxiden von Niob und Vanadium. Mittels des sogenannten Surface-Science-Approach können wohldefinierte Modelle präpariert und auf atomarer Ebene untersucht werden. Die experimentellen Methoden umfassen Infrarotspektroskopie, Thermische Desorptionsspektroskopie, Rastertunnelmiktroskopie, Photoelektronenspektroskopie und niederenergetische Elektronenbeugung. Die hier präparierten Nioboxid-Modellkatalysatoren umfassen auf $Cu_3Au(100)$ gewachsene Nioboxid-Filme, auf Nioboxid geträgertes Cobalt und auf Aluminiumoxid geträgertes Nioboxid. Die Nioboxid-Monolage weist eine Sandwich-Struktur auf, in der die NiobKationen von einer unteren und einer oberen Sauerstoff-Schicht eingerahmt sind, so dass sich die Stöchiometrie zu Nb_2O_5 ergibt. Die Sauerstoff-Terminierung hat sich als verbrückend gezeigt, während die Multilagen-Filme Niobyl-Gruppen aufweisen. Cobalt zeigt eine starke Wechselwirkung mit Nioboxid, einschließlich einer Migration in den Film. Diese starke Metall-Substrat-Wechselwirkung ist eine typischen Eigenschaft von Nioboxid. Allerdings wurde für auf Aluminiumoxid geträgertes Nioboxid eine Koexistenz beider Terminierungen gefunden. Das zweite untersuchte System ist auf Ceroxid geträgertes Vanadiumoxid. Die Struktur-Ergebnisse schließen eine Bedeckungsabhängigkeit des Oxidationszustands von Vanadium und der Vanadyl-Streckschwingung ein. Aufgrund einer starken Wechselwirkung mit Ceroxid ist Vanadiumoxid bei geringer Bedeckung vollständig dispergiert als VO_4-Monomere. Die Ergebnisse der anschließenden Reaktivitätsstudie hinsichtlich der oxidativen Dehydrierung werden auf dieser Grundlage diskutiert. Insbesondere wird das VO_4-Monomer als die Ursache eines Umsatzes von Methanol zu Formaldehyd bereits bei 340 K identifiziert.

Contents

1 Introduction **1**

2 Experimental **7**

2.1 Apparatus 7
2.2 Sample Preparation 9
2.3 Low Energy Electron Diffraction 11
2.4 Photo- and Auger Electron Spectroscopy 13
2.5 Scanning Tunneling Microscopy 15
2.6 Infrared Spectroscopy 17
2.6.1 Physical Principles of Infrared Spectroscopy 17
2.6.2 The Fourier-Transform Spectrometer 21
2.6.3 Infrared Spectroscopy on Surfaces 23
2.7 Electron Energy Loss Spectroscopy 28
2.8 Temperature Programmed Desorption 31

3 Niobia Films as Oxide Support **35**

3.1 Monolayer Niobia Films 36
3.1.1 Preparation 36
3.1.2 Results and Discussion 36
3.1.3 Conclusions 47
3.2 Niobia Multilayer Films 48
3.2.1 Preparation 49
3.2.2 Results and Discussion 49
3.2.3 Conclusions 52
3.3 Cobalt Supported on Monolayer Niobia Films 54
3.3.1 Preparation 54
3.3.2 Results and Discussion 54
3.3.3 Conclusions 60

4 Supported Niobia Particles **61**
4.1 Preparation 61
4.2 Results and Discussion 62
4.2.1 STM 62
4.2.2 IRAS 64
4.2.3 Thermal Stability 66
4.3 Conclusions 70

5 Vanadia Supported on Ceria Films **71**
5.1 Literature Review 71
5.1.1 Ceria Films 71
5.1.2 Structure of Supported Vanadia 73
5.1.3 Methanol Oxidation 75
5.2 Preparation 79
5.3 Characterization of the Ceria Films 79
5.3.1 LEED and STM 79
5.3.2 PES 79
5.3.3 IRAS 81
5.4 Results and Discussion 83
5.4.1 Structure of Vanadia/Ceria 83
5.4.2 Methanol Oxidation 95
5.5 Conclusions 114

6 Summary and Outlook **116**

Chapter 1

Introduction

Heterogeneous catalysts are of outstanding relevance for a vast number of processes in chemical industry [1–3]. The term "heterogeneous" indicates that the catalyst and the reactants are present in different phases. Typically, the catalyst is a solid, while the reactants are liquids or gases. Heterogeneous catalysts often consist of a support material, on top of which the active species is located. Supporting the active phase was originally intended to increase the surface area of the active species and increase mechanical strength [4]. In this picture, the support was seen as an inert material that would merely enhance the degree of dispersion. However, it was found later that specific interactions between the active compound and the support can take place, which modifies the structure of the active compound, and its reactivity.

As industrial heterogeneous catalysts are quite complex and also ill-defined, their investigation at the atomic level is hampered. However, such detailed studies are needed in order to link structural properties of the catalyst to its reactivity pattern, as this provides the key to catalyst optimization. One way to overcome this issue relies on the introduction of well-defined models with significantly reduced complexity.

The fabrication of model catalysts in the context of this work requires the growth of flat, thin, crystalline, metal oxide films on a metal single crystal surface. Metallic or oxidic nanoparticles are deposited subsequently. A typical model is shown in Figure 1.1. Key aspects of surface science compatible models were reviewed, e.g., by Freund [6], Goodman and co-workers [7], Campbell [8] and Henry [9]. The advantage of such models is that they can be investigated by means of surface science methods. The book by Niemantsverdriet can be named as one example for a concise summary on the applications of these methods to model catalysis [10]. This surface science approach provides the access to the atomic level studies.

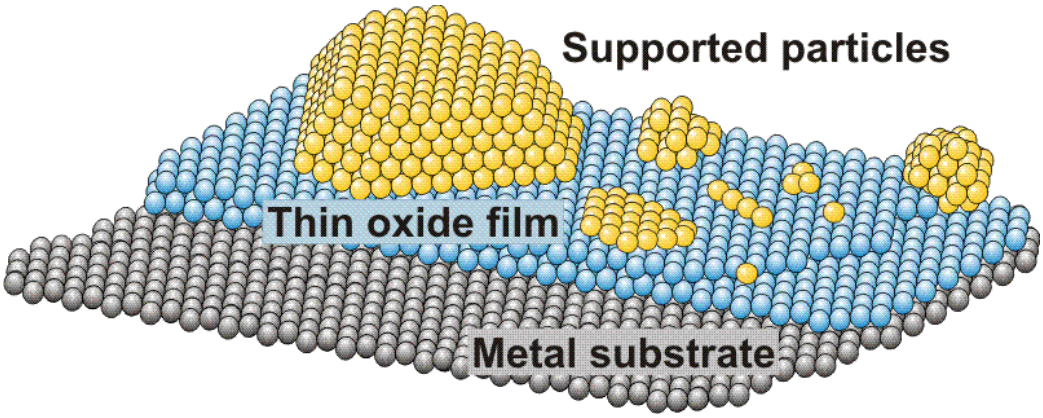

Figure 1.1: Schematic of a typical surface science compatible model catalyst (adapted from [5]). Within this work, the supported particles consist either of a metal or of another oxide.

Surface science compatible model catalysis suffers from two drawbacks: the pressure gap, and the materials gap. The term "pressure gap" refers to the fact that the pressure regime under which surface science experiments are carried out, differs from the industrial application by several orders of magnitude. The issue that the models consist of thin films, which are novel materials specifically created for these studies, and that their structural and electronic properties might not be comparable to the corresponding industrial catalyst, is summarized as the "materials gap".

This work is principally focussing on two compounds: the oxides of the transition metals niobium and vanadium, which are homologues in Group 5 of the Periodic Table of Elements (Figure 1.2). The role of these oxides for heterogeneous catalysis has been summarized by Wachs, yet with a focus on vanadium oxide and niobium oxide [11]. In order to give a motivation to the present work, the general relevance of niobia and the vanadia is summarized in the following text. A more detailed literature review on previous model studies is reviewed at the beginning of each Chapter or Section, respectively.

Ziolek [12], as well as Tanabe [13], reviewed the catalytic applications of niobium-containing compounds, such as multiple niobium oxide phases, carbides, sulfides, nitrides and oxynitrides, as well as phosphates. Another well-known example of niobia-based catalysis is the Fischer-Tropsch process, by which hydrocarbons are synthesized from CO and H_2. The active species typically contains cobalt or iron. It was shown that a niobia support enhances catalyst selectivity toward reaction products with higher molecular weight, as compared to silica or alumina [14–17]. The influence of niobia is rationalized

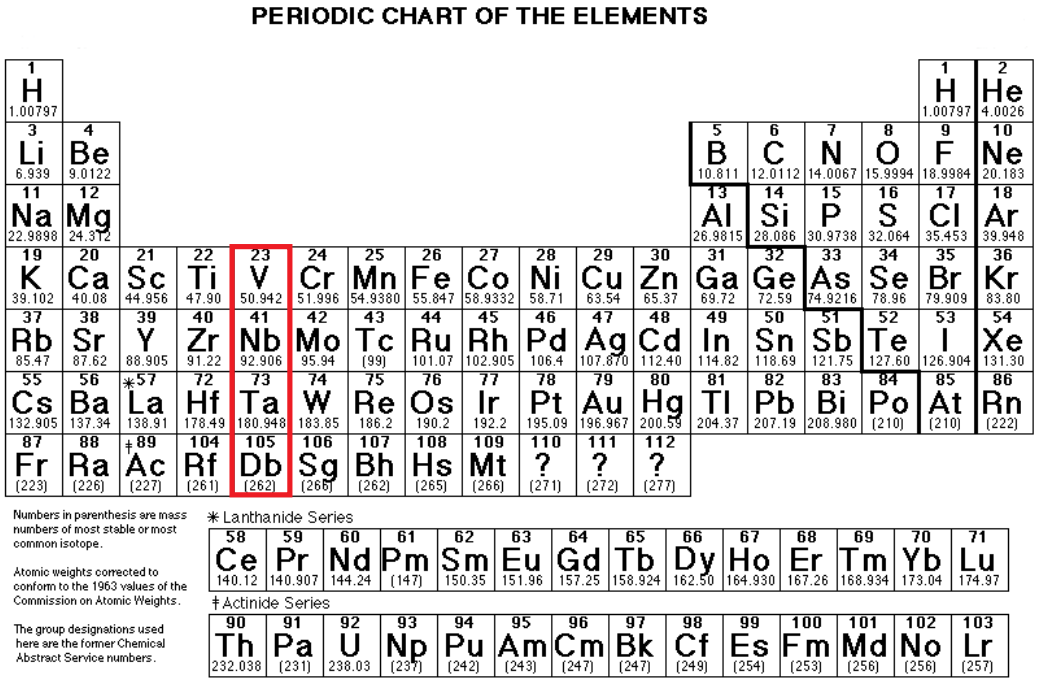

Figure 1.2: Periodic Table of Elements. Group 5 is highlighted.

in terms of the strong metal-support interaction, SMSI. Since niobia is a reducible oxide, and silica and alumina are not, some kind of redox interaction may take place at the interface between the active compound and the niobia substrate, modifying the reactivity of the active compound.

Niobia can also be the active species or a promoter for other catalysts, when it is in turn supported by another material. Supported niobia often shows better performance, as compared to the bulk system [12,18,19]. More than a decade ago Wachs and co-workers started the investigation of niobia supported on alumina and other oxides, including silica and zirconia [11, 19–27]. Reference [26] concisely reviews Group 5 metal oxides both in the bulk phase and as supported monolayer catalysts. The groups of Schmal [14,15,28–35] and Guczi [36–38] have investigated catalyst systems promoted by niobia.

Vanadium oxide, on the other hand, is the most important material in metal oxide catalysis [1, 3, 39–42]. The oxidation state of vanadium varies from (+2) to (+5), and hence, the stoichiometry of vanadium oxide is manifold: V_2O_5, V_6O_{12}, VO_2, V_2O_3, VO, $V_{2n}O_{5n-1}$ (Wadsley phases) and V_nO_{5n-1} (Magnéli phases). This stoichiometric wealth and, in particular, the ability to switch between two oxidation states with relative ease is believed to be an important factor for the catalytic activity of vanadium oxide [43].

Surnev *et al.* provide a review on vanadium oxide surfaces, in which vanadia single crystal, vanadia thin films supported on another oxide and vanadia thin films grown on a metal substrate are summarized [44]. Among the oxide supports presented, the most relevant substrate for the present work, are alumina, tin oxide, ceria and titania. A particularly interesting class of oxide-supported vanadia catalysts are the monolayer catalysts. Despite the name, the actual thickness of the vanadia overlayer can exceed one monolayer: a "monolayer catalyst" is defined as the amorphous interface region, as determined by x-ray diffraction [45, 46]. Hanke *et al.* describe the preparation and performance of SiO_2-supported vanadia, the coverage of which is equivalent to one monolayer [47]. This intends to involve all vanadium atoms into the reaction as active centers. Supported vanadia monolayer catalysts are applied in the oxidation of methanol and to reduce NO_x emissions [39,48–56].

Vanadia is used for various oxidation reactions, such as the oxidation of chlorophenol [57], soot oxidation [58], the oxidative dehydrogenation of ethane [59], ethanol oxidation [60], and many more. It is also the catalyst in the contact process, the technical production of H_2SO_4, one of the most important reactions in the chemical industry [61]. Within the present work, vanadium oxide is used for the catalysis of the oxidative dehydrogenation, ODH, of methanol to formaldehyde. As outlined above, supporting the active species enhances the surface area and leads to a gain of mechanical strength

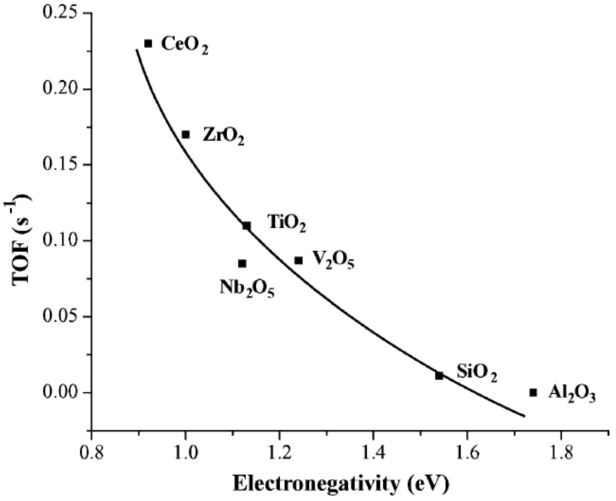

Figure 1.3: Activity of supported vanadium oxide in methanol oxidation to formaldehyde as a function of the support (taken from [63]). The turn-over frequency is most enhanced by cerium oxide.

[4]. Therefore, supported vanadia is most often used. As the catalyst for the ODH of methanol, it has received much attention in the recent past [39,46,62].

The influence of various supports on this reaction was reviewed by Wachs [63]. As shown in Figure 1.3, which is reproduced from reference [63], the turn-over frequency, of this reaction is most enhanced by cerium oxide. Accordingly, the present work is focussing on ceria-supported vanadia. Cerium dioxide, CeO_2 is known for its oxygen storage capacity. This effect is exploited in three-way catalysis, the catalytic cleaning process of automotive exhaust gas [64–67]. The advantage of CeO_2 is its ability of acting as an oxygen buffer, which is associated with a high mobility of O^{2-} anions in the CeO_2 lattice.

Industrial implementations of the ODH of methanol mainly rely on two types of catalysts. Ag-based catalysts have been used since the beginning of the 20^{th} century. Their disadvantage, oxidation temperatures as high as 1000 K [68], could be overcome by the introduction of the Formox process. The Formox process is based on mixed iron-molybdenum oxide and allows for lower operation temperatures ($\sim$ 600 K). Despite substantial efforts in catalytic research, eminent issues need still be overcome, namely the minimization of by-product formation. As mentioned above, vanadium oxide is a promising alternative catalyst for the ODH of methanol.

This reaction is greatly relevant for industrial chemistry, because its main

product, formaldehyde, is a very versatile chemical compound. It is used in the manufacture of many products of the daily life. The main part of industrial formaldehyde production is employed to give a wide range of condensates; i.e., urea-phenolic and melamine resins and, to a lesser extent, their derivates. It is further utilized in the production of papers, paints, adhesives, cosmetics, explosives, fertilizers and textiles [69, 70]. However, formaldehyde formation is not the only useful outcome of methanol oxidation. Direct methanol fuel cells, DMFCs, in which this process is exploited, represent one approach to overcome contemporary energy concerns. Wasmus and Küver have reviewed the development of DMFCs [71] (and references therein). Finally, a selective oxidation of an alcohol to the corresponding aldehyde is a challenge in fundamental chemical research. In the liquid phase, addition of a typical oxidant, such as $K_2Cr_2O_7$, to the alcohol is not selective for the formation of the aldehyde, as dichromate oxidizes often the aldehyde further to the corresponding carboxylic acid [72].

Due to its relevance, the ODH of methanol is studied as a test reaction for various vanadia-based and other model catalysts in the Department of Chemical Physics of the Fritz Haber Institute, Berlin [73–75], to which the present study intends to contribute.

This work is organized as follows: Chapter 2 provides an overview on the ultrahigh vacuum chamber and the surface science methods of relevance for this work. Chapters 3 and 4 present the results on the characterization of a series of different niobia-based systems. Chapter 3 deals with the monolayer and multilayer niobia films, as well as with niobia-supported cobalt. Niobia particles supported on alumina films are treated in Chapter 4, with respect to structure and thermal stability. Ceria-supported vanadia particles are presented in Chapter 5. After a characterization of the ceria support, structural aspects of the model system are discussed. Subsequently, its reactivity in the oxidation of methanol is outlined and linked to structural properties of the model catalyst. Chapter 6 gives a summary of the results and an outlook.

Chapter 2

Experimental

2.1 Apparatus

Ultrahigh vacuum, UHV (i.e., a pressure below 10^{-9} mbar), is required for many surface science experiments. As outlined in Chapter 1, the use of surface science in catalytic research aims at the preparation and investigation of well-defined model catalysts. However, the models can only be well-defined, if the experimentalist has control over their preparation conditions. In particular, the pressure of the gas phase surrounding the sample is an important issue, since adsorption from the background gas is inevitable, but mostly unwelcome. For this reason, UHV conditions are needed, because only then adsorption from the background is sufficiently slowed down, such that it becomes negligible on the time scale of the experiments.

The experiments presented in this work were carried out in three different UHV chambers. The chambers are denoted IRAS, STM and PES in the following, after the principal method implemented there (infrared reflection-absorption spectroscopy, scanning tunneling microscopy, x-ray photoelectron spectroscopy). All three chambers have a base pressure of $\leq 5\times10^{-10}$ mbar. The STM chamber (e.g., see [76]) and the PES chamber (e.g., see [77]) are described in the literature. The IRAS chamber consists of two parts, which are separated from each other by a gate valve. The bottom part houses the HREEL spectrometer (VSI Delta 0.5), with an ion getter pump and a Ti sublimation pump attached to it. The top part is equipped with devices for sample preparation (e.g., sputter gun, metal evaporators, gas handling), a quadrupole mass spectrometer (HIDEN HAL RC 201) and a Bruker IFS 66 v/S mid-infrared spectrometer, which is attached to the UHV chamber via two KBr windows. Figure 2.1 schematically depicts the spatial arrangement of the top chamber and the supplements mounted to it.

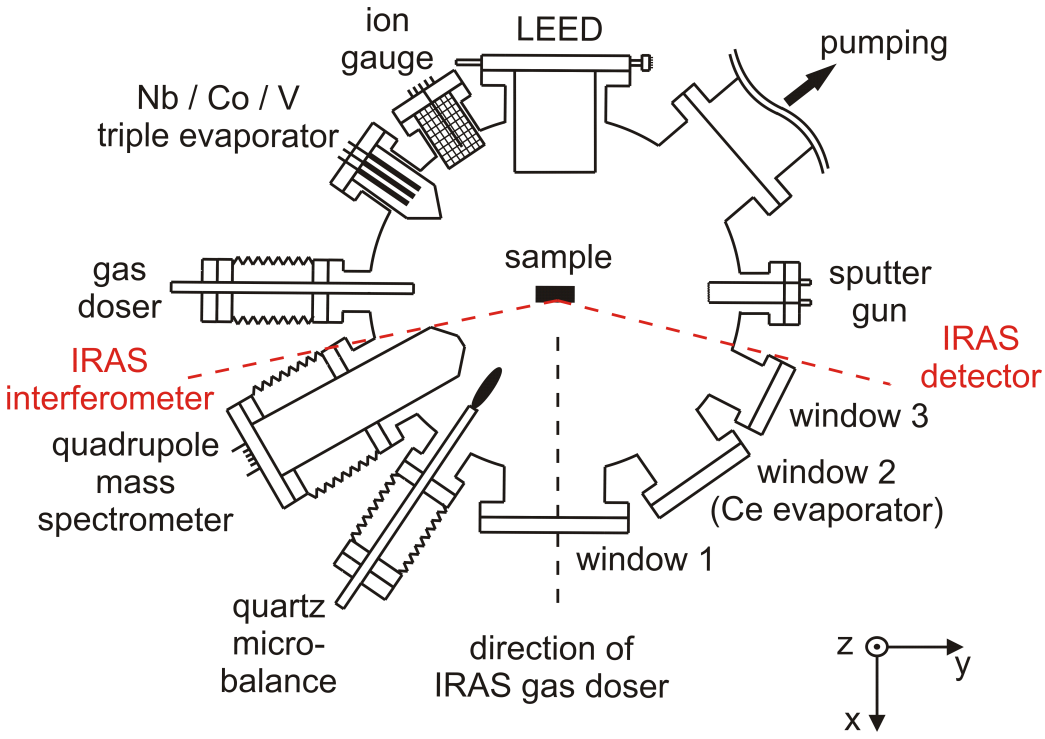

Figure 2.1: Schematic of the top chamber (top view). During experiments presented in Chapter 5, window 2 was replaced by the Ce source (single evaporator). The IRAS components are installed at a lower z level within the top chamber.

2.2 Sample Preparation

All samples used throughout this work are metal or metal alloy single crystals: $Cu_3Au(100)$ (Chapter 3), NiAl(110) (Chapter 4) and Ru(0001) (Chapter 5), where the numbers in parentheses denote the respective Miller indices. In the IRAS chamber, samples are heated resistively; i.e., by running a DC current through a pair of Ta wires (0.4 mm diameter) spot-welded horizontally to the sample. These wires are in turn spot-welded to vertical Ta rods (1 mm diameter). In order to monitor the temperature, the ends of thermocouple wires (chromel/alumel, 0.25 mm diameter) are jointly spot-welded to the unpolished side of the crystal. Figure 2.2 shows a schematic of the front view of this setup.

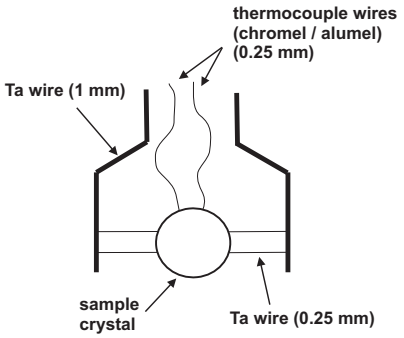

Figure 2.2: Sample mount (front view). The ends of the thermocouple wires are jointly spot-welded to the rear of the sample crystal.

The sample is suspended from the bottom of a manipulator, which allows to position the sample inside the chamber. The thermocouple wires are connected to a feedback controller (HS 130, Schlichting Physikalische Instrumente), which is capable of reading the thermocouple voltage directly as a temperature. A power supply (Delta Electronica SM 7020-D) provided the DC current (upper limits: 20 A, 70 W) for resistive sample heating. For the sake of reproducibility, the feedback controller is used to regulate the output of the power supply. This also allowed sufficiently stable heating rates to be achieved ($\pm$ 0.1 Ks^{-1}), which is of great relevance for temperature-programmed desorption experiments (see Section 2.8). The manipulator consists mainly of a "cold finger"; i.e., a reservoir for liquid N_2. The electrical connections for sample heating is guided through the cold finger. If the cold finger is filled with liquid N_2, heat will be drained from the sample via the metallic connections. Thereby, the sample can be cooled from room temperature to as low as 95 K within $\sim$ 15 min.

Preparation of well-ordered and (ideally) contaminant-free oxide films is possible only on clean substrates. Substrate cleaning is achieved by sputtering with Ar^+ ions, for which the top chamber was filled with argon to $\sim 10^{-5}$ mbar. The ions are accelerated toward the sample with a kinetic energy of $\sim$ 1 keV. Typical ion currents of $\sim 1\ \mu$ can be achieved. The typical duration of a single sputtering procedure is 45 min. Subsequently, the sample is annealed for 5 min to 800 K - 1300 K, depending on the sample material. The sputtering and annealing cycle is repeated several times. Crystallinity and absence of impurities are verified by Low Energy Electron Diffraction, LEED, and Auger Electron Spectroscopy, AES, which are presented in Sections 2.3 and 2.4, respectively.

The preparation of metal oxide films and particles can be done in several ways. In the following, the method of Physical Vapor Deposition, PVD, is explained. The UHV chambers used in this work are equipped with commercial metal evaporators (Focus EFM 3T in the case of Nb, Co, V; EFM 3 in the case of Ce; see also Figure 2.1). The metal in question is heated by high voltage(≤ 1 kV) assisted electron bombardment. In order to avoid unwanted sputtering effects from the evaporated metal atoms, the sample is biased to the high voltage. Thus, the flux of the evaporated metal is limited to thermal kinetic energy only, allowing for a soft landing on the sample. The evaporant can either be present as a rod with a diameter of 1-2 mm, or it is filled into an appropriate crucible (W or Mo). The use of a crucible is mandatory for metals that melt before yielding a substantial flux of evaporation, such as for cerium. Sufficiently small Ce pieces are placed in the crucible, where they are melted and re-solidified, in order to get a unified phase. Oxidation of the evaporated metals is done either by deposition in an oxygen ambient or by alternating deposition and oxidation steps. In certain cases, the oxidation of the metal substrate prior to the metal deposition is beneficial. For example, the growth of niobium oxide on $Cu_3Au(100)$ requires the implantation of oxygen into the substrate. The quality of the as-prepared oxide films is confirmed using LEED and AES. The preparation of particles supported on these films follows the same approach.

Details on the preparation of the individual systems relevant to this work, such as the deposited amount of the metal and the oxidation conditions, are given at the beginning of each respective Chapter or Section. The amounts of metal evaporated are given there in terms of nominal thickness; i.e., as the average height all across the surface. The nominal thickness can be well below atomic diameters.

2.3 Low Energy Electron Diffraction

By Low Energy Electron Diffraction, LEED, both the surface structure and symmetry of a given crystal and of adsorbate super-structures can be determined. It is based on the diffraction of electrons. A (relatively low) voltage, V, accelerates the electrons to a constant velocity, after which they are scattered on a sample surface. Combining the definition equations of the kinetic energy, E_{kin}, the momentum, p, and the de Broglie wavelength, λ, of an electron, the following relation between the beam voltage and λ is established:

$$\lambda = \frac{h}{\sqrt{2meV}} \tag{2.1}$$

where $h = 6.626\times10^{-34}$ Js is the Planck constant, $m = 9.11\times10^{-31}$ kg is the electron mass and $e = 1.6022\times10^{-19}$ C is the elementary charge. Hence, typical LEED voltages, which range between 20 V and 200 V, correspond to wave lengths below 0.3 nm, according to equation 2.1. This is in the order of interatomic distances in a crystal lattice, which leads to the observation of interference patterns on a luminescent screen opposite to the sample, as shown in Figure 2.3.

The same Figure also shows, how LEED patterns can be constructed using the Ewald sphere [78]. The real space atomic positions in a crystal lattice are given by a vector $\vec{F}$. Another vector, $\vec{G}$, is defined as the reciprocal lattice. $\vec{F}$ and $\vec{G}$ are related to each other as follows:

$$e^{i\vec{F}\vec{G}} = 1 \tag{2.2}$$

Note that the component of $\vec{F}$ perpendicular to the surface is inherently zero. Hence, the corresponding component of $\vec{G}$ has an infinite length, as indicated by the dashed parallel lines in Figure 2.3. Diffraction spots are observed, where this vector intersects with the Ewald sphere, which is explained in the following.

The incident electron beam has a wavevector, $\vec{k_0}$,

$$|\vec{k_0}| = \frac{2\pi}{\lambda} \tag{2.3}$$

which is scattered from the sample. The scattered wavevectors, $\vec{k_{ij}}$ (i,j $\in \mathbb{Z}$), have the same length as $\vec{k_0}$. Both $\vec{k_0}$ and $\vec{k_{ij}}$ are radii of the Ewald sphere. The difference vector between $\vec{k_0}$ and $\vec{k_{ij}}$, $\Delta\vec{k}$, is called the scattering vector.

The Bragg diffraction condition for constructive interference is as follows:

$$2d\ sin(\theta) = n\lambda \tag{2.4}$$

where d is the distance between two adjacent lattice layers, θ is the angle between the incident beam and the surface, and n is an integer number. It is satisfied, where the Ewald sphere intersects with the reciprocal lattice:

$$\Delta\vec{k} = \vec{G} \tag{2.5}$$

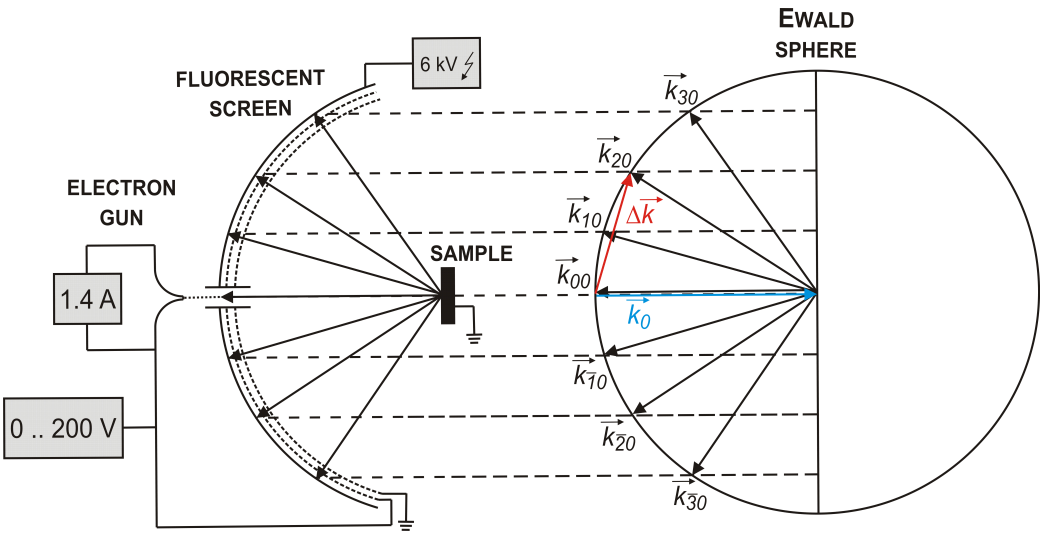

Figure 2.3: Basic principles of LEED. Incident electrons with a wavevector $\vec{k_0}$ are scattered from the surface with a wavevector $\vec{k_{ij}}$ of the same absolute value. Both are radii of the Ewald sphere. Diffraction spots are observed, where the component of the reciprocal space lattice perpendicular to the surface (dashed lines) intersects with the Ewald sphere.

The experimental setup of LEED is depicted in the left part of Figure 2.3. The filament is operated with a current of 1.4 A, which produces an emission current of $I_{em} \approx 20$ μA. In order to avoid deflection of the electron beam by the terrestrial magnetic field, the optics are covered in an anti-magnetic shield, which is made from μ-metal.

The typical value for the beam voltage is 70 V throughout this work, because then the screen shows the equivalent of the first Brillouin zone, which is the reciprocal of the real space lattice unit cell. The beam is focused by electrostatic lenses and reflected from the sample toward a luminescent screen. Before they are registered at the screen, they pass a repelling electrode, which is set to the beam acceleration potential (V in equation 2.1), in order to deflect background electrons. Beyond this stage, the electrons are accelerated by a potential of typically 6 kV to produce a pattern of sufficient brightness.

The pattern can be viewed either from the back or from the front through window 1, as depicted in Figure 2.1. The patterns can be recorded using a camera mounted to the back of the screen.

2.4 Photo- and Auger Electron Spectroscopy

Photoelectron Spectroscopy, PES, is a technique that is used to probe the chemical composition of a given sample and the oxidation state(s) of the chemical elements present. It is based on the photoelectric effect (photoeffect, Hertz effect); i.e., the capability of photons to extract electrons from a bonded state, which results in a measurable electrical current. According to Einstein [79], only photons with an energy E_γ above a certain threshold are absorbed. This threshold consists of two parts: the binding energy, BE, and the work function, ϕ. While ϕ is a material constant representing a barrier for electrons leaving the surface, BE is the energy of the orbital, in which the electron is bonded initially. Given E_γ is greater than $BE+\phi$, the electron is ejected. The excess amount of energy is transferred to the ejected electrons (i.e., photoelectrons) as kinetic energy, E_{kin}:

$$E_{kin} = E_\gamma - \phi - BE \tag{2.6}$$

The desired information is contained in BE. It becomes measurable indirectly through the measurement of E_{kin}, which is performed as follows: the photoelectrons are energy-selected by a hemispherical filter, which can only be passed by electrons with one specific E_{kin}. Variation of this pass energy establishes the photoelectron intensity as a function of E_{kin} and eventually of BE. Detection of the energy-selected electrons is done by a secondary electron multiplier. The basic aspects of PES (including the Auger decay discussed below) are summarized in Figure 2.4.

Depending on E_γ, two variants of PES are distinguished. Ultraviolet Photoelectron Spectroscopy, UPS, is based on photon energies of ~ 50 eV, by which valence electrons are ejected. For X-Ray Photoelectron Spectroscopy, XPS, the photon energy can be even greater than 1 keV, by which core electrons are probed. While the BE of valence electrons provides information on chemical bonds, the BE of core electrons is indicative of oxidation states, as outlined in the following.

The value of PES measurements stems from the fact that BE depends on the electronic configuration of the atom that ejects the photoelectron. In particular, a change in the oxidation state (i.e., a modification of the valence shell) notably affects the BE of core levels. Besides initial state effects, the final state must also be considered. For example, in the case of

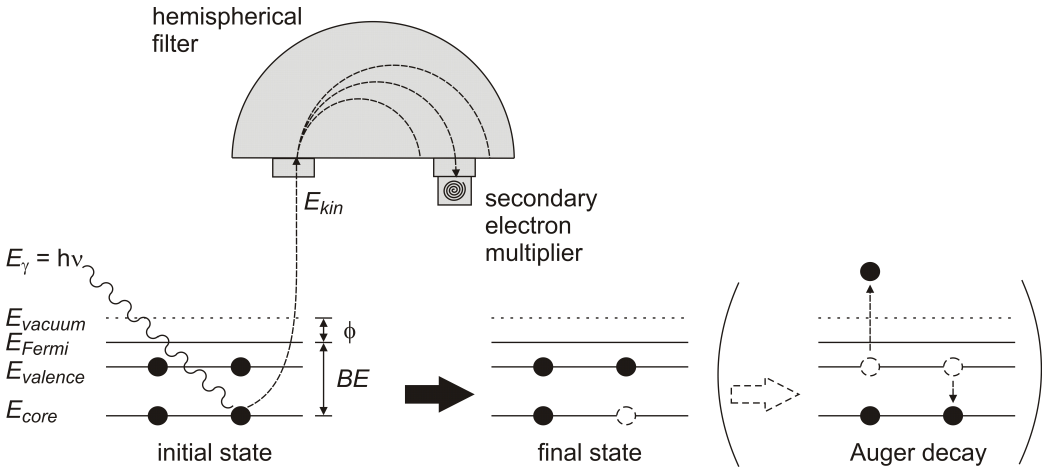

Figure 2.4: Basic principles of PES. The Auger process as one possible decay is included.

thin oxide films, the hole created by photoexcitation can be shielded and thus energetically stabilized by electrons from the nearby metallic substrate. Moreover, some photoelectrons can transfer a part of their kinetic energy to another electron of the photo-ionized atom. This reduces the measured value of E_{kin} and gives rise to satellite peaks in the spectrum, which differ from the main feature by the amount of energy transferred into the secondary excitation. The final state of the latter can be bound or unbound, and the process is then called "shake-up" or "shake-off", respectively.

PES experiments presented in this work were carried out at the BESSY II facility (beamline UE52-PGM). The use of synchrotron radiation has the advantages of (i) E_γ being adjustable over a wide range and (ii) a superior brilliance (photon flux per energy interval) by comparison to conventional x-ray sources.

The above-mentioned Auger process (see Figure 2.4) is one possible way for the final state to decay. In this process the hole is filled by an electron that originates from a higher shell of the same atom, and the energy concomitantly released is used to eject another electron, the Auger electron. As Auger electrons are detected along with photoelectrons in PES measurements, they must be distinguished from each other, which can be done by recording the same PE spectrum at different E_γ. The kinetic energy of the Auger electron only depends on the electronic configuration of the excited atom, and, in particular, it is independent of the energy of the incident beam that created the hole. Hence, application of equation 2.6 to the raw data will cause Auger peaks to shift by exactly the amount by which E_γ has been modified, while

PES peaks maintain their position.

The Auger process has been exploited for the implementation of Auger Electron Spectroscopy, AES, in which the core hole is created by irradiation with electrons. The practical advantage is that it is possible to use LEED optics for AES. Thus, a device with an as wide-spread application in surface science as LEED can be used for element-sensitive measurements as well. The electron beam from the LEED filament is accelerated by a potential of 2 keV - 5 keV (2.5 keV were used throughout this work). The LEED screen is used to collect the electrons, with a variable pass energy. Since AES peaks are rather low in intensity, the spectra are often given as their first derivative. Additionally, the quality of synchrotron PES measurements is far superior to AES measurements with optics primarily designed for LEED, which is why throughout this work AES was used only to check the cleanliness of the sample.

2.5 Scanning Tunneling Microscopy

Scanning Tunneling Microscopy, STM, is a surface science method that allows imaging of flat and conducting sample surfaces [80–82]. It was introduced in the early 1980s by Binnig and Rohrer [83]. As it offers real space surface imaging on the nanoscale, it was quickly established as a highly relevant surface science technique. Even atomic resolution can be achieved; i.e., adjacent atoms can be distinguished from each other. Hence, surface structure and periodicity are discernible in real space.

STM measurements rely on the tunneling effect, requiring a quantum mechanical description. An extensive presentation can be found, e.g., in [84], where general aspects are presented, and in [81,82], where it is related to the application in STM. It is also very briefly summarized in the following text. The tunneling effect is based on the overlap of wave functions separated by an energy barrier of finite height. If the barrier is higher than the energy of an electron on one side of the barrier, it would keep the electron strictly on this side in the classical picture. The quantum mechanical treatment, however, predicts a non-zero probability for the electron to reside within the classically forbidden regime of the barrier. Hence, the wave functions of the filled state on one side and the empty state on the other side overlap with each other, which is why the electron can “tunnel through the barrier”.

In STM, the tunneling effect occurs between the sample and a very sharp tip, which both have to be made from electrically conducting materials. The tip and the sample are not in touch with each other, which imposes the tunneling barrier between the two. If the tip has approached the sample

sufficiently while a voltage is applied between them, a tunneling current, I, can be measured. In a first approximation [81], the current is given as:

$$I \propto f(V)e^{-\alpha\sqrt{\langle\phi\rangle s}} \tag{2.7}$$

where $\langle\phi\rangle$ denotes the height of the penetrated barrier, $f(V)$ is a function of the voltage V between tip and sample, s is the tip-sample distance, and α is a constant. For a small bias V, $\langle\phi\rangle$ is related to the work functions of tip and sample. In the simple case of a homogeneous metal surface at low temperature, $f(V)$ is proportional to V; i.e., Ohm's law is applicable. In general, however, it depends on the electronic structure of both the sample and the tip. A theoretical treatment of the tunneling current is provided by Tersoff and Hamann [85, 86].

The model catalysts presented in this work are based on oxide films, which are typically electrically insulating. Therefore, for STM measurements, these films must be (i) grown on a metallic substrate, and (ii) sufficiently thin, such that tunneling is still possible.

Typical tip-sample distances are in the order of a few Å (Ångstrom; 1 Å = 10^{-10} m) [10]. Typical tunneling parameters throughout this work were currents in the nA range and voltages of 2-4 V. The voltage can be applied in either polarity; i.e., electrons can be directed from the tip to the sample and also in the opposite direction. Electrons going from the tip to the sample will interact specifically with empty electronic states on the sample, while electrons going in the opposite direction must originate from occupied sample states.

There are two principal modes of operation for STM: constant height or constant current. However, for the vast majority of STM applications and, in particular, for all experiments presented in this work, only the latter is important. In the constant current mode, a feedback controller regulates the tip-sample distance in order to keep the current at the preset value, while the tip scans across sample areas with different heights or different electrical conductivities. The variation of the feedback signal in two lateral coordinates is used for mapping the sample. Such images contain convoluted information about both the morphology and conductivity of the sample surface, as well as the electronic structure of the tip and the height of the tunneling barrier, which depends on the work function of the surface. Hence, STM images can be interpreted as topographical maps, only if all other contributions are constant.

As stated above, the tip must be very sharp; ideally with only a single atom at its apex. A blunt tip will make surface features such as particles appear larger than their actual dimensions. This tip deconvolution effect

applies also to particles that are very close together. Moreover, a tip with a double apex can show artificial "shadows" of protruding surface features. Sharp tips can be achieved by chemical etching under ambient conditions, followed by sputtering inside the UHV chamber. On the other hand, ready-made tips are commercially available, which were used in this work.

2.6 Infrared Spectroscopy

2.6.1 Physical Principles of Infrared Spectroscopy

Infrared (IR) Spectroscopy relies on vibrational transitions induced by photon absorption. Since the wavenumber of the absorbed photon is specific for the excited transition, IR spectroscopy allows for the investigation of the presence or absence of certain vibrational modes, which renders it a powerful tool for chemical analysis. Inherently, absorption-induced transitions proceed from lower to upper energy eigenstates. For energetic reasons, only photons that fall into the IR region of the electromagnetic spectrum are suitable for vibrational transitions.

In the following, the basic principles of vibrational transitions are summarized along the lines of a simple model, the harmonic oscillation of a diatomic molecule in the gas phase. This model considers the kinetic and the potential energy of the oscillator, the sum of which is conserved. In the classical picture, the system is oscillating at an eigenfrequency, ν_0:

$$\nu_0 = 2\pi\sqrt{\frac{k}{\mu}} \tag{2.8}$$

where k is the spring constant, and μ is the reduced mass. The reciprocal reduced mass, $\frac{1}{\mu}$, is defined as the sum over all reciprocal atomic masses:

$$\frac{1}{\mu} = \sum_i \frac{1}{m_i} \tag{2.9}$$

For a quantum mechanical treatment, however, the molecule must be described by a wave function, Ψ. The stationary Schrödinger equation serves as an ansatz:

$$\frac{d^2\Psi}{dx^2} + \frac{2\mu}{\hbar}(E_{vib} - \frac{kx^2}{2})\Psi = 0 \tag{2.10}$$

where $h = 6.626\times10^{-34}$ Js is the Planck constant, and $\hbar = \frac{h}{2\pi} = 1.055\times10^{-34}$ Js is the reduced Planck constant or Dirac constant. The solution of equation

2.10 for the energy eigenvalues, E_{vib}, are given as a function of the vibrational quantum number, v.

$$E_{vib}(v) = (v + \frac{1}{2})hc\tilde{\nu}_0 \tag{2.11}$$

where $\tilde{\nu}_0$ is the eigenwavenumber of the oscillator. It is concluded from equation 2.11 that the vibrational eigenstate spectrum is discrete. A transition to a higher-lying state can be made only, if external energy is supplied, which matches exactly the energy difference between the initial and the final state. This is the resonance condition. (Moreover, the initial state must of course be sufficiently populated.) The photon energy, E_γ, is proportional to the wavenumber, $\tilde{\nu}$,

$$E_\gamma = hc\tilde{\nu} \tag{2.12}$$

where c is the speed of light. Following the resonance condition for a transition $|v'\rangle \leftarrow |v''\rangle$, with the abbreviation $\Delta v := v'$ - v'', the excitation energy can be expressed by the quantum number, v:

$$\begin{aligned} E_\gamma = hc\tilde{\nu} = E_{vib}(v') - E_{vib}(v'') &= (v' + \frac{1}{2})hc\tilde{\nu}_0 - (v'' + \frac{1}{2})hc\tilde{\nu}_0 \\ &= (v' + \frac{1}{2} - v'' - \frac{1}{2})hc\tilde{\nu}_0 = (\Delta v)hc\tilde{\nu}_0 \end{aligned} \tag{2.13}$$

Note that the excitation energy does not depend on the explicit values of v'' and v', but only on their difference, Δv.

The absorption of light can be described by means of the perturbation theory. The first order perturbation operator, $\hat{H}^{(1)}$, is given as the scalar product of the molecular dipole moment $\vec{\mu}$ and the electric field component $\vec{E}$ of the irradiated light:

$$\hat{H}^{(1)} = -\vec{\mu}\vec{E} \tag{2.14}$$

According to Fermi's Golden Rule, the absorption probability, W, can be expressed as follows:

$$W \propto |\, \langle \Psi(v')|\vec{\mu}|\Psi(v'')\rangle \,|^2 \tag{2.15}$$

where $\Psi(v'')$ and $\Psi(v')$ are the wave functions of the initial and final state, respectively, and $\vec{\mu}$ is the dipole operator. The expression

$$\vec{\mu}_{v''v'} := \langle \Psi(v')|\vec{\mu}|\Psi(v'')\rangle \tag{2.16}$$

is called the transition dipole moment, which yields:

$$\vec{\mu}_{v''v'} = \langle \Psi(v')|\vec{\mu}|\Psi(v'')\rangle = \langle \Psi(v')|\vec{\mu}_0 + \sum_Q \left(\frac{\partial \vec{\mu}}{\partial Q}\right)_0 Q + \ldots |\Psi(v'')\rangle \quad (2.17)$$

where Q is a normal coordinate (i.e., a bond length or an angle between two bonds) in the molecule or crystal lattice under investigation. Accordingly, $\vec{\mu}_Q := \left(\frac{\partial \vec{\mu}}{\partial Q}\right)_0$ is the dynamic dipole moment of the vibration along the direction of Q. The fact that all Q are pairwise linearly independent allows to break equation 2.17 down into a set of equations for each individual coordinate Q, of which there are 3N-6 in a molecule with N atoms (3N-5, if the molecule is linear):

$$\vec{\mu}_{v''v'Q} = \vec{\mu}_Q \langle \Psi(v')|Q|\Psi(v'')\rangle \quad (2.18)$$

Equation 2.19 implies that for an excitation to occur along a given coordinate Q, the related dynamic dipole moment must not vanish:

$$\vec{\mu}_Q \neq 0 \quad (2.19)$$

However, a set of selection rules applies further limitations, as outlined in the following. It can be shown that a transition $|v'\rangle \leftarrow |v''\rangle$ must obey the following selection rule, because W is zero otherwise:

$$\Delta v = v' - v'' = \pm 1 \quad (2.20)$$

($\Delta v = -1$ corresponds to photon emission, along with de-excitation.) Combining this with equation 2.13, it is $\tilde{\nu} = \tilde{\nu}_0$; hence, the eigenwavenumber of the oscillator is equal to the wavenumber of the absorbed photon. Moreover, due to equation 2.20, only one absorption band is expected for each transition. In this respect, vibrational spectroscopy is different from rotational spectroscopy, because the energetic spacing of rotational states is not equidistant (in the case of the rigid rotator). However, selection rule 2.20 can be violated, if, e.g., the oscillator is not perfectly harmonic, which might then lead to the observation of overtone bands in addition to the fundamental transitions that correspond to equation 2.20.

Another relevant issue is the symmetry of the initial state, $|v''\rangle$, and the final state, $|v'\rangle$, as well as of the dipole operator, $\vec{\mu}$. The integral $\langle \Psi(v')|\vec{\mu}|\Psi(v'')\rangle$ must be totally symmetric (i.e., the integrand must be an overall even function), because again W is zero otherwise. It is possible to derive the symmetry properties of the wavefunctions and the dipole operator by means of group theory. A comprehensive summary on the chemical applications of group theory is given by Cotton [87].

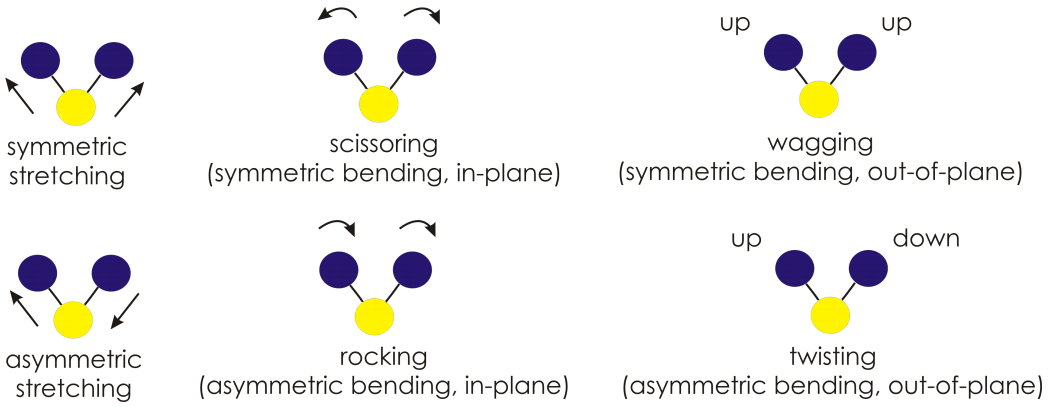

Figure 2.5: Schematic of the six simple vibrational modes of a methylene group: symmetric and asymmetric stretch, scissoring and rocking, wagging and twisting.

For completeness, the six simple vibrations of a methylene group, -CH_2-, are listed below and depicted in Figure 2.5. These modes are sufficient for the discussion of the adsorbates relevant to this work; however, it should be mentioned that more complex molecules may also perform more complex vibrations.

symmetric stretch, ν_s: the C/H bonds are stretched in phase;

asymmetric stretch, ν_a: the C/H bonds are stretched with a phase difference of π; i.e., while one band is fully elongated, the other one is fully contracted ("anti-phase");

scissoring or symmetric in-plane deformation, δ: the angle between the two C/H bonds is spreading and closing;

rocking or asymmetric in-plane deformation, ρ: the two C/H bonds are simultaneously bent to the same side, while the H/C/H plane is maintained;

wagging or symmetric out-of-plane deformation, ω: the two C/H bonds are bent in phase out of the H/C/H plane;

twisting or asymmetric out-of-plane deformation, τ: the bending of the two C/H bonds out of the H/C/H plane occurs in anti-phase.

2.6.2 The Fourier-Transform Spectrometer

Early IR spectrometers were dispersive spectrometers. The light from the IR source had to be monochromatized; i.e., a filter would allow only one wavenumber at once to pass and repell all others. Modern devices, however, function very differently, as they benefit from the implementation of Fourier transform (FT) technology. The light source is an SiC rod heated to above 1000 °C. Such a "globar" is a broad-band emitter in the range from 560 to 8000 cm^{-1}. The light is guided through a Michelson interferometer, before it reaches the sample and finally the detector. This is shown in Figure 2.6.

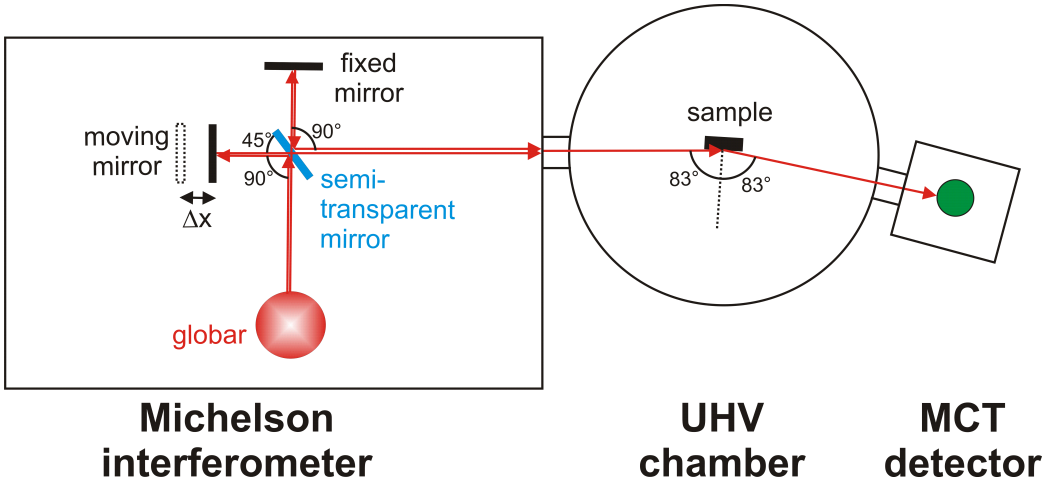

Figure 2.6: Schematic of the Infrared Reflection-Absorption Spectroscopy setup: Michelson interferometer, ultrahigh vacuum chamber with sample, mercury cadmium telluride detector.

The primary beam is split by the semi-transparent mirror. One half of the intensity crosses this mirror, while the other half is reflected perpendicular to the original beam. Subsequently, both fractions are reflected back to the center, where the semi-transparent mirror splits them again, into a total of four beams. Two new beams are formed by superposition of these four: one half of the intensity is reflected back to the light source and therefore lost. The other half leaves the Michelson interferometer and continues to the sample, from which it is reflected toward the detector under a grazing angle (83°) with respect to the normal of the sample surface. The Bruker IFS 66 v/S spectrometer, which was used here, is equipped with a mercury cadmium telluride, MCT, detector. The MCT alloy acts as a photodiode, which requires cooling by liquid N_2.

The purpose of the Michelson interferometer is to produce a beam with a

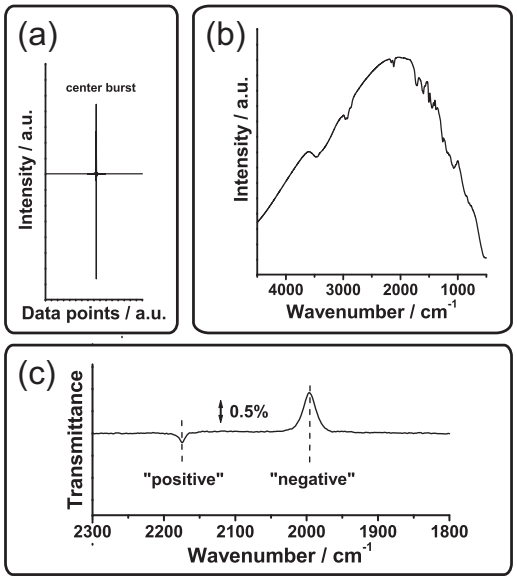

Figure 2.7: IRAS data. (a) interferogram (with center burst); (b) single channel spectrum (Fourier-transformed interferogram); (c) typical ratio of two single channel spectra. These data belong to Figure 5.11 in Section 5.4.1, where the origins of the observed "positive" and "negative" band are discussed. The base line in (c) represents 100% transmittance.

variable phase information, which is done by the superposition of two beams. The distance travelled by the beam that was reflected by the moving mirror, varies with time, while distance travelled by the other one is constant. Maximum constructive interference takes place, when the moving mirror and the fixed mirror have exactly the same distance from the semi-transparent mirror, leading to the center burst in the interferogram, as shown in Figure 2.7 (a).

Hence, the detected signal is an interferogram, as depicted in Figure 2.7 (a), from which a single channel spectrum (Figure 2.7 (b)) is obtained by application of the Fourier transform, FT, a mathematical operation. The single channel spectrum is the detected intensity as a function of the wavenumber. Therefore, it reflects the emission properties of the globar. However, absorption bands are minute by comparison to the intensity of the single channel spectrum. In order to eliminate the influence of the globar and to reveal the actual absorption band, each single channel spectrum must be divided by a reference spectrum. In practice, this means that one single channel spectrum has to be acquired before the sample is modified, and a second one afterward. Their ratio is the actual IR spectrum (such as, e.g., Figure 2.7 (c)). Note

that a species that appeared between the recording of the two spectra is represented by a "positve" band; i.e., a transmittance below 100%. Similarly, a vanishing species produces a "negative" band.

FTIR spectrometers have several advantages over dispersive spectrometers:

1. *Multiplex Advantage (Fellgett's Advantage).* In FTIR the light is not split into individual wavenumbers, before it is measured by the detector. As a consequence of the Fourier transform, each data point of the interferogram contains information on all detected wavenumbers. Moreover, the great number of data points leads to an improved signal-to-noise ratio.

2. *Throughput Advantage (Jacquinot's Advantage).* FTIR spectrometers have a simpler optical path, and, in particular, they lack the monochromator of dispersive spectrometers, which partially absorbed intensity. In FTIR, the intensity available is therefore higher.

3. *Frequency Precision (Conne's Advantage).* The frequency precison and accuracy of dispersive spectrometers depends on the calibration with external standards and on the ability of the electro-mechanics in the monochomator to move slits and gratings uniformly. FTIR spectrometers have an internal standard, typically a HeNe laser, which also clocks the moving mirror and the detector.

4. *Constant Spectral Resolution.* Different spectral resolutions for different wavenumbers may arise for dispersive spectrometers, as covering the entire spectral range often requires changing a grating in the course of the measurement. Apart from the interruption of the measurement, each grating may contribute differently to the overall resolution.

The Bruker IFS 66 v/S spectrometer offers the selection of the resolution in the software. 2 cm^{-1} are chosen, which represent a good compromise between quality and acquisition time.

2.6.3 Infrared Spectroscopy on Surfaces

For the investigation of surfaces, IR spectroscopy is implemented as Infrared Reflection-Absorption Spectroscopy, IRAS (less frequently IRRAS), or Reflection-Absorption Infrared Spectroscopy, RAIRS. It can be used to investigate the vibrations of both molecules and crystals. The lattice vibrations of crystals are called phonons. As a rule of thumb, the phonon range is

located below 1100 cm^{-1}, which is not fully accessible by mid-IR spectrometers. Those cover the full range of vibrations of adsorbed molecules; i.e., 4000 cm^{-1} to 1000 cm^{-1}. The lower spectral limit of the Bruker IFS 66v/S spectrometer used in this work is 560 cm^{-1}, but a large number of phonons (in the bulk) fall well below this number. As a consequence, the applicability of IRAS to the investigation of phonons is limited. Another method, High Resolution Electron Energy Loss Spectroscopy, which is better suited for phonon studies, is described in Section 2.7.

However, the general aim of this work is to correlate the reactivity of a given surface with its structural properties, and hence, surface phonons are most important. One prominent example for surface phonons is the stretching mode of a surface oxygen atom sitting atop a metal atom (called vanadyl group, V=O, in the case of vanadium), which is typically observed at $\sim$ 1040 cm^{-1} [88–90]. On the other hand, surface oxygen in a bridging position was found at 630 cm^{-1} to 740 cm^{-1} by Sock *et al.* [91], which is still within the above-mentioned detection limits.

The acronym IRAS actually refers to a particularly surface-sensitive way of acquiring IR spectra; i.e., its capability of detecting surface-located species (both adsorbates and surface phonons) is enhanced. This is achieved by grazing incidence (83°) with respect to the surface normal; i.e, nearly parallel to the sample surface. This geometry is depicted in Figure 2.6. As outlined by Hoffmann [92], the *s*-component of the electric field of the incident IR light suffers a phase shift of 180° , which is nearly independent of the angle of incidence. Hence, the *s*-component (which is oriented parallel to the surface normal) vanishes at the surface, due to destructive interference with the evanescent light. The phase shift of the *p*-component (which is oriented perpendicular to the surface normal), on the other hand, has a strong angular dependence, and particularly for grazing incidence, a large resultant *p*-component of the electric field is established. As a consequence, the surface intensity peaks sharply in this case.

Moreover, dipole vibrations (i.e., dynamic dipole moments, $\vec{\mu}_Q$; see equation 2.19) perpendicular to the surface are excited, and on metal surfaces (as well as on ultrathin oxide films grown on a metal substrate) these dipoles are amplified by the image dipoles created from free charge carriers in the metal. Dynamic dipoles parallel to the surface, on the other hand, are cancelled out by their image, which renders their detection impossible by means of IR spectroscopy. This effect, known as the metal surface selection rule, MSSR, is schematically depicted in Figure 2.8.

When IRAS is used to study vibrations of adsorbed molecules, the spectra contain intrinsic information on the surface. Adsorbates bind to the surface, and changes in their IR spectra with respect to the corresponding

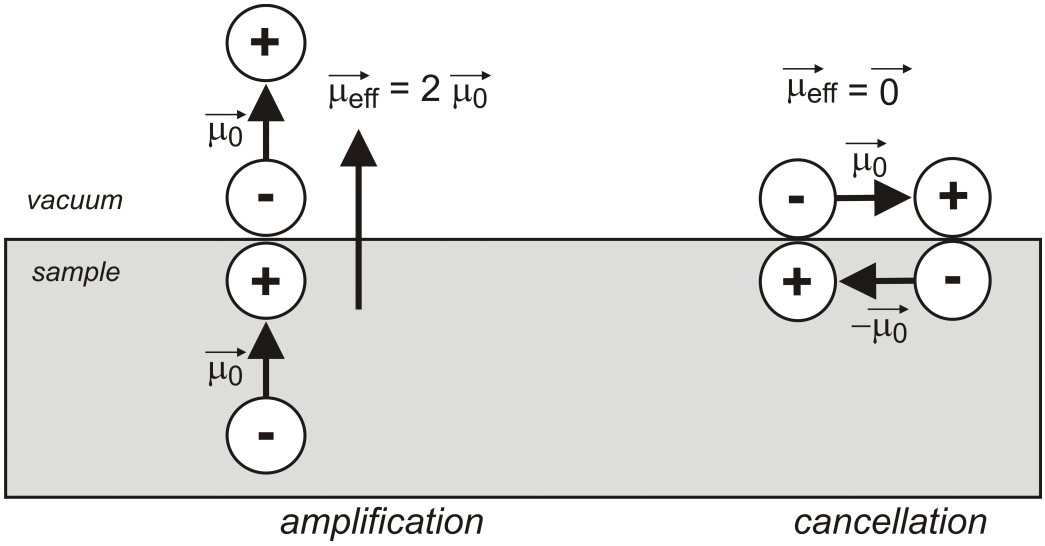

Figure 2.8: Illustration of the Metal Surface Selection Rule. The component of the dipole moment perpendicular to the surface, $\vec{\mu_\perp}$ can be detected by IRAS, because it is amplified by the image charge. However, the parallel component, $\vec{\mu_\parallel}$, and its image cancel each other out.

gas phase species may reveal details on the adsorption geometry and the electronic properties of the adsorbing surface atoms. As a consequence, certain adsorbates may serve to probe the surface.

The most commonly used probe molecule is carbon monoxide, for a number of reasons. First, it has a very simple vibrational spectrum, as only the carbonyl stretch is observed. Second, the related dynamic dipole moment is strong, which leads to intense absorption bands. Third, its adsorption and desorption is mostly reversible. Fourth, the adsorption of CO on (metal-containing) surfaces and its relationship to IR spectroscopy is understood well and was summarized by Blyholder [93].

The Blyholder model relates the strength of adsorption to the wavenumber of the carbonyl stretch, which is 2143 cm^{-1} for CO in the gas phase. The adsorption of CO onto a surface occurs via the non-binding electron pair located at the carbon atom, due to the electronic configuration of CO. As seen in Figure 2.9, the highest occupied molecular orbital, HOMO, of CO is identified as the 5σ molecular orbital, which is, within a very good approximation, equivalent to the non-binding electron pair located on the C atom. Hence, adsorption of CO occurs as "carbon-down", which results in a C/surface bond. This bond competes for available electrons with the C/O bond. A stronger C/surface bond is related to a weaker C/O bond, and

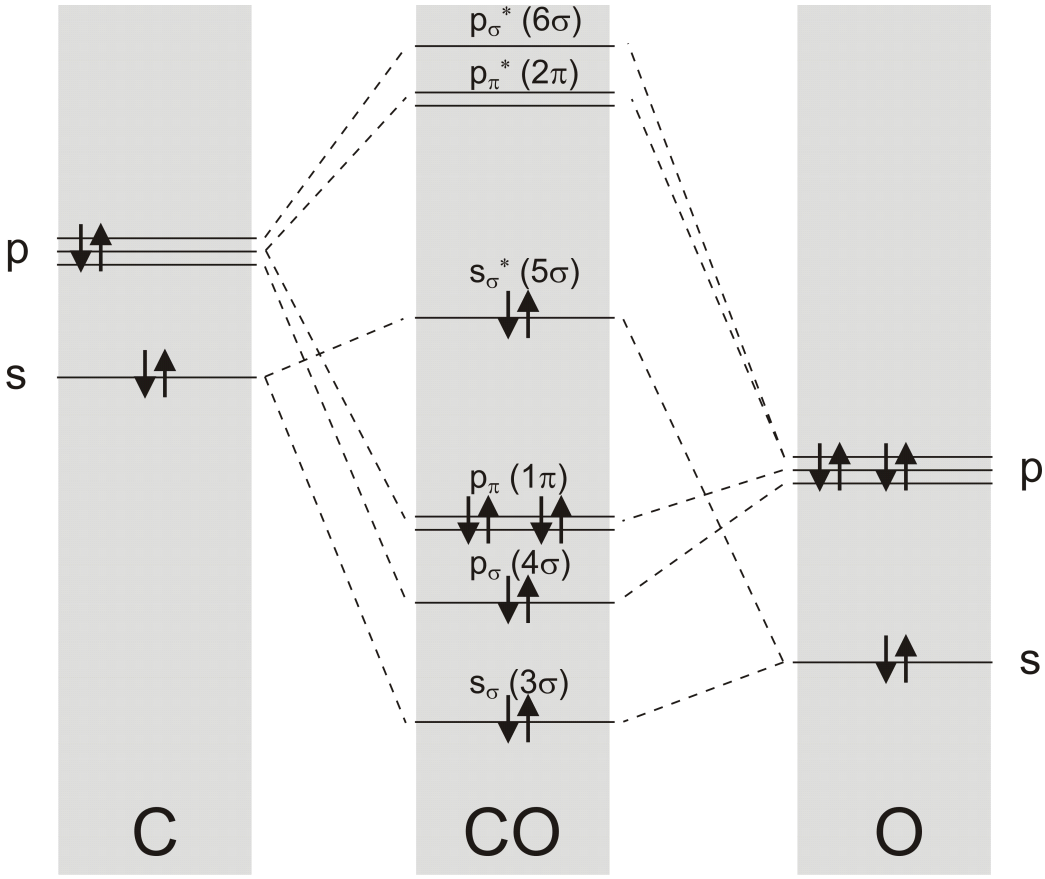

Figure 2.9: Molecular orbitals of carbon monoxide (after [94]). The 5σ orbital of CO is the highest occupied molecular orbital (HOMO). Since it is located mostly at the carbon atom, CO adsorbs as "carbon down".

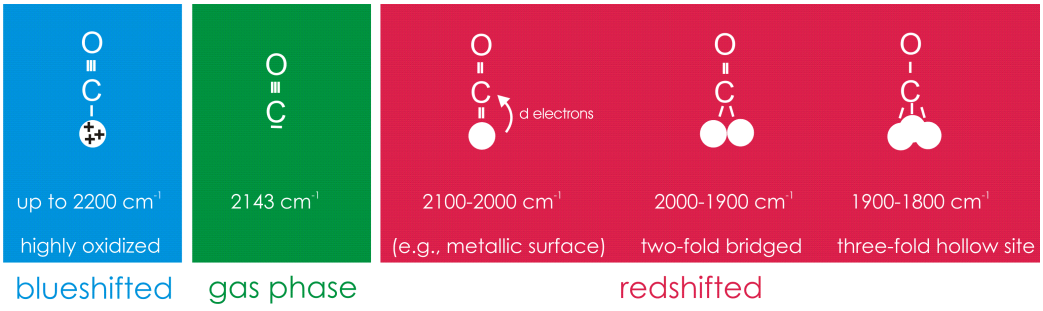

Figure 2.10: Chemical shifts of IR bands according to Blyholder [93]. Wavenumbers are provided by Hoffmann [92] (and references therein).

hence, also to a weaker oscillator strength of the carbonyl stretch. This leads to the observation of a redshift (i.e., to lower wavenumbers) with respect to the gas phase, while the opposite will cause a blueshift (i.e., to higher wavenumbers).

Redshifts are indicative for both a coordination of CO to several surface atoms at once and/or donation of d electron density from the surface into the C/surface bond. This back-donation depends on availability of d electrons, and hence, on the oxidation state of the adsorption site(s). If no or only few d electrons are present on a highly oxidized adsorption site, or if a high adsorbate coverage imposes additional competition for the available d electrons, a blueshift is more likely to be observed. The extents of these chemical shifts are summarized in Figure 2.10, along the lines of Hoffmann [92] (and references therein). Other effects may also cause an IR band to shift, as outlined in the following. If charge transfer takes place between the surface and the adsorbate, this additional electrostatic interaction may, e.g., redshift a CO band by up to 20 cm^{-1}, as calculated by Efrima and Metiu [95]. The "wall effect" accounts for the fact that adsorbates vibrate against a rigid surface, which leads to mass re-normalization and thereby to a blueshift [92]. As shown in Figure 2.8, the dipole moment of the adsorbate induces an image of itself within the surface. Provided the image is capable of following the dynamics of the original on the same time scale, the coupling between the two induces a redshift, which is called the polarization effect. Finally, dipole-dipole interactions must be considered; e.g., between adjacent molecules in the adsorbate phase. The shift depends, i.a., on intermolecular spacing, angular orientation and the number of individual dipoles contributing. This effect applies to adatom structures as well, such as vanadyl-terminated vanadia particles (see discussion of IRAS results in Section 5.4.1). The shift observed in an IRAS experiment, however, must be considered as a superposition of all of the above influences.

It is important to note that IRAS intensities do not always reflect the abundances of the corresponding species. Even for two identical molecules in the gas phase (hence, with identical dipole moments) that adsorb on inequivalent surface sites, this statement does not hold in general. It is possible for the band at higher wavenumber to "borrow" some of the intensity of the other peak, if the corresponding wavenumbers are sufficiently close to each other (100 cm^{-1} or less) [96]. Due to this effect, the less abundant species may even give rise to a band that is more intense than the one of the more abundant species, essentially exacerbating data analysis.

2.7 Electron Energy Loss Spectroscopy

Electron Energy Loss Spectroscopy, EELS, is a spectroscopy method based on the loss of kinetic energy of electrons. In principle, it spans the range from vibrational to electronic transition, but throughout this work, it was used exclusively as another vibrational spectroscopy. This variant is named High Resolution Electron Energy Loss Spectroscopy, HREELS.

Although both IRAS and HREELS detect vibrational transitions, they differ in several ways. The most striking difference is the energy range covered: HREELS is ideally suited for the study of phonons, in particular those of transition metal oxides, which consist of relatively heavy atoms, and are therefore associated with low wavenumbers. While the IR spectrometer used here, a Bruker IFS 66 v/S, has a detection limit of 560 cm^{-1} at the low end of the spectrum, it is an intrinsic property of HREEL spectra that $\tilde{\nu} = 0$ cm^{-1} is always included, because this is the position of the elastic peak. As a consequence, IRAS is better suited for the study of adsorbates, while HREELS is better suited for the study of phonons (lattice vibrations).

EELS is based on the loss of kinetic energy of electrons that are scattered on the surface. The primary electrons are generated by a filament, which have a primary kinetic energy, $E_{primary}$, of 5 eV in the case of HREELS. Since HREELS data are given in meV and IRAS data in cm^{-1}, the numbers must be converted for comparison. The conversion factor is 8.061 $\frac{cm^{-1}}{meV}$.

A two-stage monochromator (pre- and main monochromator) ensures that the distribution of the kinetic energy in the primary beam is as narrow as possible, since its full width at half maximum, FWHM, determines the resolution. Both monochomators consist of a set of electrostatic lenses that guide the electrons on a sectorial path, with opposite curvatures. A schematic representation of the setup of the VSI Delta 0.5 used in the present work is given in Figure 2.11. The terrestrial magnetic field makes μ-metal shielding neccessary, as presented for LEED (see Section 2.3).

When the electrons are scattered from the sample, a specific amount, E_{loss}, of their kinetic energy is transferred into vibrational modes of the sample. The reflected electrons then have to pass the analyzer stage (another sectorial set of electrostatic lenses), the pass energy, E_{pass}, of which is variable. After that, they are detected by a channeltron.

The electron yield is thus counted as a function of E_{pass}, which establishes the intensity, I, (i.e., the electron count rate) as a function of E_{pass}. The equation

$$E_{loss} = E_{primary} - E_{pass} \tag{2.21}$$

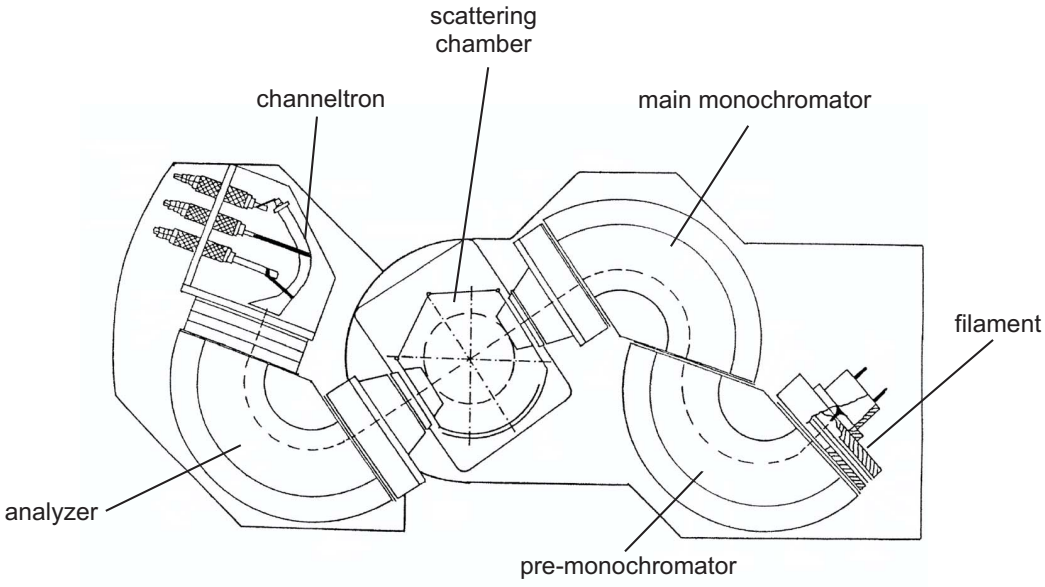

Figure 2.11: Schematic of the VSI Delta 0.5 HREELS spectrometer (adapted from [97]). The analyzer section can me rotated with respect to the scattering chamber.

transforms the count rate into a function of E_{loss}, which is the actual HREEL spectrum.

Note that inelastic scattering, i.e., transferring kinetic energy to vibrational modes of the sample, is much less probable than simple elastic scattering with only transfer of momentum, but without any energy transfer at all. This is why the peak at zero energy loss is always by far the biggest peak in the spectrum.

However, the intensity of the elastic peak may vary between different spectra, because the experimental condition of the HREEL spectrometer may change over time. Therefore, the spectra can only be compared after normalization with respect to the elastic peak; i.e., the spectra need to be scaled, such that the elastic peaks have the same intensity. For this reason, the elastic peak at 0 cm^{-1} is always included into the spectrum, as mentioned in the beginning of this Section.

Three principal inelastic processes can be distinguished, two of which reflect the particle-wave duality of the electrons. The electron may interact with the surface as an electromagnetic wave via the dipole scattering; i.e., similar to the scattering of light. Accordingly, the IRAS selection rules apply to the dipole scattering, including the MSSR (see Section 2.6.3). However, since electrons bear a non-zero rest mass, they can also exchange a momentum with the surface, thus giving rise to the impact scattering peaks. Moreover, in a mechanism called negative ion resonance, it is possible that an unoccupied electronic state on the sample with an energy in the range of the energy of the primary electron beam (5 eV in this work), traps an electron from the beam in a very short-lived state (between 10^{-15} s and 10^{-10} s). In general, the equilibrium of the internuclear distance in the newly created anion and the formerly neutral species are different, which results in a vibration, when the anion attempts to assume the new equilibrium distance. Once the short-lived anion decays, the direction, in which the electron is ejected, is determined by the symmetry of the orbital it had occupied. Hence, the detection of such electrons generally requires off-specular measurement. Dipole scattering is a relatively long-ranged interaction (60 Å from the surface), while impact scattering and negative ion resonance require a close proximity between the electron and the sample.

Finally, it should be mentioned that the "high resolution" of HREELS holds true in comparision with EELS, but not with IRAS. Using the above-mentioned unit conversion factor, a FWHM of 2.5 meV, which would be considered as very good for HREELS measurements, correspond to more than 20 cm^{-1}. The resolution in the IRAS experiments, however, is 2 cm^{-1}; hence, superior by at least one order of magnitude.

2.8 Temperature Programmed Desorption

The adsorption behavior of molecules on a surface can be studied by Temperature Programmed Desorption, TPD, which is also referred to as Thermal Desorption Spectroscopy, TDS. In these experiments, the sample is exposed to a gas. Subsequently, it is heated, while the desorbing species are monitored by a mass spectrometer. The principal functionality of a quadrupole mass spectrometer, which is used for TPD experiments in this work, is discussed below.

Two main ways of adsorption are distinguished. Physisorption is based on the merely electrostatic interaction between temporary dipole moments in the surface and the adsorbate that makes the molecule stick to the surface (i.e., van der Waals interactions). This attractive force is counterbalanced by the Pauli repulsion [98]. Hence, the physisorbed molecule remains at an equilibrium distance, where the two effects just cancel each other out. Chemisorption, on the other hand, requires the formation of chemical bonds between the adsorbate and the surface. The energy threshold between physisorption and chemisorption is commonly accepted to be in the order of 50 kJ mol^{-1}; i.e., 0.5 eV per molecule. The chemisorbed molecule may stay intact (molecular chemisorption), or it may dissociate (dissociative chemisorption), if at least one intramolecular bond in the adsorbate is sufficiently weakened by the adsorption process. Dissociative chemisorption can be activated or non-activated. Since chemisorption of CO occurs molecularly (on the surfaces discussed within this work), it can be used as a probe molecule, which is discussed in detail in Section 2.6.3. The oxidation of methanol to formaldehyde (see Section 5.4.2) can be named as an example for dissociative chemisorption within this work. In this case, the method is called Temperature Programmed Reaction, TPR.

In TPD experiments, the adsorption energy is measured indirectly, since they actually monitor the reverse process. The energetics of adsorption kinetics can be obtained by analysis of TPD data, as presented in the literature [99–103]. The first complete analysis was given by King [100]. In the Wigner-Polanyi model, it is assumed that the rate of desorption, $-\left(\frac{d\theta}{dt}\right)$ (where θ is the coverage), of a given species from the surface is as follows:

$$-\left(\frac{d\theta}{dt}\right) = \nu\ \theta^n\ e^{-\left(\frac{E_{des}}{RT}\right)} \tag{2.22}$$

where E_{des} is the energy needed to activate the desorption, t is the time, $R = 8.314$ J K^{-1} mol^{-1} is the universal gas constant, T is the temperature, θ is the coverage (varying between 0 and 1), and ν is the pre-exponential frequency factor. The order of the desorption process is determined by the exponent n

of θ^n. Three cases of $n = 0$, $n = 1$ and $n = 2$ are typically distinguished; i.e., zero-order, first-order and second-order desorption.

In many cases, $\nu = 10^{13}$ s^{-1} is a good estimate. Desorption (i.e., $-\left(\frac{d\theta}{dt}\right)$) occurs upon heating the sample. Hence, θ is a function of temperature, which itself is a function of time in this case. Assuming a constant heating rate $\left(\frac{dT(t)}{dt}\right) = \beta$, in order to facilitate data analysis (the use of a feedback controller provides $\frac{\Delta\beta}{\beta} = \pm 1\%$), equation 2.22 can be rewritten as:

$$-\left(\frac{d\theta}{dT}\right) = \frac{\nu}{\beta}\ \theta^n\ e^{-\left(\frac{E_{des}}{RT}\right)} \tag{2.23}$$

Zero-order desorption takes place, if the desorption rate does not depend on the coverage. The spectra are typically asymetric and show all the same leading edge, while the temperature of maximum desorption shifts to higher values with increasing initial coverage. First-order desorption spectra have symmetric line shapes, the peak temperature of which is independent of the initial coverage. According to Redhead [99], E_{des} can then be calculated as follows:

$$E_{des} = RT_{max}\ (ln(\nu\ T_{max}) - ln(\beta) - 3.64) \tag{2.24}$$

Second-order desorption ($n = 2$) is typical for dissociative adsorption. In this case, the peaks are symmetric, and the temperature at maximum desorption shifts to lower values with increasing intial coverage. Habenschaden and Küppers established leading-edge analysis for this case [101].

Besides the feedback controller for controlled heating, a quadrupole mass spectrometer, QMS, is needed for the detection of desorbed species. A HIDEN HAL RC 201 was used in the present work. A QMS consists of three principal stages: the ion source, the quadrupole filter, and the detector. The ion source ionizes the entering gas molecules. The quadrupole consists of four electrodes that are arranged parallel to the flight path of the ions. This unit acts as a filter that allows only ions with certain $\frac{m}{z}$ to travel across to the detector, where m is the ion mass, and z is the number of elementary charges the ion possesses. The filtering relies on the application of an AC voltage between the four poles, with neighboring poles having always opposite polarity. While a given frequency of the AC voltage allows one specific $\frac{m}{z}$ value to pass, all others are ejected. The frequency, however, is varied rapidly, such that multiple $\frac{m}{z}$ values can be detected within the fraction of a second. The dwell and settle time intervals for data sampling can be adjusted by the user. Typical values for the acquisition time for one data point of one ion species (i.e., one value for $\frac{m}{z}$) range between 10 ms and 100 ms. The ions

are detected by a secondary electron multiplier, SEM, the signal output of which is further amplified electronically.

The HIDEN HAL RC 201 records mass signals as functions of time. It is also capable of tracking the temperature signal that it receives from the feedback controller. Using a spreadsheet software, the mass signals can be converted into functions of temperature.

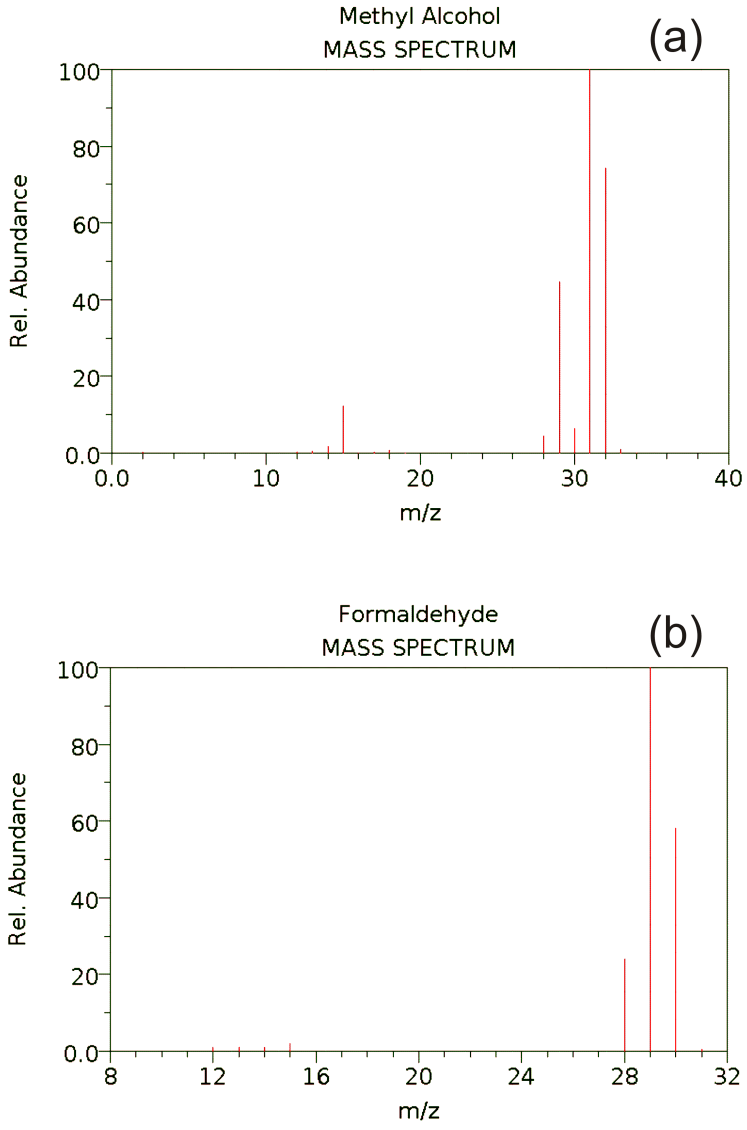

Figure 2.12: fragmentation pattern of (a) methanol and (b) formaldehyde at an ionization voltage of 70 V (from NIST webbook [104])

Depending on the voltage used in the ion source, the molecule may be fragmented prior to detection. This means that, e.g., methanol, which has a relative mass of 32 a.m.u., is not detected at $\frac{m}{z} = 32$. Instead, the main peak for methanol at an ionization voltage of 70 V is reported to be $\frac{m}{z} = 31$ (see Figure 2.12 (a)), indicating fragmentation. Moreover, the second most intense fragment is located at $\frac{m}{z} = 29$. Note that a formaldehyde fragment is also detected at this value (see Figure 2.12 (b)), which is why the methanol contribution has to be subtracted, in order to monitor formaldehyde desorption.

The mass spectrometer signals $I_{31}^{CH_3OH}$ at $\frac{m}{z} = 31$ and $I_{29}^{CH_2O}$ at $\frac{m}{z} = 29$ were selected to represent methanol and formaldehyde, respectively, because they are the most abundant ones. The contribution of methanol $I_{29}^{CH_3OH}$ to the overall intensity of $\frac{m}{z} = 29$, I_{29} is subtracted:

$$I_{29}^{CH_2O} = I_{29} - I_{29}^{CH_3OH} \tag{2.25}$$

Since $I_{29}^{CH_3OH}$ is not directly accessible, it needs to be expressed relative to $I_{31}^{CH_3OH}$, which is in turn the only contribution to I_{31} and thus directly measurable ($I_{31}^{CH_3OH} = I_{31}$).

$$I_{29}^{CH_2O} = I_{29} - \left(\frac{I_{29}^{CH_3OH}}{I_{31}^{CH_3OH}} \right) I_{31} \tag{2.26}$$

The TPR from pristine ceria does not show formaldehyde formation over the relatively broad range of 250 K - 500 K. Hence, the ratio $\frac{I_{29}^{CH_3OH}}{I_{31}^{CH_3OH}}$ is equal to $\frac{I_{29}}{I_{31}}$ in this case. For this spectrum, $\frac{I_{29}}{I_{31}}$ was calculated for each data point between 250 K and 500 K and subsequently averaged This yielded 0.7, which was then inserted into equation 2.26. All TPR data of formaldehyde presented in Section 5.4.2 were subject to this refinement.

Chapter 3

Niobia Films as Oxide Support

As stated in Chapter 1, niobia is used as a support in the Fischer-Tropsch process, where it enhances the selectivity toward high-molecular weight products. To understand the role of niobia as the support, niobia films as model catalysts were prepared for the first time. Previous studies of Nb(100), Nb(110) and Nb(111) single crystal surfaces and Nb foils focussed on the formation of passivating films that may strongly affect the superconducting properties of Nb [105–110].

Several O-induced reconstructions of Nb surfaces are observed by LEED, depending on the preparation. For example, An *et al.* [109] observed a change from initial c(2×2) via (1×1) to amorphous. Annealing to 900 K lead to dissolution of O in the Nb bulk, with a concomitant surface ordering to (3×1). At 1500 K - 2500 K, however, the reverse process of O seggregation to the surface occurred, which lead to the formation of oxidized surfaces as well. Arfaoui *et al.* [107,108] were able to prepare NbO_x(111)-like nanocrystals (x = 0.8 - 1.2), which form tiled structures with many stacking faults on Nb(110). Apparently, Nb may act as a storage for oxygen, from which uncertainties in the film thickness may arise eventually, due to the amount of oxygen available being unknown.

Petrucci *et al.* [111] grew thick films of niobium oxide (100 Å to 1.2 μm) on *z*-cut $LiNbO_3$ by Molecular Beam Epitaxy, MBE, which were studied by Reflection High Energy Electron Diffraction, RHEED, and ex-situ XPS. At first, Nb^{2+} and Nb^{5+} were found to coexist, but after an additional oxidation at 450 ℃ for 1h only Nb^{5+} prevailed. Preparation on z-cut sapphire (Al_2O_3) at 650 ℃ in a low flux of O_2/Nb yielded perfect RHEED reflections attributable to $NbO_{0.8}$(111). Further annealing at 420 ℃ in dry O_2 for 3h converted it to polycrystalline Nb_2O_5.

Xie *et al.* [112, 113] used Pt(111) as a substrate. Niobium oxide was grown in repeated cycles of deposition of 0.1 monolayer Nb and oxidation at

700 K in 10^{-6} to 10^{-5} mbar O_2, ; however, only at submonolayer coverage, sharp LEED spots could be obtained, while it revealed poor crystallinity otherwise. Using AES, HREELS and UPS, the authors concluded that the stoichiometry would be NbO, NbO_2 or Nb_2O_5, depending on the preparation conditions. An HREELS band at 926 cm^{-1} was attributed to the stretching of niobyl (Nb=O) groups. Yet the lack of order in the films, in addition to the absence of morphological studies, renders the correlation between structure and spectroscopy questionable.

3.1 Monolayer Niobia Films

First attempts on the preparation of well-ordered niobium oxide films at the Department of Chemical Physics of the Fritz Haber Institute, Berlin, were done along the lines of Niehus and co-workers [114–116], who prepared vanadium oxide on an oxygen-implanted $Cu_3Au(100)$ substrate. This approach seems proximate, as vanadium and niobium are homologues of Group 5 of the Periodic Table of Elements (see Figure 1.2).

3.1.1 Preparation

A $Cu_3Au(100)$ single crystal (from Mateck) is used as the substrate for the growth of niobia films. The surface of this sample is cleaned by cycles of sputtering and annealing (800 K, 5 min). This is repeated until the LEED pattern was of a sufficient quality, as shown in Figure 3.1 (a). The clean $Cu_3Au(100)$ sample is then sputtered with O_2 (2×10^{-5} mbar, 300 K, 1 keV), which implants oxygen into $Cu_3Au(100)$, and subsequently annealed (650 K, 5 min) to smoothen the surface. In general, it is necessary to allow the pressure in the chamber to recover after such high O_2 exposures. Niobium is vapor deposited onto this surface from an Nb rod (2 mm diameter, from Goodfellow, 99.99% purity). The Nb flux was calibrated in terms of nominal thickness (see Section 2.2), using a quartz microbalance. After evaporation of 1.6 Å Nb, the sample is oxidized in 10^{-6} mbar O_2 at 780 K for 30 min in front of a calibrated gas doser. The quality of the film is verified by LEED. A successful preparation yields the LEED pattern depicted in Figure 3.1 (b).

3.1.2 Results and Discussion

LEED

The LEED pattern in Figure 3.1 (b) exhibits three sets of spots that are arranged in concentric twelve-membered rings, which are numbered from (1)

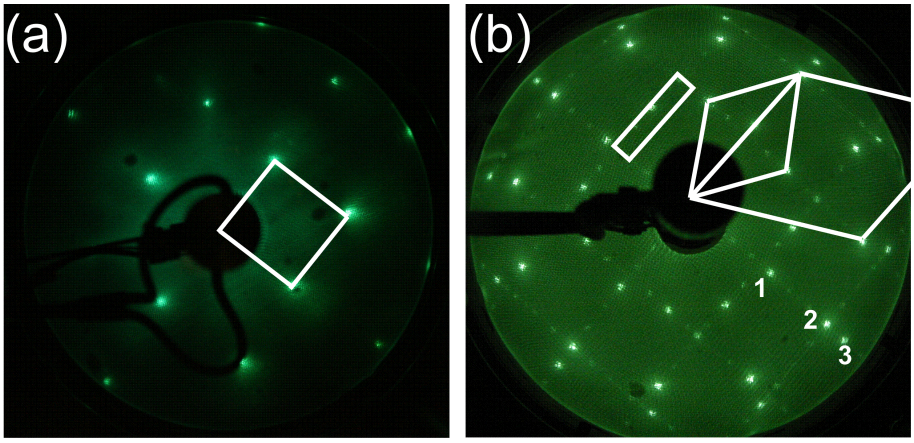

Figure 3.1: LEED patterns (70 eV) of (a) clean $Cu_3Au(100)$ and (b) monolayer $Nb_2O_5/Cu_3Au(100)$. The numbers 1-3 in (b) denote the observed rings in the LEED pattern. The unit cells are indicated. The additional rectangle in (b) represents the coincidence structure, which is shown as a real space schematic in Figure 3.2.

to (3), respectively, from inside to outside. Ring (3) is formed by second order diffraction spots of ring (1). Such a pattern is typical for hexagonally symmetric surfaces that exist in two domains, which are rotated by either 30° or 90° with respect to each other. Since the $Cu_3Au(100)$ substrate has square symmetry, perpendicular domains are considered as most likely. For each domain, two of the six hexagonal spots of ring (2) coincide with the (1×1) substrate spots, indicating a good epitactical relationship between the film and the substrate, as previously reported for several metal oxides of the MO(111) type [117–119]. Hence, ring (2) is assigned to the O sublattice of the niobia film, which is expressed in real space as:

$$\begin{pmatrix} \vec{A'} \\ \vec{B'} \end{pmatrix} = \begin{pmatrix} 1 & \frac{-1}{\sqrt{3}} \\ 0 & \frac{2}{\sqrt{3}} \end{pmatrix} \begin{pmatrix} \vec{A} \\ \vec{B} \end{pmatrix} \tag{3.1}$$

where $\vec{A}$ and $\vec{B}$ are the unit vectors of $Cu_3Au(100)$, while $\vec{A'}$ and $\vec{B'}$ are the unit vectors of the O sublattice. Since the shortest interatomic distance in $Cu_3Au(100)$ is 2.65 Å, equation 3.1 yields 3.1 Å for the shortest distance in the O sublattice, which is quite reasonable for thin oxide films. Taking into account the $(\sqrt{3} \times \sqrt{3})R30°$ relationship between ring (1) and ring (2), 5.4 Å are obtained for the real space equivalent of ring (1).

Additionally, there is a large number of spots running along the {110} and $\{\bar{1}10\}$ directions of the substrate. These spots are rather weak, and they

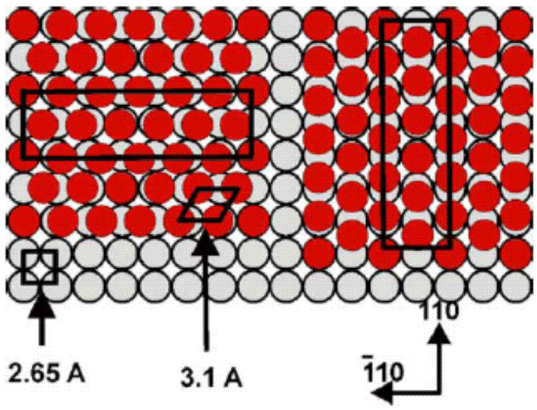

Figure 3.2: Schematic representation of the (2×7) coincidence structure formed between the square lattice with a_{110} = 2.65 Å of the metallic substrate and the hexagonal lattice with a_{111} = 3.1 Å of the oxide film. Two domains can be formed through rotation by 90° of the hexagonal lattice as indicated.

originate most likely from a coincidence structure of the square symmetry of $Cu_3Au(100)$ and the hexagonal symmetry of the niobia film. The observed (2×7) periodicity, along with the shortest interatomic distance of 2.65 Å, yields

$$2 \times 2.65 \text{ Å} = 5.3 \text{ Å} \tag{3.2}$$

and

$$7 \times 2.65 \text{ Å} = 18.55 \text{ Å} \tag{3.3}$$

as the common multiples between the characteristic lengths of the substrate and the film. It is

$$1 \times 5.4 \text{ Å} \approx 5.3 \text{ Å} \tag{3.4}$$

and

$$6 \times 3.1 \text{ Å} = 18.6 \text{ Å} \approx 18.55 \text{ Å} \tag{3.5}$$

Hence, every seventh substrate atom coincides with every sixth atom of the O sublattice in the $\{\bar{1}10\}$ direction, and every second substrate atom coincides with an O atom in the $\{110\}$ direction. The resulting coincidence structure is depicted in Figure 3.2.

STM

STM results presented in Figure 3.3 were provided by D.E. Starr. The observation in STM of the substrate being fully covered occurred at the equivalent of 0.7 ML Nb. Figure 3.3 (a) reveals atomic protrusions with a periodicity of $\sim$ 5.5 Å, which is in a good agreement with the 5.4 Å identified as the characteristic length for ring (1). Missing protrusions, imaged as dark spots, are interpreted as defects. Figure 3.3 (b) shows a long-range modulation (corrugation amplitude less than 0.2 Å), which appears as stripes. The stripes follow two principal directions that are perpendicular with respect to each other, which corresponds to the observation of two domains, as made by LEED. The apparent height of the film at low NbO_x coverage was measured to be $\sim$ 2.5 Å. Although the oxidic film has a higher work function than the metallic substrate, which may lead to an underestimation of the film thickness, this number is certainly indicative for a small thickness.

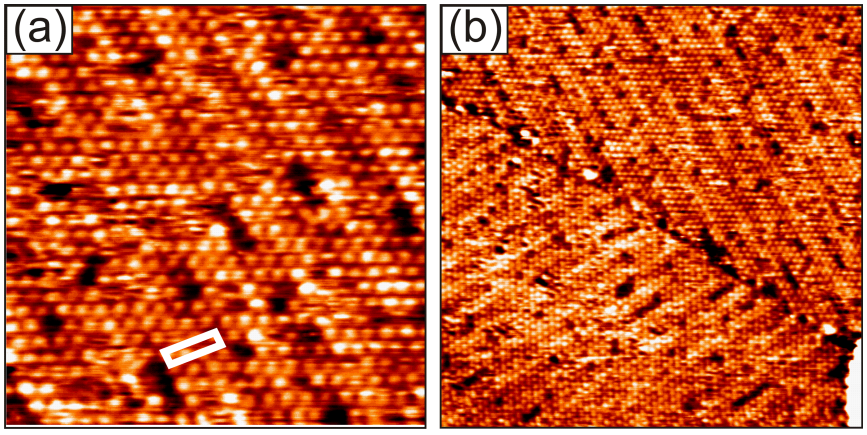

Figure 3.3: (a) STM of monolayer niobia films grown on $Cu_3Au(100)$, V = 1.4 V, I = 1.0 nA, 15×15 nm^2, the white box indicates the surface modulation; (b) STM of monolayer niobia films grown on $Cu_3Au(100)$, V = 1.4 V, I = 1.0 nA, 40×40 nm^2. (Data provided by D.E. Starr)

PES

Figure 3.4 presents PES data of the films in the Nb 3d, the O 1s and the valence band regions (provided by D.E. Starr). Detection angles of both 0° and 70° with respect to the surface normal were utilized. The Nb $3d_{5/2}$ level was chosen to represent spin-orbit split Nb 3d. The single Nb peak centered at 206.4 eV indicates the presence of only one Nb species. Its relative intensity

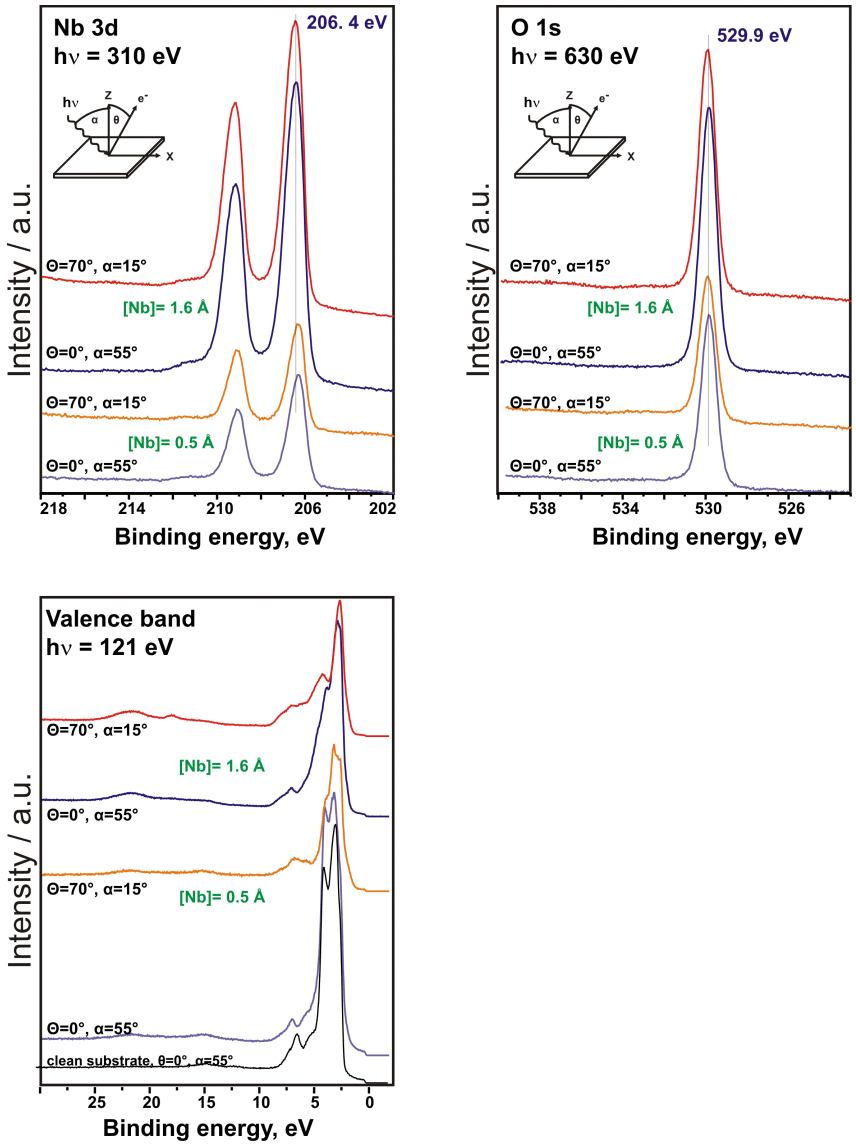

Figure 3.4: PES data of monolayer niobia films grown on $Cu_3Au(100)$ (Nb $3d$, O $1s$, valence band). The spectra are offset for clarity. (Data provided by D.E. Starr.)

is independent of the detection angle, revealing that this species is located in the surface region. According to a review by Halbritter [120] and a more recent publication by Morris *et al.* [121], Nb exhibits binding energies of 205.8 eV and 207.5 eV for Nb^{4+} and Nb^{5+}, respectively, by which the measured value of 206.4 eV is framed. However, in the case of very thin oxide films, the binding energy of the core electrons may be lowered as compared to thicker films and bulk systems due to the screening of the core hole in the final state by metal substrate electrons (see also Section 2.4). Inspection of the spectra at the O 1*s* level does not clarify the situation. The measured 529.9 eV are close to many values reported for transition metal oxides. It is assumed that, similar to the oxides of the homologous vanadium, the O 1*s* peak does not shift considerably as a function of the oxidation state of the metal [122].

In principle, the valence band region is suited to discriminate between NbO_2 and Nb_2O_5. Since the latter is an insulator with a band gap of 3.4 eV and the former a semiconductor, the presence of a feature near the Fermi edge can provide the desired distinction. According to Morris *et al.*, the additional $4d^1$ electron of NbO_2 gives rise to a well-resolved peak at 1.3 eV. Another broad peak in the valence band region of NbO_2 from 4 eV to 10 eV is attributed mainly to the O 2*p* levels. The valence band spectra for the present study, however, does not resemble bulk spectra of either NbO_2 or Nb_2O_5. While there is some intensity at $\sim$ 2.5 eV, it is plausible that the electronic structure of the present thin film differs from the ones of bulk samples. As a conclusion, the lower binding energy attributed to a final state effect and the lack of intensity at 1.3 eV suggest the oxidation state Nb^{5+}, implying a Nb_2O_5 stoichiometry.

This result is used for further discussion of the LEED observations. Assuming one close-packed layer of each O and Nb, the stoichiometry would be NbO, and the $(\sqrt{3} \times \sqrt{3})$R30° structure would not appear in LEED. Removing one-third or two-third of this thought close-packed niobium layer, such that the $(\sqrt{3} \times \sqrt{3})$R30° pattern would appear, would lead to stoichiometries (Nb_2O_3 or NbO_3, respectively) that are at variance with the PES results. Hence, another O layer atop Nb is required, stacked as (Cu_3Au)-O-Nb-O. Reducing the filling of either of the two O layers by one-third or two-third results again in a stoichiometry inconsistent with PES, which is why the $(\sqrt{3} \times \sqrt{3})$R30° structure must arise from an incompletely filled Nb layer. Taking into account a nominal film thickness that is equivalent to $\sim$ 0.7 ML Nb fully covered the $Cu_3Au(100)$ substrate, it is concluded that the Nb layer is filled by two-third. In order to fulfill the stoichiometric ratio of [Nb]:[O] = 2:5, the overall O content in the film must add up to five-third of one close-packed layer. Since the bottom O layer, which is stacked between the substrate and Nb, is assumed to be close-packed, two-third remain for the top

O layer. Such sandwich structures are known to have a low net dipole moment normal to the surface, which renders them thermodynamically stable, according to Tasker [123].

LEED results indicate that the Nb layer and the bottom O layer are in $(\sqrt{3} \times \sqrt{3})$R30° registry with respect to each other. However, no further coincidence structure is observed, which is why the Nb layer and the top O layer must exhibit the same symmetry. Since both contain the same number of atoms, there are only two possibilities to arrange them: O sits either on top of Nb, or it sits in the three-fold hollow sites of the Nb layer.

Computational Results

Density functional theory, DFT, calculations done by D. Lahav investigated the stability of a total of four stacking arrangements of (bottom O)-Nb-(top O): (i) all three on top of each other - AAA; (ii) Nb in the hollow sites of bottom O, but top O atop Nb - ABB; (iii) Nb in the hollow sites of bottom O, top O in the hollow sites of Nb, top O not in registry with bottom O - ABC; (iv) Nb in the hollow sites of bottom O, top O in the hollow sites of Nb, top O in registry with bottom O - ABA. After geometry optimization, AAA and ABB turned out to be the energetically least favorable structures. On the contrary to this, the other two converged to the same structure, where the top O layer is bridging the Nb atoms.

In this situation, the distances between the top O layer and the Nb layer and between the Nb layer and the bottom O layer are ~ 1 Å and ~ 1.2 Å, respectively. Adding the 2 Å that were kept fixed for the distance between the bottom O layer and the substrate, the total film thickness amounts to ~ 4 Å, which agrees qualitatively with the 2.5 Å found as the apparent height in STM.

On the basis of calculated density of states, STM images of the most stable structure at experimental tunneling conditions were simulated following the Tersoff-Hamann approach [86]. As shown in Figure 3.5, simulation and experiment agree well, as also the 5.4 Å periodicity is reproduced in the simulation. The calculations reveal that the protrusions originate from unoccupied d states of Nb located between two Nb atoms (Figure 3.5 (a)). As concluded from Figure 3.5 (c), there is no charge re-distribution, and hence, no direct interaction between these two Nb atoms. The protrusions are therefore assigned to arise from pairs of open Nb atoms that do not exhibit a bridging O atom, which would actually screen these states.

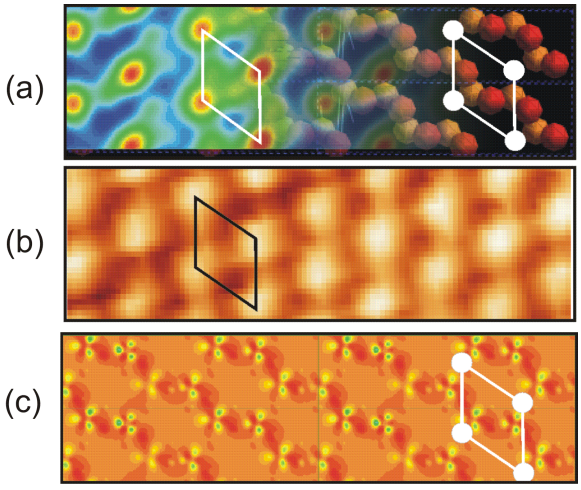

Figure 3.5: (a) Simulated and (b) experimental STM images, provided by D.E. Starr and D. Lahav, respectively. The simulated image is superimposed with the positions of surface atoms in the model ($V = 1$ V, tip-sample distance set to 3 Å) in the simulation. (c) The corresponding charge difference plot in the plane of the Nb layer. The positions of STM protrusions over the surface are indicated by filled circles. The unit cell is indicated.

HREELS

The HREEL spectrum of $Nb_2O_5/Cu_3Au(100)$ given in Figure 3.6 corroborates the DFT results. It exhibits three peaks, which are located at 703 cm^{-1}, 870 cm^{-1} and 1406 cm^{-1}, respectively. The one at 703 cm^{-1} is the prevalent feature, to which the one at 1406 cm^{-1} is an overtone. The main peak is tentatively assigned to asymetric O(top)-Nb-O(bottom) vibrations, which is consistent with the O atoms of the top layer bridging the Nb atoms. For vanadia, bridging surface oxygen was found between 630 cm^{-1} and 740 cm^{-1} by Sock *et al.* [91].

In particular, the 900 cm^{-1} - 1000 cm^{-1} region, which is characteristic for stretching modes of O atop a metal, is essentially featureless. In Section 3.2.2, which deals with the HREEL spectra of the multilayer niobia films grown on $Cu_3Au(100)$, a band at 984 cm^{-1} is assigned to the stretching mode of niobyl groups. This band is observed as well for alumina-supported niobia particles, which are discussed in Section 4.2.2. Note that no intensity could be observed in the niobyl stretch region in complementary IRAS experiments, either (not shown). The weak feature at 870 cm^{-1} is a shoulder to the main peak. It may indicate a minor concentration of Nb/O stretching modes arising from distorted NbO_6 octahedra [22], which are the building blocks of niobia, and

hence, lend insight into the defectivity of the film. This is supported by the HREEL spectra of the oxidized and reduced multilayer niobia films presented in Figure 3.11, where a band at 842 cm^{-1} becomes prevalent after annealing the sample to 900 K for 5 min in UHV. The latter treatment is thought to result in the loss of O and thus possibly in structural changes.

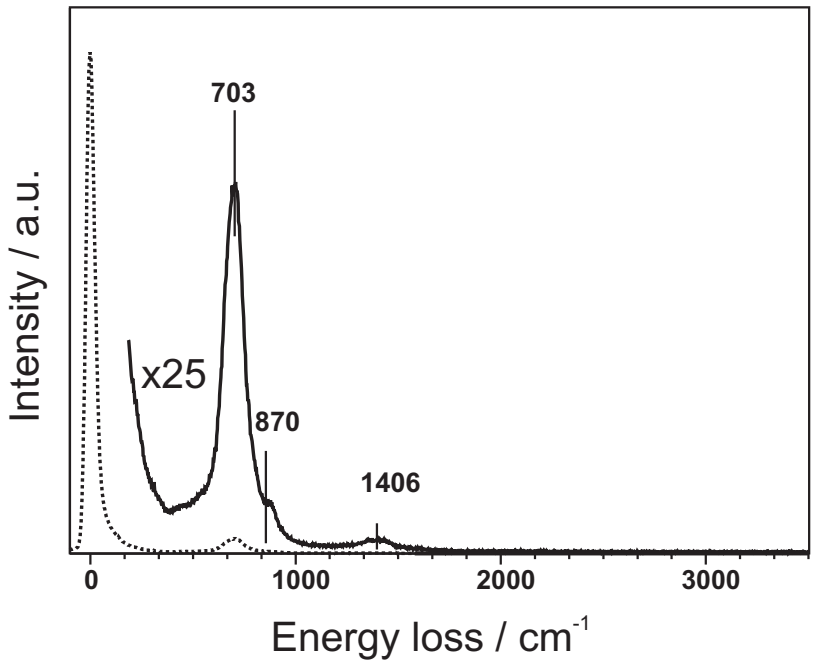

Figure 3.6: HREELS of monolayer $Nb_2O_5/Cu_3Au(100)$

CO Adsorption

The surface of the monolayer $Nb_2O_5/Cu_3Au(100)$ films was further probed by CO adsorption. TPD and IRAS data are presented in Figure 3.7. The TPD spectrum (Figure 3.7 (a)) has no common feature with the one for CO on clean $Cu_3Au(100)$ (which exhibits only one peak at 142 K), indicating that the film is free of holes, through which the substrate would be exposed. O-precovered $Cu_3Au(100)$, the intermediate surface before Nb deposition, seems to be totally inert toward CO adsorption.

There are three desorption species from the niobia films, at 125, 155 and 272 K. These spectra could be repeated for several runs of CO adsorption and desorption, and no CO_2 formation was observed. It is concluded that, under these conditions, CO adsorbs molecularly on the film and is unable to reduce it. The highest desorption temperature, approximately 270 K, is

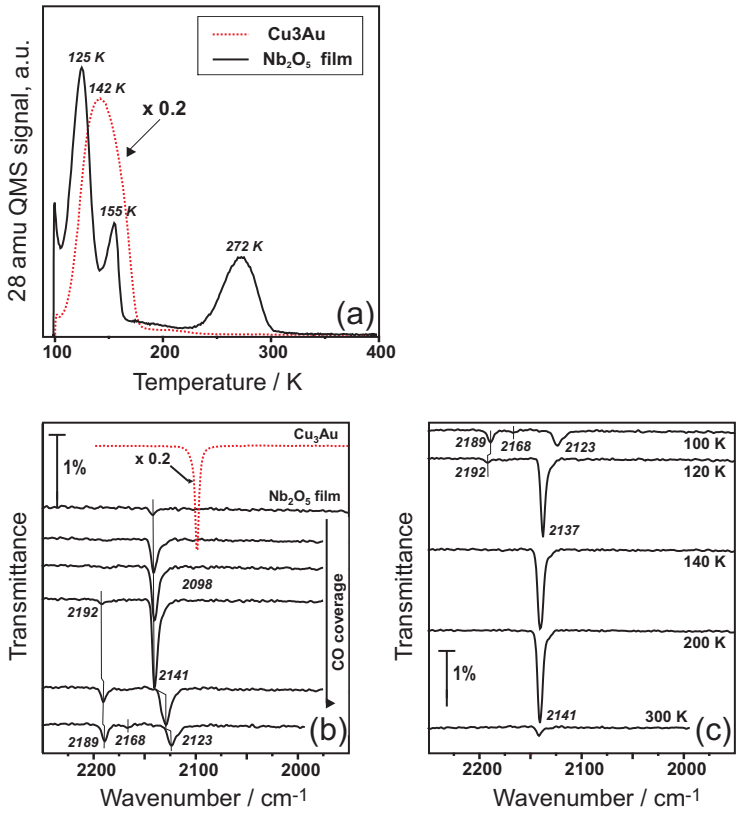

Figure 3.7: (a) CO TPD from monolayer niobia films (dotted red line: CO TPD from $Cu_3Au(100)$). (b) CO IRAS (increasing exposure) on monolayer niobia films (dotted red line: CO IRAS of $Cu_3Au(100)$). (c) CO IRAS (flashing series) of monolayer niobia films. IR spectra are offset for clarity.

unusually high, since the desorption temperature of CO from various oxides ranges below 200 K [124]. An assignment to CO on metallic Nb is ruled out, as the respective desorption temperature was reported to be $\sim$ 425 K [125].

Complementary IRAS measurements were conducted, and the spectra are shown in Figure 3.7 (b) and (c). Figure 3.7 (b) depicts the spectra for increasing CO coverage. For comparison, it shows IR data of CO on $Cu_3Au(100)$ as well; there is only one peak at 2098 cm^{-1}, with a strong intensity. The wavenumber and the intensity are both typical for CO on a metallic substrate [96]. The presence of gold in Cu_3Au apparently weakens the interaction of CO with the substrate as compared to Cu(100), which is reflected by a lower desorption temperature and a higher wavenumber of the C/O stretching mode (200 K [126], 2072 cm^{-1} [127]).

Upon CO adsorption on the niobia film, a peak at 2141 cm^{-1} first gains

intensity with increasing exposure, but then loses intensity and simultaneously shifts to 2123 cm^{-1} at saturation coverage. Meanwhile, a signal of low intensity emerges at 2192 cm^{-1}, which shifts to 2189 cm^{-1} at saturation coverage. At the saturation level, one more peak appears at 2168 cm^{-1}. The coverage-dependence of the 2141-2123 cm^{-1} peak indicates an interaction between the CO molecules and can be understood on the basis of redistribution of the adsorption sites with increasing coverage [128].

Figure 3.7 (c) shows IR spectra of CO adsorption after thermal flashes to the indicated temperature. The sample spectra were taken at 100 K, as the reference spectrum was taken at this temperature as well. The two CO species with the highest stretching wavenumbers, 2191 cm^{-1} and 2168 cm^{-1}, desorb below 140 K, which is in agreement with the desorption temperature of 125 K found in TPD. Heating to 200 K increases the intensity of only the 2141 cm^{-1} peak slightly, but does not lead to the loss of any IRAS band, from which it is concluded that the CO species desorbing at 155 K is inactive for detection by IRAS. The main peak at 2141 cm^{-1} desorbs between 200 and 300 K, which matches well the desorption at 272 K.

For the understanding of these results the integrated TPD peak areas of CO adsorbed on $Nb_2O_5/Cu_3Au(100)$ and on $Cu_3Au(100)$ must be compared. The saturation coverage of CO on $Cu_3Au(100)$ at 100 K is equivalent to 0.3 monolayers [128], but the integral TPD intensity of CO adsorbed on the niobia film is about five times smaller. This corresponds to an average of less than 0.2 CO molecules per niobia surface unit cell. Nevertheless, the strong coverage dependence of the wavenumber of the high temperature desorption species is a hint for strong intermolecular interactions. Therefore, it is most probable that CO adsorption does not occur on regular sites, but on extended defects, where the local CO concentration can be very high and thus lead to the aforementioned observations.

On the basis of the Blyholder model for CO adsorption [93] (see Section 2.6.3), the observed IR signals are assigned as follows: Beutel *et al.* observed a peak at 2191 cm^{-1} for silica-supported niobia particles and assign it to CO adsorbed on Nb^{5+}. The above PES results confirm this to be the sole Nb state. Accordingly, the main peak at 2141-2123 cm^{-1} should represent CO adsorbed on reduced sites, where the remainder of some d electron density can perform a back-donation from the surface to CO, which lowers the wavenumber, as described in Section 2.6.3. The unusually high desorption temperature of 272 K reflects a very strong adsorption typical for defects. The coverage-dependent wavenumber makes it a legitimate assumption that these defect sites are localized along step edges or domain boundaries, as observed from Figure 3.3 (b).

In a study of a similarly prepared niobia film, Höbel *et al.* observed two

peaks in their SFG spectra at 2118 and 2165 cm^{-1}, after exposing the film to 10^{-6} mbar CO at 100 K [129]. Their assignment for the 2118 cm^{-1} band is identical to the one presented here for the peak at 2123 cm^{-1}. Bearing in mind their high pressure (by comparison), the surface must certainly be saturated with CO, and hence, these two species must be equivalent. The respective second species (2191 cm^{-1} here vs. 2165 cm^{-1} for Höbel *et al.*) do not match, which may be due to slight differences in the preparation procedure. Höbel *et al.* performed a final anneal in UHV at 773 K, which was not done in the present study. However, a minute IR peak at 2168 cm^{-1} was found also in the present case. The explanation of Höbel *et al.* for this is CO adsorbed on regular terrace sites, although they admit that the film is O-terminated and therefore would not adsorb CO on regular sites in significant amounts. It appears more plausible that their additional anneal in UHV resulted in a partial reduction of the film and the creation of Nb^{4+} sites. The simultaneous absence of intensity at 2191 cm^{-1} could indicate that the reduction took place on sites that have been defective already beforehand. This would be consistent with the observation that annealing of the niobia multilayer films at 900 K in UHV for 5 min leads to the loss of some of the topmost O atoms, as observed in Figure 3.10 (b), and thus also to a reduction.

These CO adsorption studies reveal an essentially inert surface, indicating a termination by oxygen. One of the adsorption states, assigned to CO on Nb^{5+}, confirms the Nb_2O_5 stoichiometry concluded from PES. The main adsorption, however, exhibits a coverage-dependent wavenumber. Since the film was found to grow in two domains, as seen in Figure 3.3 (b), this state most likely represents adsorption along the domain boundaries, where intermolecular interactions of adsorbed CO would depend on the proximity between adjacent molecules and thus on the exposure.

3.1.3 Conclusions

The thin niobia film is shown to be a monolayer, which PES result reveal to be present as Nb_2O_5. Combining LEED, DFT and HREELS results, Nb is found to be framed by one O layer above and another one underneath. The O atoms in the top layer sit in bridging positions between the underlaying Nb. The films has hexagonal symmetry, but grows in two perpendicular domains.

These findings are consistent with the structural model shown in Figure 3.8. It must be mentioned that the model does not resemble any of the known (unreconstructed) bulk structures of Nb_2O_5. Indeed, it is quite conceivable that the structure of a monolayer film differs substantially from its bulk counterpart, as influences of the substrates may become non-negligible for

these films.

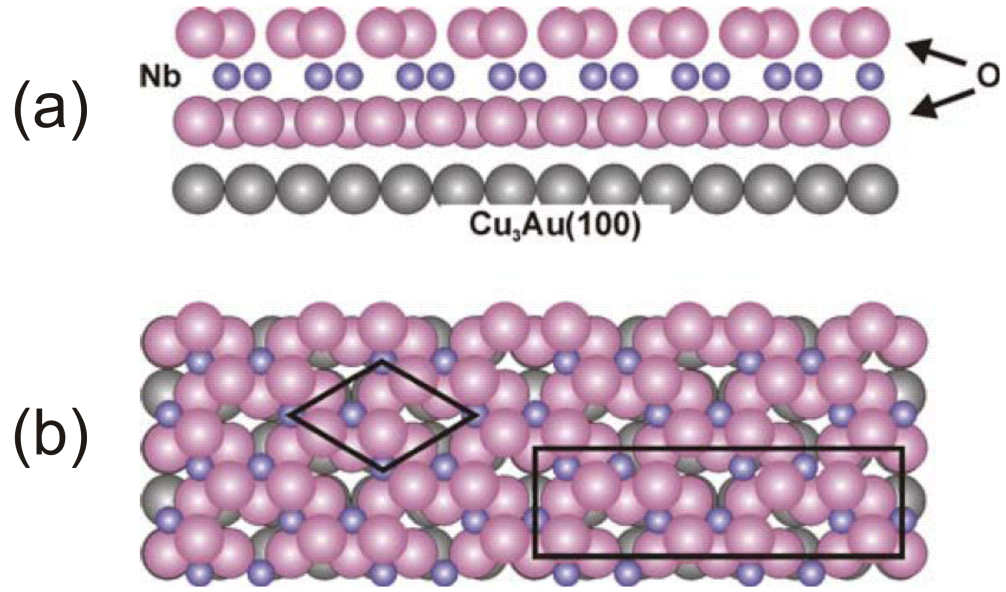

Figure 3.8: Structural model of monolayer $Nb_2O_5/Cu_3Au(100)$ films; (a) side view, (b) top view. The (1×1) unit cell and the (2×7) superstructure are indicated in (b).

However, preliminary theoretical results from Sierka *et al.* show that the structure in Figure 3.8 may not be the overall most stable structure [130], and hence, further studies are required.

3.2 Niobia Multilayer Films

It is obvious that the thickness of the thin oxide films may strongly affect the properties of metal deposited on these films, as recently shown for MgO [131]. In particular, metal deposits atop an ultrathin film can migrate toward the metallic substrate below the film. Although this effect may have a fundamental interest, industrial catalysts deal with bulk oxide materials. It is therefore proximate to grow films of sufficient thickness, such that this interaction is not prone to occur. In the light of this issue, multilayer niobia films were also prepared. First results are presented here; however, this topic remains the aim of ongoing research.

3.2.1 Preparation

Multilayer films can be prepared either by additional deposition and oxidation cycles beyond the monolayer coverage (1.6 Å) or by extending the time of the single-step preparation applied for the monolayer films. In both cases, the preparation was concluded by a second oxidation at 900 K for 5 min at 10^{-6} mbar O_2.

3.2.2 Results and Discussion

With increasing niobia coverage, the LEED pattern changes from hexagonal to rectangular symmetry, with various intermediate structures (Figure 3.9). This is interesting, because the substrate has square symmetry, and hence, a rectangular symmetry for the monolayer would be more intuitive. In general, the patterns are complex, but still exhibit two co-existing rotational domains, as found for the monolayer films (Figure 3.9 (a)). As the thickness increases, the influence of the substrate on the surface layers of the film is diminishing, and a different geometry is adopted. It seems that the hexagonal structure of the monolayer films is somehow stabilized by the presence of the metallic substrate.

As discussed in Section 3.1.2, PES data for the well-ordered monolayer films show a binding energy in the Nb $3d_{5/2}$ range of 206.4 eV, which is slightly lower than what was observed for Nb_2O_5, due to the well-known screening effect of the metal substrate below the film. According to the proposed structure of the monolayer films, it contains the top O atoms in bridging Nb-O-Nb positions. As a result, HREEL spectra show only the peak at 703 cm^{-1}; i.e., typical for stretching and/or bending vibrations of the Nb-O-Nb linkage. For thicker niobia films, the PES measurements (provided by D.E. Starr) reveal a peak at 207.4 eV for the Nb $3d_{5/2}$ level (Figure 3.10 (a)), clearly showing that the multilayer niobia films consist of Nb cations in the highest oxidation state, (+5). Concomitantly, the small shoulder at 206.4 eV, observed at normal electron emission and not in grazing emission, can be assigned to Nb ions at the interface between niobia and the substrate.

In contrast to the monolayer films, the multilayer films show HREELS peaks at 565 cm^{-1}, 842 cm^{-1} and 984 cm^{-1} (Figure 3.10 (b)). As discussed in Section 3.1.2, Xie *et al.* report HREELS data on different niobia films ("NbO_x" and "Nb_2O_5" in their notation) grown on Pt(111), which turned out to be of poor crystallinity [112,113]. These films showed HREELS signals at 384 cm^{-1} and 926 cm^{-1}. Note that the resolution of 96 cm^{-1} within this work is superior to the 50 cm^{-1} of Xie *et al.* by a factor of ~ 2.

The high wavenumber signal was attributed to the Nb=O stretching

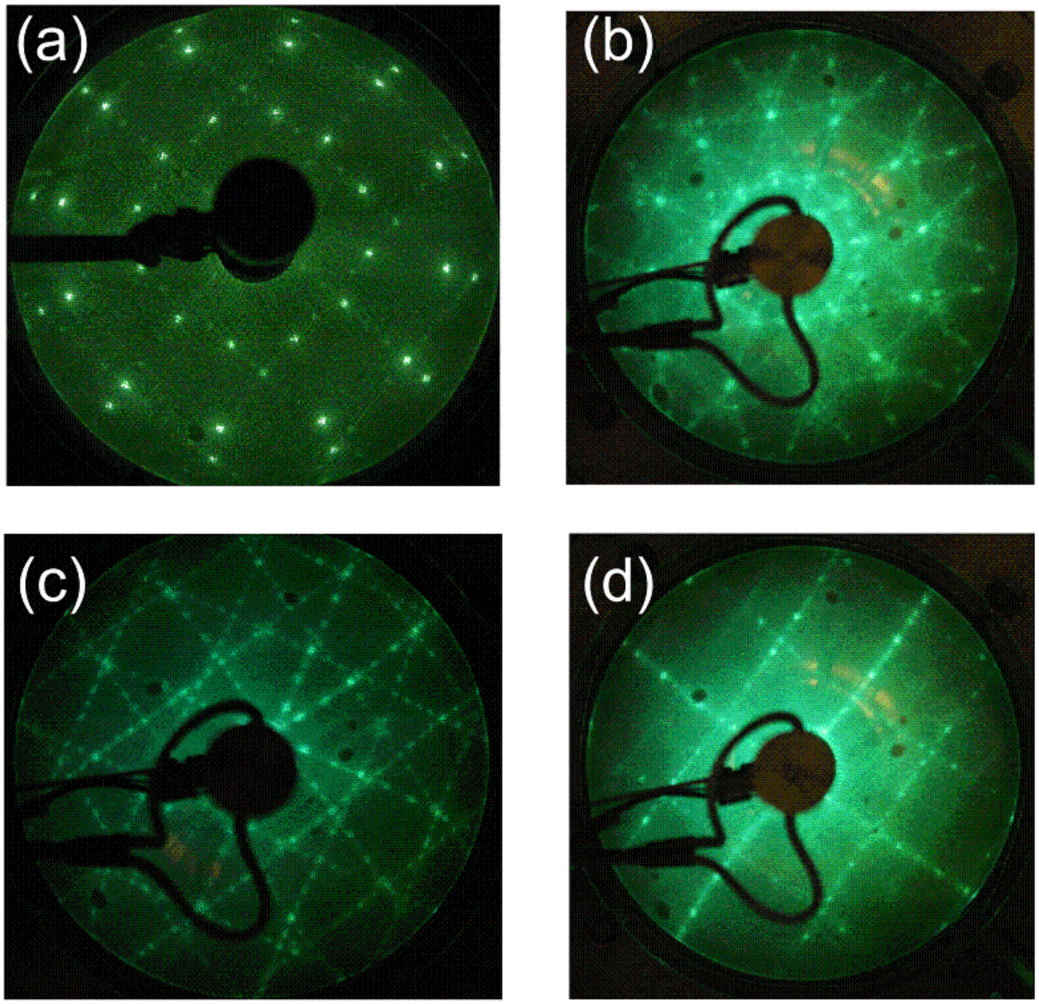

Figure 3.9: LEED patterns (70 eV) of niobia films with increasing coverage. (a) 1 ML; (b) slightly above 1 ML; (c) 1-2 ML; (d) $\sim$ 2 ML.

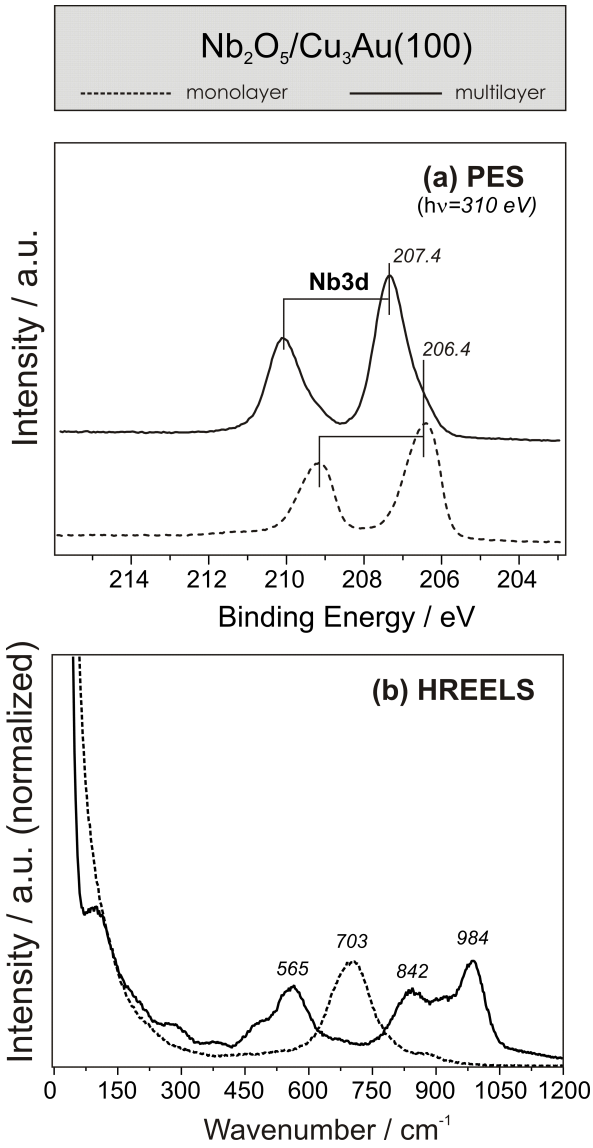

Figure 3.10: Niobia multilayer films grown on $Cu_3Au(100)$. (a) PES (at 0° with respect to surface normal) (data provided by D.E. Starr, spectra are offset for clarity); (b) HREELS (spectra are normalized with respect to the elastic peak).

mode, although it is significantly lower than any observed on so-called *H*-phase of Nb_2O_5, but much higher than that of other stable crystalline (so-called *T*- and *TT*-phase) or amorphous phases of niobium pentoxide (700 cm^{-1} - 870 cm^{-1}) observed by Raman and IR spectroscopy [132–134]. The NbO_2 phase showed transverse optical phonons below 700 cm^{-1} [135], which would correspond to surface phonons at 807 cm^{-1}, as calculated in reference [112].

It is well-established that M=O terminated surfaces can be reduced by bombardment with accelerated electrons. Following Abu al-Haija *et al.*, the LEED electron beam was used for a surface reduction [136, 137]. Using electron bombardment, the authors specifically altered the surface termination. Vibrational spectroscopy showed the removal of the vanadyl groups, while all other phonons were maintained. Additional PES results show that, although the vanadyl O atom is removed, the V atom persists in a reduced oxidation state, while re-oxidation of the film restores the vanadyl groups [137]. HREEL spectra for the as-prepared, reduced and re-oxidized film are given in Figure 3.11.

Bombardment of the sample with LEED electrons (200 eV) does not result in a selective removal of the niobyl groups. Instead, an overall intensity reduction is observed by comparison of spectra (i) and (ii) in Figure 3.11. Re-oxidation at relatively high temperature (900 K, 10^{-6} mbar O_2, 5 min) restores the original intensity, with the exception of the altered ratio of the peaks at 842 cm^{-1} and 984 cm^{-1}, respectively. Annealing the sample at 900 K for 5 min in UHV suppresses the band at 984 cm^{-1} significantly, while the intensity gain at 842 cm^{-1} is very strong. Another re-oxidation under the conditions of the previous one restores the original situation (compare (i) and (v)).

Apparently, a good way to remove the niobyl groups is to anneal the sample in UHV for 5 min at 900 K. Spectrum (ii) of Figure 3.11 suggests an overall loss of structural order in the film after the bombardment, which could not be entirely reversed by the first re-oxidation. The fact that the second re-oxidation was seemingly more successful can be assigned to the fact that the annealing in UHV may have contributed to restoring the order.

3.2.3 Conclusions

LEED results indicate that the structure of the multilayer is quite different from the structure of the monolayer. With increasing niobia coverage, the pattern changes from hexagonal to rectangular symmetry. This is most likely due to a diminishing influence of the substrate on the surface layer of the film, which will then adopt a different geometry. It is interesting, however,

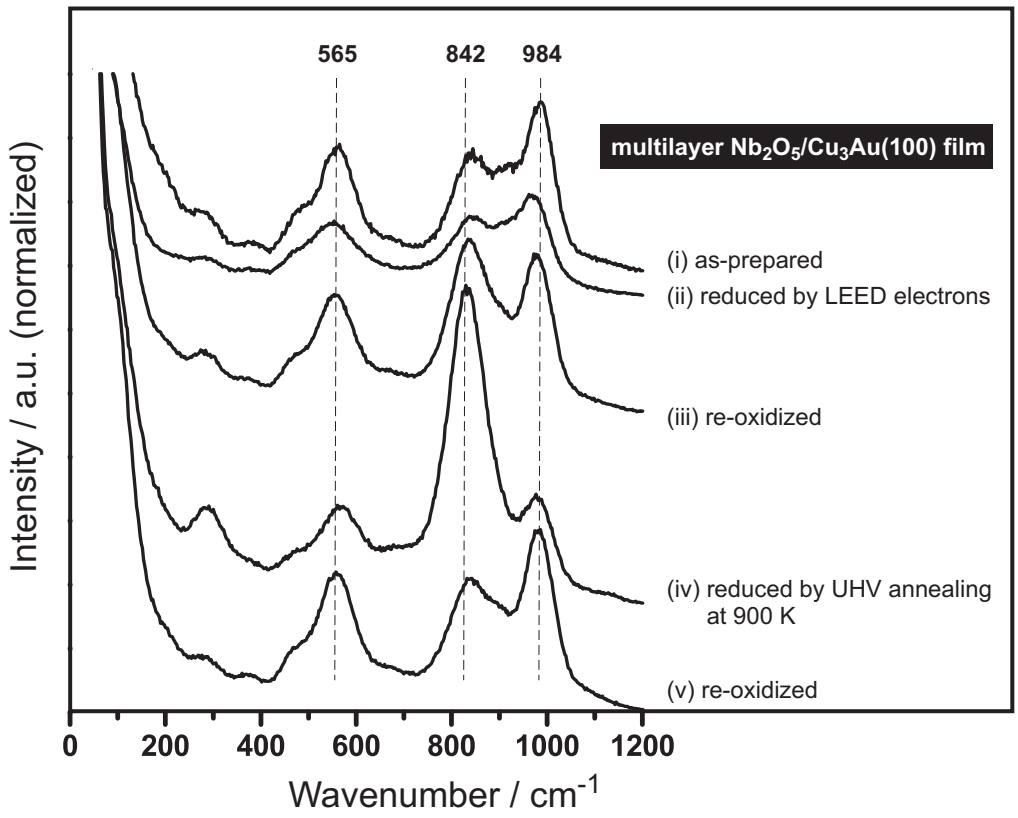

Figure 3.11: HREELS of multilayer Nb_2O_5 films. Reduction for (ii) was done by LEED at 200 eV for 2 min. Reduction for (iv) was done by annealing in UHV for 5 min at 900 K. Oxidation in (iii) and (v) was done at 10^{-6} mbar O_2 for 5 min at 900 K. The spectra are offset for clarity.

that the symmetry of the monolayer is hexagonal on a square substrate, while the multilayer grows in a rectangular structure.

Contrary to the monolayer films, the multilayer niobia films exhibit niobyl groups that can be removed and restored similarly to the vanadyl groups on V_2O_3/Au(111), as reported by Abu al-Haija *et al.* However, bombardment with LEED electrons of $E_{kin} = 200$ eV was far less successful than annealing the sample to 900 K for 5 min in UHV.

3.3 Cobalt Supported on Monolayer Niobia Films

Continuing the attempts of modeling a niobia-based Fischer-Tropsch catalyst, cobalt was deposited on niobia monolayer films. The preparation of Co/Nb_2O_5 particularly aims at studying the specific interaction between Co and niobia.

3.3.1 Preparation

Monolayer Nb_2O_5 films, which has been discussed in Section 3.1, are used here as a substrate for metal particles. Cobalt was evaporated in UHV at 100 K and at 300 K from a rod (2 mm diameter), which was calibrated using a quartz microbalance in terms of nominal Co thickness.

3.3.2 Results and Discussion

The model system of cobalt deposited on the monolayer $Nb_2O_5/Cu_3Au(100)$ film has been studied by means of STM, CO adsorption (IRAS and TPD), and PES.

STM

Figure 3.12 shows STM images of Co deposited at 300 K on the monolayer niobia films (provided by D.E. Starr). Co coverages were 0.5 Å and 2 Å, as indicated. Apparently, small particles are homogeneously dispersed on the surface, which coalesce at higher coverage. However, the apparent height of the majority of these particles does not exceed 2 Å. It is concluded that Co wets the surface of the niobium oxide film, forming two-dimensional (i.e., monolayer) islands. Since the formation of these islands can be kinetically limited, samples with both coverages were heated to 500 K and re-investigated. At low coverage, large and well-shaped islands formed, while the high coverage

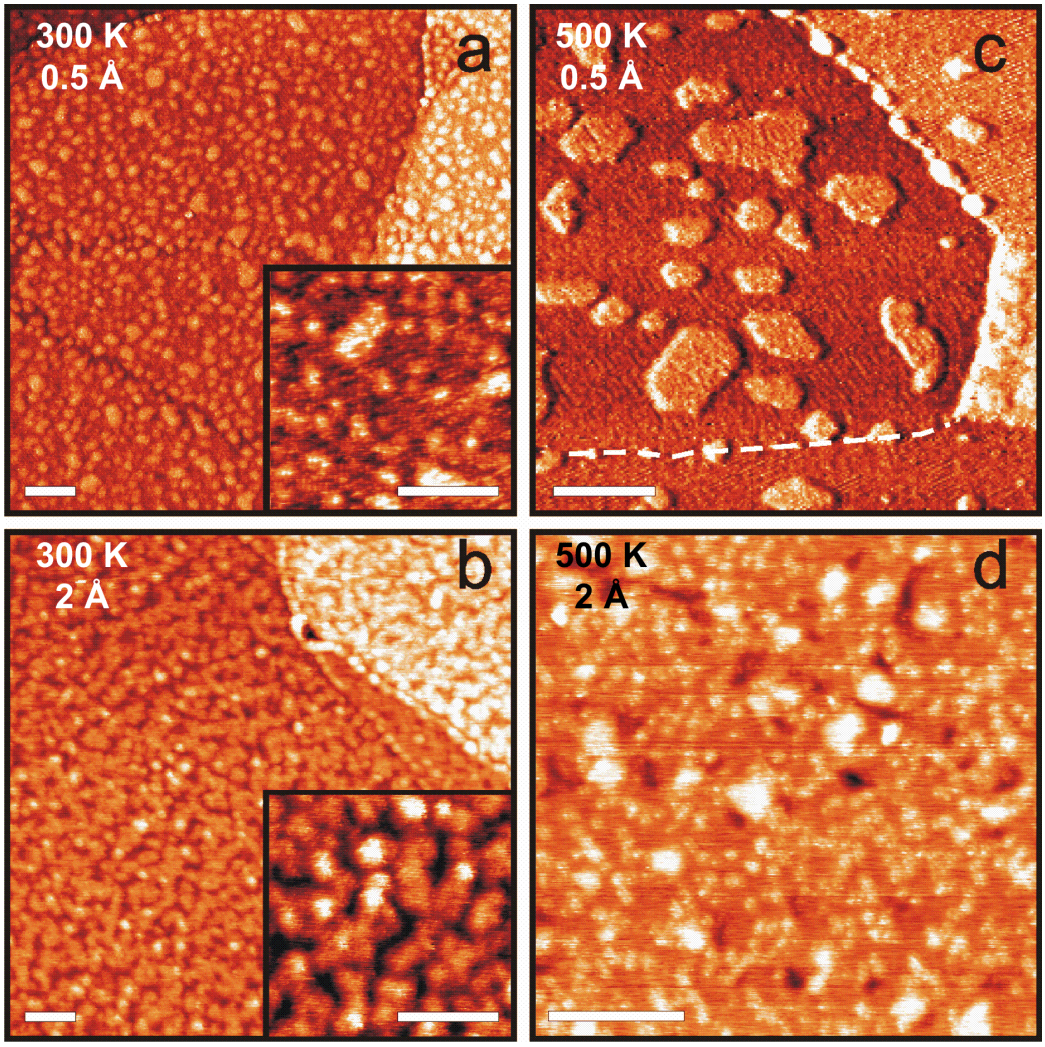

Figure 3.12: STM images of Co deposited on monolayer Nb_2O_5 films at 300 K (provided by D.E. Starr). Co coverages are indicated. Images (c) and (d) were taken after heating the sample to 500 K. The scale bar corresponds to 20 nm. Tunneling parameters: (a) $V = 1.2$ V, $I = 1$ nA; (b) $V = 0.75$ V, $I = 0.7$ nA; (c) $V = 1.25$ V, $I = 1.3$ nA; (d) $V = 0.75$ V, $I = 1$ nA. Image (c) is presented in differentiated contrast, where the domain boundary is marked by the dashed line.

sample exhibited an ill-defined and relatively rough surface with a corrugation amplitude of $\sim$ 1 Å. On thin alumina films, three-dimensional Co particles were found, the apparent height of which was up to 2 nm [138].

CO Adsorption

Figure 3.13 (a) shows CO TPD spectra measured for $\sim$ 1 Å Co deposited on the monolayer niobia film at 100 K. The first run (black line) showed a number of desorption features (150 K, 275 K, 340 K, 400 K). The peaks in the 250 K - 450 K temperature range have been assigned previously to CO desorption from metallic Co particles on thin alumina films. The respective spectrum is presented in the same figure for comparison. The peak at 387 K has been assigned to CO atop species, while the shoulder at 275 K is assumed to originate from $Co(CO)_n$ [139]. However, the second run of the CO TPD (red line) is very different from the first, but very similar to the CO TPD spectrum acquired from the pristine niobia film (see Figure 3.7). In fact, the only difference is a rather small shoulder at $\sim$ 180 K, which is not found on the clean film. A different behavior is found for Co on thin alumina films (blue line), where the CO TPD spectra undergo only minor changes with each run [139]. It is clear that significant structural changes must occur while heating the sample to 500 K during the TPD. Additional depositon of Co after a TPD run could restore the signals assigned to CO desorption from sites of metallic Co, and heating to 500 K would remove it again.

Interestingly, no feature associated with CO desorption from metallic Co was observed, when cobalt was deposited at 300 K (Figure 3.13 (b)). Quite on the contrary, the spectrum is very similar to the one for pristine niobia, even for the first run (black line), except for the additional peak at $\sim$ 200 K. The CO TPD spectra for the second run (red line) for Co deposition at 100 K and the first run for Co deposition at 300 K are practically identical. It is concluded that Co interacts strongly with the niobia substrate at 300 K, leading to a loss of metallic properties of Co.

Since CO desorption and structural changes upon heating take place simultaneously, the TPD spectra may be affected by this. In order to follow CO adsorption as a function of temperature, IR spectra of 10 L of CO were acquired at 100 K after heating to the temperatures given in Figure 3.13 (c). When Co was deposited at 100 K, one band at 2082 cm^{-1} is observed, which is similar to data assigned to $Co(CO)_n$ on Co/alumina [139]. Upon heating to 300 K, the feature splits into three peaks at 2050 cm^{-1}, 2078 cm^{-1} and 2098 cm^{-1}, which attenuate with increasing temperature. The second band observed at 100 K (2127 cm^{-1}), shifts to 2135 cm^{-1} and becomes more promi-

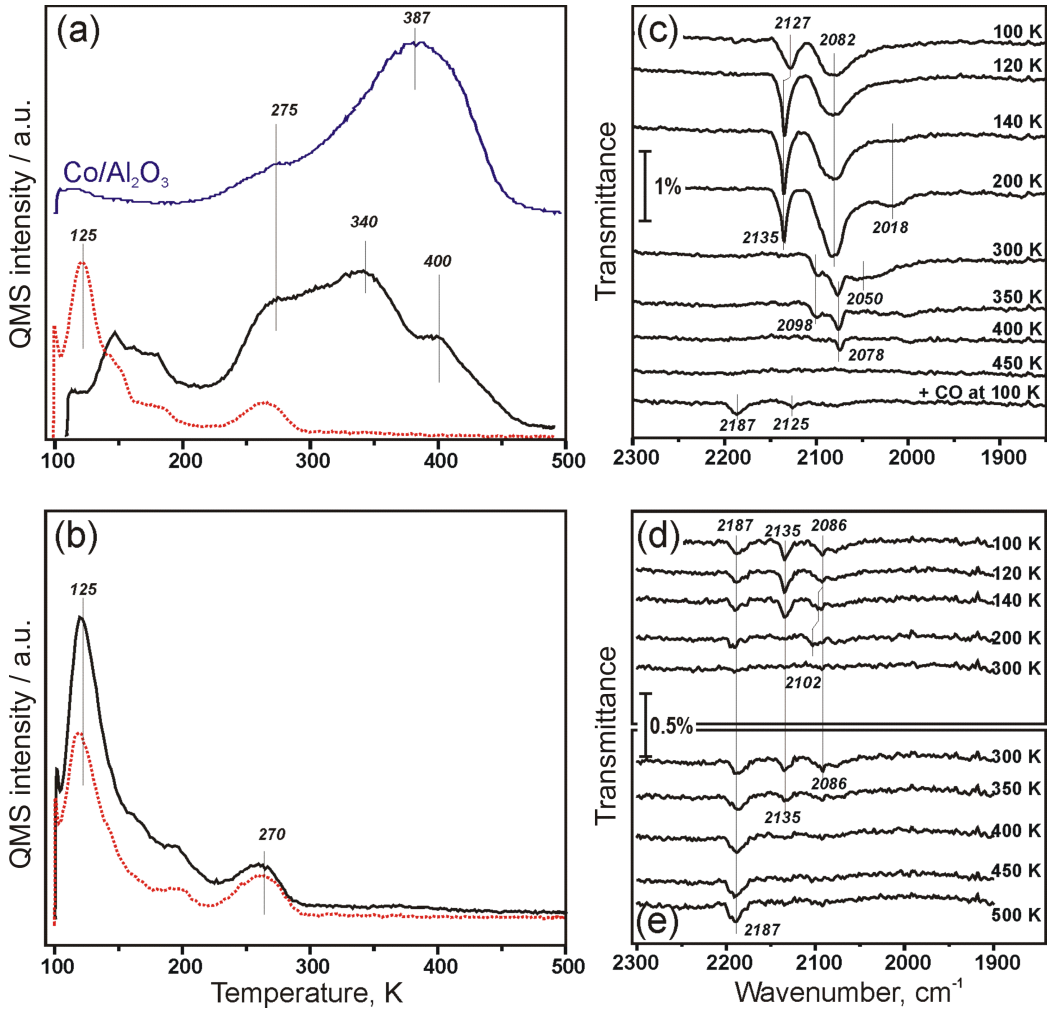

Figure 3.13: (a) CO TPD from cobalt deposited on monolayer Nb_2O_5 films at 100 K (black line: first run; dotted red line: second run; purple line: CO TPD from cobalt on alumina film for comparison); (b) CO TPD from cobalt deposited on monolayer niobia film at 300 K (black line: first run; dotted red line: second run); (c) CO IRAS of cobalt deposited on monolayer niobia film at 100 K, followed by flashing to indicated temperatures and final CO re-adsorption; (d) CO IRAS of cobalt deposited on monolayer niobia film at 300 K, followed by flashing to indicated temperatures; (e) re-adsorption of CO, flashing series continued to indicated temperatures. IR spectra are offset for clarity.

nent above 140 K, but vanished above 300 K. This behavior is consistent with CO adsorbed on the defects of the niobia film. The co-existence of defects and Co demonstrates that defects are not the preferential nucleation sites of Co on $Nb_2O_5/Cu_3Au(100)$. Re-adsorption of CO at 100 K after flashing the sample to 500 K showed in principle only one band at 2187 cm^{-1} (the weak signal at 2125 cm^{-1} is again consistent with the defects of niobia), which is no surprise after the strong structural changes suggested by the TPD spectra.

As shown in Figure 3.13 (d), this band is present from the beginning for Co deposition at 300 K (and CO adsorption at 100 K), while the two other signals at 2135 and 2086 cm^{-1} are similar to those found for Co deposited at 100 K, although much weaker here. After flashing the sample to 300 K, CO is no longer detected by IRAS, which agrees with the complete desorption of CO below 300 K as observed in TPD (see Figure 3.13 (b)). The spectra in Figure 3.13 (e) are taken after additional flashes to the indicated temperatures, followed by re-adsorption on CO at 100 K. The band at 2187 cm^{-1} is the only one that persists up to 500 K and is practically identical with the band of CO adsorbed on Nb^{5+} sites [140] (see Section 3.1.2). The loss of all cobalt-related features at elevated temperatures indicates that niobia encapsulates the Co deposits such that the resulting surface no longer exhibits metallic adsorption properties.

PES

The electronic structure of the cobalt species on the niobium oxide surface was studied by means of synchrotron PES. Figure 3.14 presents the spectra before and after deposition of Co (contributed by D.E. Starr). The clean film is characterized by a binding energy of 206.4 eV for the Nb $3d_{5/2}$ level, which is discussed in Section 3.1.2. For Co deposited at 300 K, the PE spectra show two species in the Co $2p_{3/2}$ range at 778 eV and 781 eV. These values are typical for metallic (Co^0) and oxidized ($Co^{\delta+}$, such as in Co_3O_4 or CoO) states, respectively [141]. The integral ratio of $[Co^{\delta+}]$:$[Co^0]$ increases from 0.1 to 0.3, when the detection angle is changed to grazing incidence. This implies that $Co^{\delta+}$ is located primarily on the surface, while Co^0 is found mostly in the sub-surface region. In principle, this could be explained by the formation of Co particles with oxidized $Co^{\delta+}$ species on the surface modified by Nb^{5+}, as revealed by the IRAS experiments presented in Section 3.3.2. However, the STM images in Figure 3.12 do not show three-dimensional particles, but monolayer islands typical for metal-on-metal systems. Therefore, it seems likely that Co migrates through the film and forms a metallic layer in direct contact with Cu_3Au. In this model, oxidized $Co^{\delta+}$ is formed on or incorporated into the niobia film, resulting in a partial reduction of the niobium

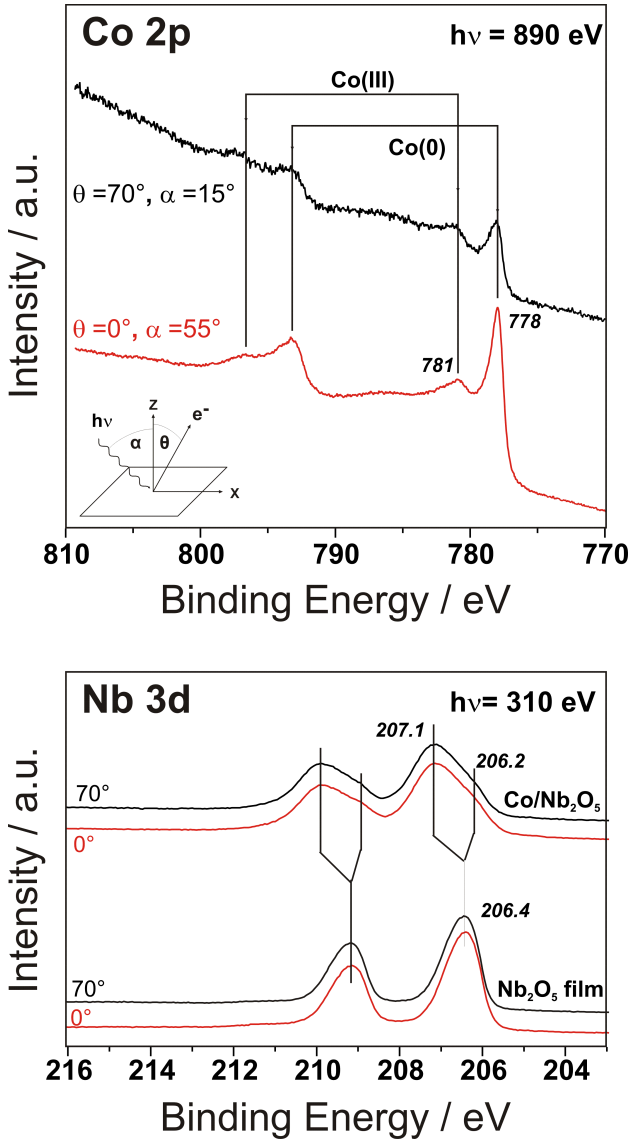

Figure 3.14: PES of cobalt on monolayer niobia films (provided by D.E. Starr).

cations. The latter is demonstrated by the altered Nb $3d_{5/2}$ region, where the original feature at 206.4 eV is replaced by two new ones at 207.1 eV and 206.2 eV. The intensity ratio of these signals is independent of the detection angle, indicating all Nb species lying in one single layer, as previously found for the pristine film (see Section 3.1.3). It must be stated that the binding energy of 207.1 eV exceeds the one of 206.4 eV, which represents already fully oxidized Nb^{5+}.

A tentative explanation is based on the presence of cobalt ions and reduced niobium ions, by which the Fermi level could be pinned down at a different position. The PES results clearly show that Co deposited on the niobia film is readily oxidized at 300 K, which is at variance to Co deposited on alumina films [138, 139].

3.3.3 Conclusions

The combined TPD, IRAS and PES results show that the niobia film is able to readily oxidize metallic Co^0 deposits even at room temperature. The Co^0 can be stabilized only by deposition at low temperatures, due to kinetic limitations. The Co/niobia interaction leads to the formation of a mixed Co-Nb oxide, the surface of which may expose Nb^{5+}, as concluded from CO adsorption experiments. In addition, Co species may migrate through the film, which seems to occur more efficiently at elevated temperatures. These results are largely at variance with Co deposited on thin alumina films, where three-dimensional and metallic particles are formed at 300 K, which remain stable up to 600 K [138, 139]. These results could shed some light on the promoting effect of niobia, as observed on industrial niobia-supported Co catalysts, the exceptional catalytic properties of which are rationalized on the basis of the SMSI effect [14, 15].

Chapter 4

Supported Niobia Particles

The next step in the studies of niobia-based catalysts are alumina-supported niobia particles. Apart from being a useful support in the Fischer-Tropsch process [14–17], niobia can also play the role of the active compound, when it is added to another oxide, such as alumina or silica, where it forms a monolayer-type catalyst that is dispersed over the support [26, 46, 142–144]. As mentioned in Chapter 1, the activity of supported niobia is often enhanced with respect to the corresponding bulk component. The groups of Schmal [14, 15,28–31,31–35] and Guczi [36–38] investigated catalyst systems promoted by niobia. Another example for the usefulness of supported niobia is the work of Li *et al.*, who contributed several papers on the capability of niobia/alumina of hydrating ethylene oxide to ethylene glycol [145–148].

The atomic structure of supported niobia continues to be debated [63,149, 150] (and references therein), and therefore an investigation using the surface science approach may provide deeper insight. Moreover, vanadium and niobium are homologues in Group 5 of the Periodic Table of Elements, which is why a comparison of alumina-supported vanadia and niobia is very illustrating for the understanding of reaction mechanisms. A study of alumina-supported vanadia is provided by Magg *et al.* [149, 151, 152].

The alumina-supported niobia model catalyst is studied by means of IRAS and STM, in order to reveal structural properties. Thermal stability is investigated as well. The results presented in this Chapter represent the first surface science study of a niobia/alumina model catalyst.

4.1 Preparation

Alumina films prepared in this work were obtained by surface oxidation of a NiAl(110) single crystal, following a procedure that is well-known from the

literature [153]. The oxidation was done in front of a calibrated gas doser (550 K, 20 min, 10^{-6} mbar O_2), followed by annealing (1140 K, 5 min, UHV). This cycle was then repeated once, in order to avoid holes in the film.

The quality of the film was controlled by LEED. The alumina film has a rather complex LEED pattern [153]. The same reference also summarizes the characterization of the film, which grows in multiple domains. More precisely, it exhibits two reflection domains and two antiphase domains, which are all oriented in characteristic angles with respect to each other and to the underlying NiAl. STM images shown in Figures 4.1 (a) and 4.3 (d) reveal the domain boundaries as line defects particularly well.

Niobium and (for reference measurements) vanadium were evaporated onto the alumina film from a metallic rods (2 mm diameter, from Goodfellow, 99.99%) using a commercially available Focus EFM 3 evaporator. During evaporation, the chamber was backfilled with 10^{-7} mbar O_2. All amounts of niobia and vanadia in the following are given in terms of nominal thickness of the respective metal.

4.2 Results and Discussion

4.2.1 STM

STM images of a series of niobia/alumina samples with increasing coverage are presented in Figure 4.1. At 0.1 Å (Figure 4.1 (a)), there are particles, which are perceived as niobia, dispersed randomly over the surface; i.e., both on and between the line defects.

As previously shown for metallic deposits on alumina, the spatial distribution of the particles basically reflects the extent of interaction between the deposits and their support [153, 154]. The absence of preferential nucleation on defects, as deduced from Figure 4.1, can be interpreted as a rather strong interaction between the niobia particles and the alumina support.

Particle density is a (monotonically increasing) function of coverage up to 1 Å, where it saturates at $\sim 2\times10^{13}$ cm^{-2}, while the average particle height is nearly constant from the onset (see Figure 4.1 (f)). At high coverages the particle size is difficult to determine precisely, due to the tip deconvolution effect (see Section 2.5). However, it is obvious that the growth mode of niobia on alumina under the chosen conditions is three-dimensional from the onset (i.e., a Volmer-Weber growth mode).

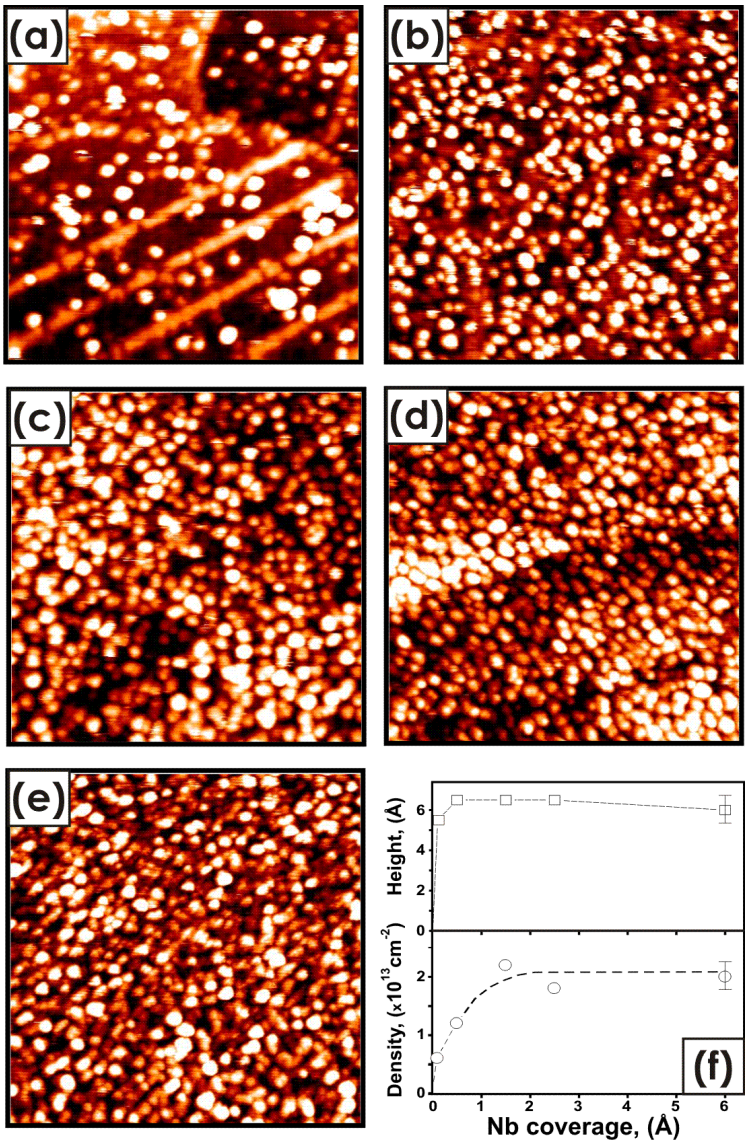

Figure 4.1: (a) - (e) STM images of niobia/alumina as function of niobia coverage ((a) 0.1 Å, (b) 0.5 Å, (c) 1.5 Å, (d) 2.5 Å, (e) 6.0 Å). Image size and tunneling parameters: 60×60 nm^2, $V = 3$ V, $I = 0.1$ nA. (f) Average apparent particle height and particle density as functions of niobia coverage, as seen in (a) - (e).

4.2.2 IRAS

IRAS was used to study the surface structure of the niobia/alumina model catalyst. Both phonons and vibrations of adsorbed molecules were measured, where the latter are represented by CO as the typical probe molecule (see Section 2.6.3). The phonon region is shown in Figure 4.2 (a). The prominent 865 cm^{-1} band of pristine alumina [155] could be reproduced. It attenuates upon niobia deposition, while a new band at 900 cm^{-1} appears as a shoulder, eventually resulting in a broad feature centered at $\sim$ 885 cm^{-1} for the highest niobia coverage studied. The spectral broadening is consistent with the formation of small and randomly dispersed particles, as observed with STM. A second new band at 986 cm^{-1} emerges at a coverage of 1 Å.

The assignment of these bands is facilitated by comparison with the results on an alumina-supported vanadia system, which was studied in detail by Magg *et al.* [149, 151, 152]. For convenience, the bottom curve in Figure 4.2 (a) shows the IR spectrum of 3.5 Å vanadia/alumina similarly prepared in the same setup. Based on results from Raman and IR spectroscopy, the peak at 1045 cm^{-1} was assigned to the stretching mode of vanadyl (V=O) groups. Meanwhile, the broad signal at $\sim$ 950 cm^{-1} is associated with vibrations involving V-O-Al linkage at the vanadia/alumina interface, as predicted by theoretical calculations [149, 151]. On niobia/alumina, the peak at 986 cm^{-1} must be therefore assigned to the niobyl (Nb=O) stretch and the peak at 885 cm^{-1} to Nb-O-Al interface vibrations. Simple mass considerations show indeed that replacing V by the heavier Nb would result in a shift to lower wavenumbers. The fact that each band in the niobia/alumina spectra has a straightforwardly identified match in shape and intensity in the vanadia/alumina spectra is a further strengthening of this assignment.

CO was used to probe the surface of niobia/alumina. The IR spectra as a function of niobia coverage are presented in Figure 4.2 (b). The associated wavenumber of 2190 cm^{-1} for the CO stretch represents a strong blueshift with respect to the gas phase wavenumber (2143 cm^{-1}). Such a shift must be explained by a strengthening of the C/O bond, which is caused by a weakened C/surface bond. This occurs on metal cations that lack *d* electrons for back donation and that must therefore be highly, if not fully oxidized. Hence, it is concluded that this band represents CO (linearly) adsorbed on accessible Nb^{5+} sites, in agreement with Beutel *et al.* [140].

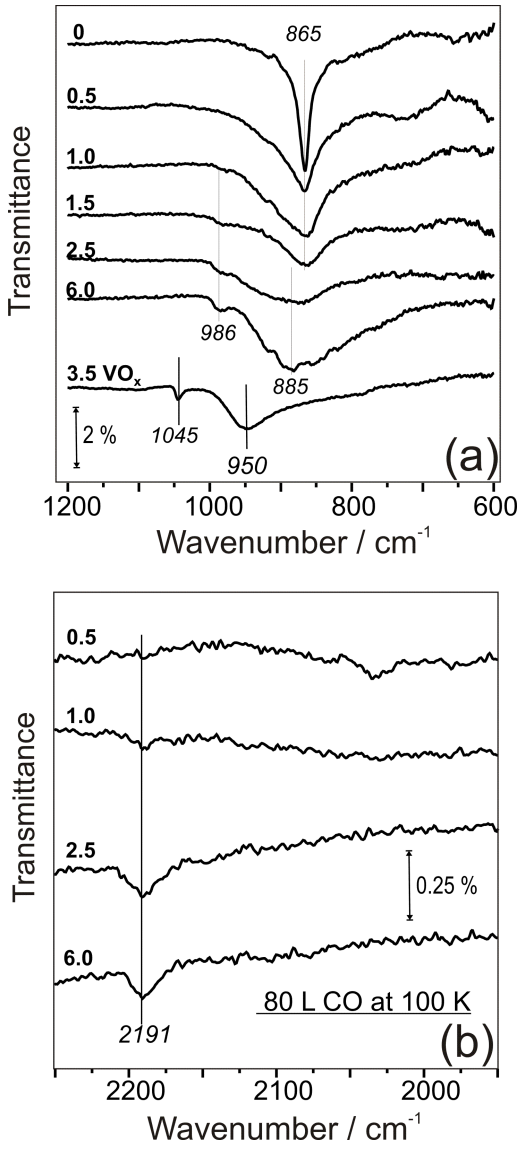

Figure 4.2: IRAS of niobia/alumina. (a) dependence of the phonons on the niobia coverage, (b) dependence of CO adsorption on the niobia coverage. The coverage in Å is indicated. The spectra are offset for clarity. For comparison, the phonon spectrum of identically prepared VO_x particles is shown in the bottom line of (a).

4.2.3 Thermal Stability

Thermal stabilty of alumina-supported niobia was studied with STM and IRAS. Figure 4.3 shows STM images of the 0.5 Å niobia/alumina sample (a) in the as-prepared state, and after flashing the sample in UHV to (b) 500 K, (c) 700 K and (d) 900 K. While Figure 4.3 (a) and (b) are essentially identical in terms of particle density and particle size, the flash to 700 K seems to have increased the size of some particles at the expense of the overall particle density. Hence, some particles started sintering, and niobia migration into the alumina film seems to have occured as well. After the flash to 900 K, the effect is even more visible. As shown for metal particles [154], this interdiffusion proceeds probably via the alumina line defects, thus resulting in their decoration with niobia particles, as seen in Figure 4.3.

The 2.5 Å niobia/alumina sample underwent a different treatment. It was first heated to 700 K in UHV, then oxidized in 10^{-7} mbar O_2 at 400 K and finally at 900 K. STM images are shown in Figure 4.4 (a)-(d), and IRAS data in Figure 4.5.

The initially existing Nb=O band at 986 cm^{-1} obviously disappears upon flashing to 700 K. Concomitantly, the broad band centered at 905 cm^{-1} and assigned to Nb-O-Al interface vibrations sharpens, most probably due to a strong attenuation of the main alumina phonon at 865 cm^{-1}. This can be explained by the onset of niobia migration into the film, as revealed by STM and discussed above. Mild oxidation at 400 K restores the niobyl species without affecting the interface region. However, further oxidation at 900 K shifts the interface phonon from 915 to 948 cm^{-1}, overlapping with the niobyl band, such that the latter becomes a shoulder. This observation is understood as an indication for structural modifications of the particle/substrate interface, because STM results show that the overall particle morphology is not much affected by the oxidation at 900 K. The latter finding also indirectly supports the assignment of the $\sim$ 900 cm^{-1} band to a niobia/alumina interface phonon.

The effect of the O_2 ambient on the thermal stability can be rationalized in terms of oxygen preventing the reduction of the niobia surface, and hence, migration of Nb atoms into the film. Moreover, previous studies of the interaction of O_2 with alumina-supported particles demonstrated that metal particles may promote thickening of the alumina film via dissociation of molecular oxygen and subsequent diffusion of O atoms to the alumina/NiAl interface [156, 157]. This may in turn alter the interaction of the niobia particles and their alumina support as well.

The comparison of the phonon data of niobia films grown on a $Cu_3Au(100)$ substrate and alumina-supported niobia particles is very helpful. Vibrational

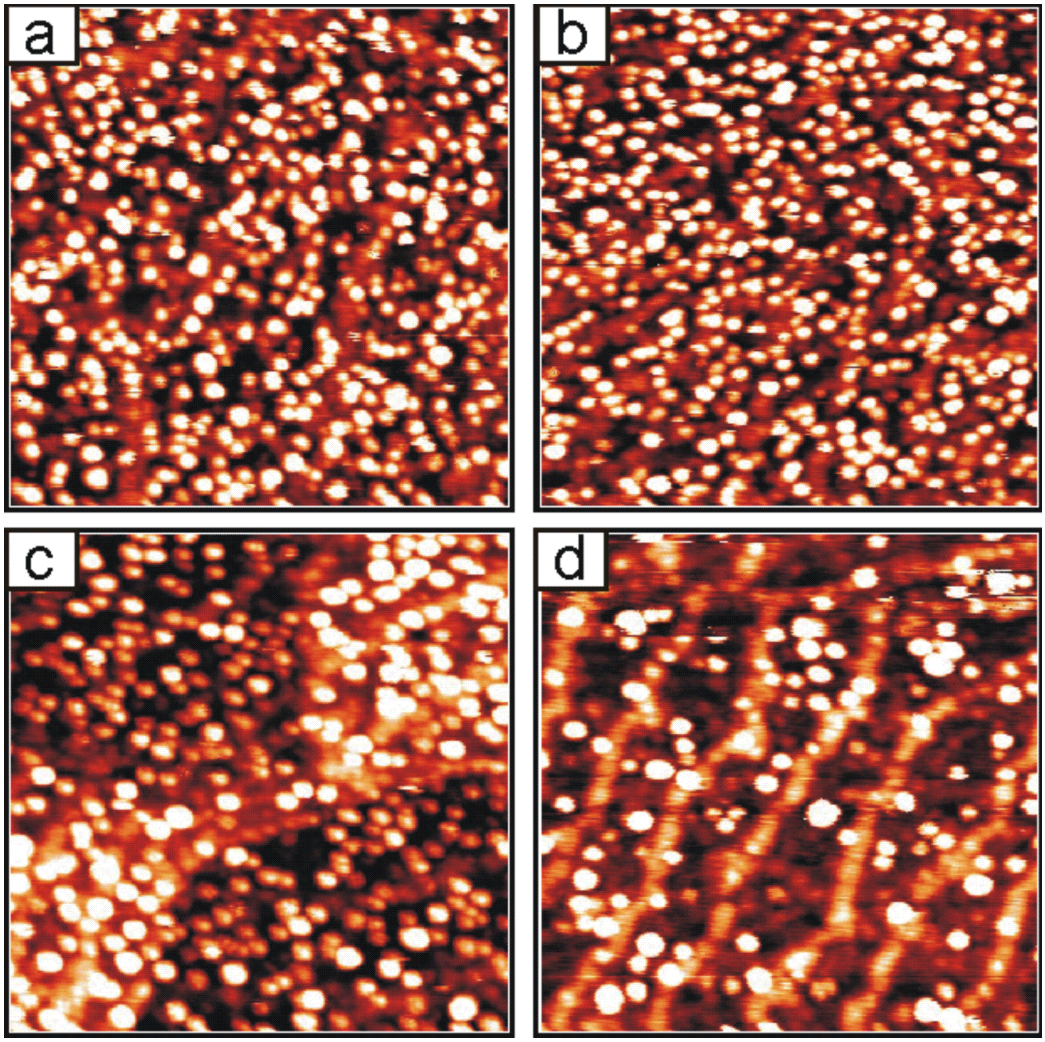

Figure 4.3: STM images showing the thermal stability of niobia/alumina. (a) as-prepared; flash in UHV to (b) 500 K, (c) 700 K, (d) 900 K. Image size and tunneling parameters: 60×60 nm^2, 0.1 nA, 3 V.

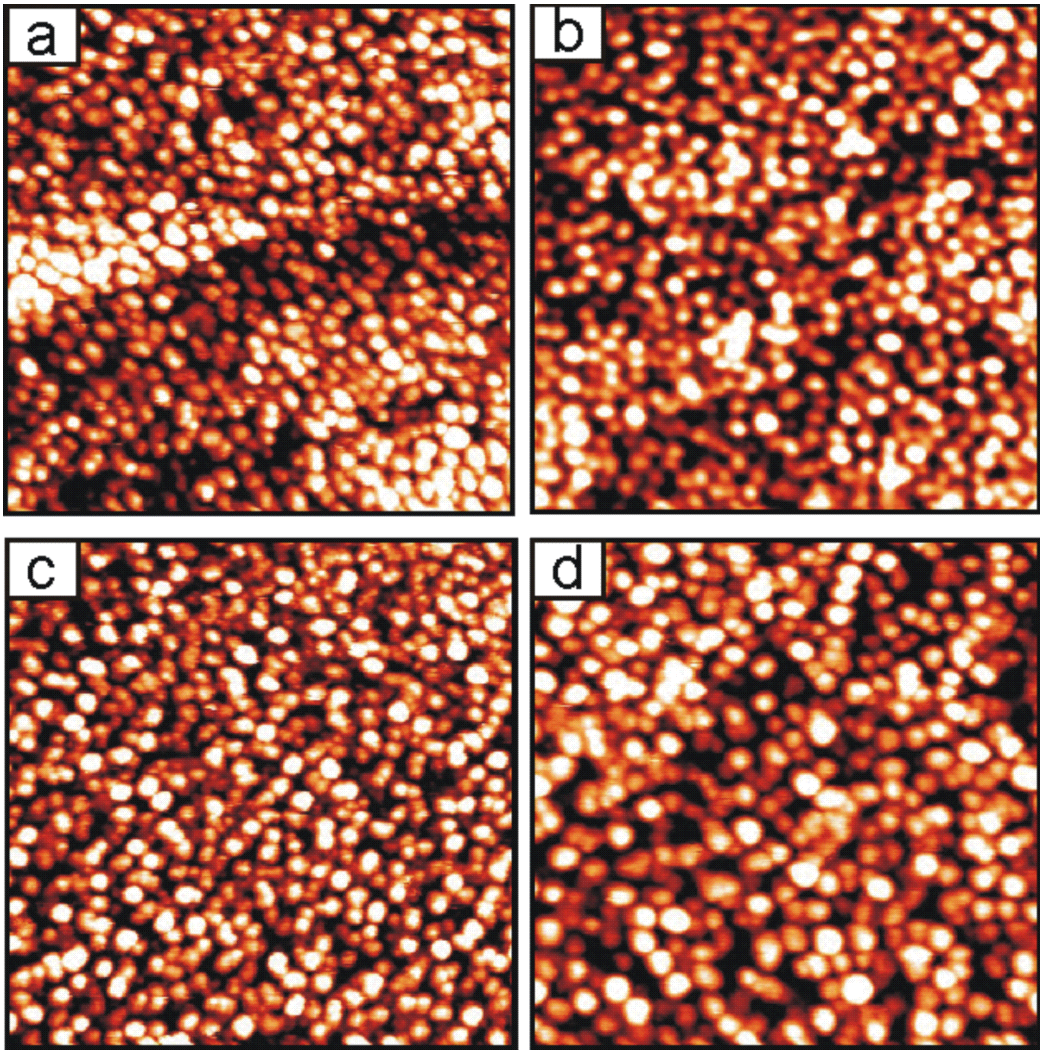

Figure 4.4: STM images following the removal and restoration of niobyl groups. (a) as-prepared; flash to (b) 700 K in UHV, (c) 400 K in 10^{-7} mbar O_2, (d) 900 K in 10^{-7} mbar O_2. Image size and tunneling parameters: 60×60 nm^2, $V = 3$ V, $I = 0.1$ nA.

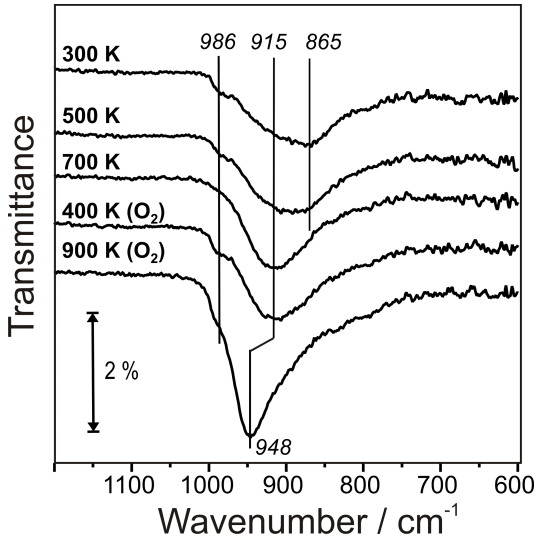

Figure 4.5: IRAS data of the removal and restoration of niobyl groups. Top to bottom: as-prepared at 300 K; flash to 500 K and 700 K, respectively, in UHV; flash to 400 K in 10^{-7} mbar O_2; flash to 900 K in 10^{-7} mbar O_2. The spectra are offset for clarity.

spectroscopy proves significant differences between the monolayer and the multilayer film. While the former has only one dominant feature located at 703 cm^{-1} in HREELS (see Section 3.1.2), and, in particular, none at $\sim$ 1000 cm^{-1}, the latter gives rise, i.a., to a band at 986 cm^{-1} (see Section 3.2.2). As discussed previously, this reflects the difference in the termination of the films. While the monolayer films have oxygen in a position where it bridges two niobium atoms, the multilayer films have O sitting atop Nb.

Probing the alumina-supported particles by CO adsorption produced, i.a., a weak band at $\sim$ 2190 cm^{-1}, which is assigned to CO adsorbed on Nb^{5+} [140]. An identical band is observed for monolayer niobia films. Therefore, the CO adsorption behavior of supported niobia indicates that the the monolayer niobia films and the niobia particles alike consist of Nb^{5+} ions. On the multilayer films, the presence of Nb^{5+} was confirmed by PES. On the other hand, the mere existence of CO adsorption states makes supported niobia similar to the monolayer films and different from the multilayer films, where CO adsorption did not occur at all, because of the termination by niobyl groups. Hence, alumina-supported niobia shares the CO adsorption behavior of the monolayer niobia films, while the niobyl termination is similar to the multilayer films. It is concluded that the alumina-supported niobia exhibits both niobyl groups and Nb^{5+} cations accessible for CO adsorption.

4.3 Conclusions

This Chapter presents the first surface science study of a niobia/alumina model catalyst. Using STM, phonon IRAS and CO adsorption IRAS, it is shown that niobia forms randomly dispersed nanoparticles with a stoichiometry of Nb_2O_5 and co-existing Nb^{5+} and Nb=O sites on the surface. Therefore, the niobia particles exhibit similarities with niobia films grown of $Cu_3Au(100)$. This model catalyst system is rather stable up to 700 K in UHV. The presence of O_2 during the heating seems to enhance the thermal stability.

The structural and morphological properties are mostly consistent with similarly prepared vanadia/alumina, except for the fact that niobia does not form a sesquioxide phase. Hence, niobia Nb_2O_5, but vanadia V_2O_3 stoichiometries were found. However, when supported on alumina, both oxides primarily exhibit an M=O termination.

Chapter 5

Vanadia Supported on Ceria Films

This Chapter presents a study on a ceria-supported vanadia model catalyst for the oxidative dehydrogenation of methanol to formaldehyde. As outlined in Chapter 1, supported vanadium oxide is an important class of catalytically active materials. Wachs reviewed the influence of various supports on the reactivity of vanadia [63]. As seen in Figure 1.3, CeO_2-supported VO_x revealed the highest turn-over frequency in the oxidative dehydrogenation of methanol. For this reason, ceria was chosen as the support of vanadia in this work.

After an introduction to the relevant literature, the structure of the vanadia/ceria model catalyst and then the reactivity of this system with respect to methanol are addressed.

5.1 Literature Review

5.1.1 Ceria Films

Cerium dioxide, CeO_2, which has a fluorite structure, is an insulator with a band gap of 6 eV [158]. Hence, single crystals of this material can only be studied with methods that do not rely on electrical conduction; e.g., TPD, IRAS, and Atomic Force Microscopy, AFM. Alternatively, annealing to high temperatures may promote the formation of O vacancies, which enhances the electric conductivity of the surface.

The group of Iwasawa studied a $CeO_{2-x}(111)$ (i.e., a reduced CeO_2) single crystal with non-contact AFM [159], providing insight into the defectivity of reduced CeO_2 surfaces. They also report that oxygen adsorption at 300 K

is sufficient for defect healing, and that O vacancies can accomodate two distinguishable methoxy (H_3CO) species for a definition) after adsorption of methanol [160].

Recently, Reichling and co-workers performed more careful AFM studies. This group found that despite the bulk structures of CaF_2 and CeO_2 are isostructural, the respective (111) surfaces created by bulk cleavage differ substantially in the stability of the defects present [161]. Furthermore, they studied the surface termination [162] and the formation of subsurface O vacancies [163].

The limitation to methods that do not rely on electrical conduction could be overcome by the growth of thin, well-ordered cerium oxide films. The first attempts date from the early 1990s. Lambert and co-workers deposited Ce on a Rh foil [164] and on Pt(111) [165]. The group of Nix tried Pd(111) [166] and Cu(111) [167] as substrates for cerium oxide films. However, all of the above procedures involved the oxidation of metallic cerium after its deposition, and it turned out that cerium formed surface alloys, regardless of the substrate material. Additionally, cerium oxide films do not seem to favor a two-dimensional (Frank-van der Merwe), but a three-dimensional (Stranski-Krastanov or Volmer-Weber) growth mode, which represents another hurdle in the preparation of flat films that wet their substrate. The groups of Netzer [168, 169] and Thornton [170] confirmed both the surface alloying and the three-dimensional growth for Rh(111) and Pt(111), respectively. Schierbaum *et al.* studied ceria deposited onto Pt(111) [171, 172] and discovered surface alloying and three-dimensional growth for their preparation method as well.

Mullins and co-workers have been very active in the field of cerium oxide films [173–195]. After using $SrTiO_3(001)$ in the beginning, they discovered Ru(0001) to be most appropriate [175]. For this reason, Ru(0001) is also used in the present work. Subsequently, they studied the reactivities of CeO_x/Ru(0001) and Rh/CeO_x/Ru(0001) with synchrotron PES. Target molecules were, i.a., NO [176], SO_2 [178], CO [177], H_2CO [187], H_3COH [188], H_3CSH [193], and HCOOH [195].

At the Department of Chemical Physics of the Fritz Haber Institute, Berlin, Lu *et al.* invesitigated the growth of cerium oxide on Ru(0001) by means of STM, assisted by LEED and AES [196]. Atomically flat terraces of 5 Å in height were found, corresponding to one CeO_2 bilayer (i.e., two -O-Ce-O- stacks) [168]. Apparently, the step edges of the Ru substrate were decorated first. This film typically grows in two rotational domains and exhibits a rather low point defect density. The point defects observed as depressions were assigned to oxygen vacancies. Moreover, the circular shape of the terraces, arising from the preferential three-dimensional growth, leads to a large number of undercoordinated sites on the step edges. It turned out

that gold preferrably nucleates on point defects, followed by the step edge sites [197].

Hermansson and co-workers have looked into the relative stability of the (100), (110) and (111) facets of CeO_2 by means of density functional theory calculations [198], which was found to ascend in this order. Oxygen vacancies on (110) facets are most favorable on the surface, while they should located sub-surface on (111) facets. In a subsequent publication, it was stated that an oxygen (O^{2-}) vacancy is actually lacking the neutral O atom, while the double negative charge is distributed among two adjacent Ce^{4+}, reducing them both to Ce^{3+} [199]. Further studies comprise the adsorption properties with respect to CO [200] and NO [201,202] and the oxygen vacancy formation at the Pd/CeO_2 system [203].

Independently, the group of Watson has done similar efforts. In agreement with Hermansson and co-workers, they conclude that the (111) facet is the most stable for supported ceria nanoparticles, followed by (110), while (100) exhibits a dipole moment in the direction of the surface normal, which should lead to a reconstruction of this facet [204]. They also confirm the local reduction of two Ce cations in the vicinity of an O vacancy [205]. Theoretical studies on the adsorption of NO, NO_2 and CO on CeO_2 were published subsequently [206–208].

5.1.2 Structure of Supported Vanadia

The preparation of vanadia model catalysts started in growing thin films on a number of substrates. At first, the growth of vanadium oxide films on TiO_2 surfaces was studied experimentally [209–211] and theoretically [212]. Later, metal single crystals, such as W(110) [89], Au(111) [89, 136, 137, 213, 214], Rh(111) [215–217], and $Cu_3Au(100)$ [114–116] were used as well.

As outlined in Chapter 1, industrially employed vanadia catalysts are typically supported on another oxide. This holds particularly true for the oxidation of methanol, which is the subject of Section 5.4.2.

Using DFT calculations and statistical thermodynamics, Todorova *et al.* studied the phase diagram of alumina-supported V_nO_m as a function of vanadia coverage [218]. They found that vanadyl termination is a prevalent feature; however, the transformation of the vanadyl termination into a termination by vanadium atoms was predicted to be more facile on V_2O_5 than on V_2O_5 that form at high coverage on α-$Al_2O_3(0001)$. In a complementary paper, Brázdová *et al.* concluded that the most stable structure of isolated V_2O_5 clusters lack a vanadyl termination, but are only slightly more energetically favorable that a vanadyl terminated structure [219]. Todorova *et al.* extended the study by using meta-stable κ-$Al_2O_3(001)$ as the support,

on which vanadyl reduction is more facile than on α-Al_2O_3 [220].

Deposition of metallic vanadium on metal oxide supports was studied by several groups. Biener *et al.* evaporated V onto an α-Al_2O_3 [221]. Magg *et al.* used the alumina films that are also employed in Chapter 4 in their study of the deposition of metallic vanadium [222]. Both groups observed that vanadium interacted strongly with alumina, by which vanadium oxide was formed. Magg *et al.* even observed incorporation of vanadia into the alumina film. Biener *et al.* [223] and Price *et al.* [224] observed oxidation of vanadium upon deposition on a TiO_2(110) surface.

Magg *et al.* reported on the structure and the CO adsorption properties of vanadium oxide on aluminum oxide films prepared by surface oxidation of NiAl(110) [149, 151, 152]. Kaya *et al.* deposited vanadium in an O_2 environment on an ice-precovered silica surface [225], which promoted the oxidation of vanadium and attenuated the interaction between the vanadia particles and the silica film. The results on supported vanadia nanoparticles are compared to those on V_2O_3/Au(111) films in reference [226].

The group of Vohs investigated the growth of vanadium oxide on a CeO_2 (111) single crystal [227]. Using PES, they observed the formation of V^{3+} species after depositing small amounts of metallic V. Apparently, ceria oxidized vanadium by donating oxygen from its O sublattice. Up to one monolayer of vanadium could be transformed into vanadia with a stoichiometry close to V_2O_3 via exposure to $\sim 10^{-7}$ mbar O_2 at 550 K. About 10^{-3} mbar O_2 at 400 K produced even V^{5+}, yet multilayer vanadium coverages could not be oxidized beyond the sesquioxide stoichiometry with this procedure. Similar findings are reported for TiO_2(110) single crystals [228, 229].

Wang and Madix deposited H_2O and $VOCl_3$ concurrently on the same surface and discovered the formation of V_2O_5 at submonolayer coverage by means of PES [230]. Beyond monolayer coverage, a mixed V^{4+}/V^{5+} oxide seems to form.

A particularly interesting class of vanadia-based materials are the monolayer catalysts that were introduced in Chapter 1. Isolated and also polymeric VO_4 units, from which these catalysts are built, have been characterized in the literature at several instances, by means of Raman spectroscopy [231–238], X-Ray Absorption Spectroscopy, XAS (Extended X-Ray Absorption Fine Structure, EXAFS, and Near-Edge X-Ray Absorption Fine Structure, NEXAFS) [239, 240], solid state ^{51}V Nuclear Magnetic Resonance, NMR, spectroscopy [241], IR spectroscopy [234, 242–244], XPS [245–248], and UV-Vis Diffuse Reflection Spectroscopy, DRS [249–251]. In particular, a Raman band at slightly above 1000 cm^{-1} was reported by Kim and Wachs to represent the vanadyl stretch of isolated VO_4 species [252] (and references therein) in V_2O_5/Al_2O_3. Bañares and co-workers found a similar band for

low coverages of vanadia in alumina [253].

5.1.3 Methanol Oxidation

It is generally accepted that the formation of methoxy groups is the first step in methanol reactions on oxide surfaces [254–258]. There are various subsequent reaction channels for this intermediate. It can recombine with the detached H atom to desorb as methanol. If the methoxy O atom is left on the surface, recombination leads to the desorption of methane instead. Other possible reactions of methoxy groups include decomposition to dioxomethylene, -OCH_2O- [259], and formate, -OCHO- [260], which can be reversibly transformed into each other. Adsorbed formate may then decay to CO or CO_2, if its H atom is transferred to the surface. Dioxomethylene, on the other hand, may donate one O atom to the surface, while the leftover of the molecule desorbs as formaldehyde [257]. Figure 5.1 summarizes the above decay routes.

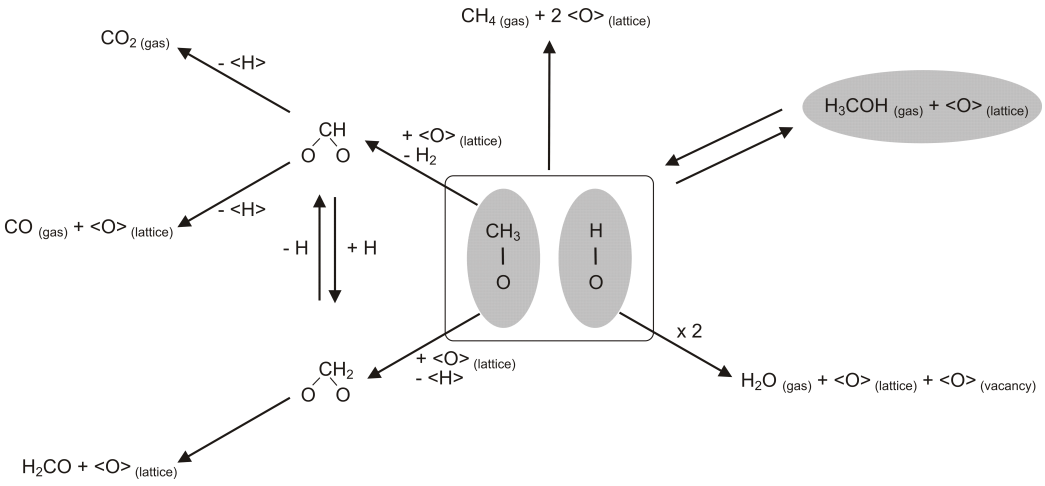

Figure 5.1: Decay routes of surface methoxy species.

In a simplified picture, the mechanism of methanol dissociation typically requires cation-anion pair adsorption sites [254–256, 260, 261]. The cation is also a Lewis acid, due to its electron deficiency. This applies in particular to coordinatively unsaturated cations. Methanol can adsorb to cationic sites via a non-binding electron pair located on the O atom. The hydroxyl H atom of methanol is donated to a nearby anion, which acts as a Lewis base, thereby transforming methanol into methoxy species.

While the presence of Lewis acids and bases and of coordinatively unsaturated cations was thought to be important, various surfaces that fulfill these conditions were found to be inactive for methanol dissociation. On $SnO_2(110)$, to give just one example, the reaction takes place preferentially on Sn^{4+} sites with adjacent bridging oxygen position vacant [257]. Such sites must be created by partial reduction of the surface; however, not only if the extent of the reduction is too little, but also too large, the surface becomes unreactive again. This indicates that attributing the reactivity to the mere presence of cation-anion pair sites is holding some shortages.

Several examples from the literature suggest that metal oxides are selective for the partial oxidation of methanol, while metallic species led to a total decomposition to CO and H_2. This was observed by Schauermann *et al.* for alumina-supported Pd particles [73] and by Mullins and co-workers for ceria films and ceria-supported Rh particles [188,189]. Additionally, Brandt *et al.*, who adsorbed methanol on Fe_3O_4/Pt(111) [74] measured the formation of formaldehyde at $\sim$ 550 K on the pristine film, while at the presence of Pd particles on the surface, CO and H_2 were the sole reaction products. Hence, oxidic catalysts seem to be favorable for the partial oxidation of methanol, and as mentioned in Chapter 1, supported vanadia is particularly well-suited.

Some of the suggested mechanisms of methanol oxidation on metal oxides are presented in the following text. In the net reaction, the conversion of H_3COH to H_2CO removes two H atoms from methanol. It is most probable that they will be first incorporated into surface hydroxyl groups, to which the oxide catalyst donates two lattice O atoms. The recombination of the hydroxyl groups forms water and restores one lattice O. The other O atom desorbs in the water molecule, which creates an O vacancy ($\square$) on the surface.

$$\begin{aligned}
(H_3COH)_{gas} + O_{lattice} &\rightarrow (H_3CO)_{ads} + (OH)_{ads} \\
(H_3CO)_{ads} + O_{lattice} &\rightarrow (H_2CO)_{gas} + (OH)_{ads} \\
2\ (OH)_{ads} &\rightarrow (H_2O)_{gas} + \square + O_{lattice} \\
\hline
(H_3COH)_{gas} + O_{lattice} &\rightarrow (H_2CO)_{gas} + (H_2O)_{gas} + \square
\end{aligned}$$

This mechanism is reported for several surfaces. Namai *et al.* studied the adsorption of methanol on a $CeO_2(111)$ single crystal by means of non-contact AFM [262]. Two kinds of methoxy species are identified after exposing the sample to methanol at room temperature, which are ascribed to adsorption on atop and three-fold hollow sites, respectively. Their density ratio is almost unity. If image acquisition is done in an atmosphere of $\sim 10^{-8}$ mbar H_3COH, line defects are rapidly formed and ascribed to a chain reaction, where a generic vacancy accomodates methoxy, and the desorption of formaldehyde and water simultaneously re-opens the vacancy and creates

a second one adjacent to the first. Kim and Barteau discuss an analogous mechanism on a $TiO_2(001)$ single crystal [255].

At the Department of Chemical Physics of the Fritz Haber Institute Berlin, the oxidation of methanol was studied on V_2O_5 [263] and on V_2O_3 [264] films (both grown on Au(111)). The mechanism was found to be identical for both cases. The surface has to be partially reduced (i.e., only about half of the vanadyl groups are removed). The chain reaction is similar to the one presented by Namai *et al.*. In the case of vanadia films, the O vacancies correspond to the reduced V (former V=O) sites, and the adjacent O atoms to the V=O sites. Methanol adsorbs on V as H_3CO-V, and an adjacent V=O group is turned into VOH. Desorption of water from two VOH sites (which originates from the adsorption of two methanol molecules) leaves one V and one V=O site. Hence, methanol adsorption on n V sites creates another $\frac{n}{2}$ V sites that are available again for another reaction cycle. This chain is self-limited, as each time the number of newly created V sites is half the number in the previous cycle. The total number of V sites in all cycles is 2n, according to the geometric series. Hence, twice as many H_3CO-V form as V sites were originally present. This is confirmed by the STM data of Romanyshyn *et al.* [264].

Wang and Madix investigated formaldehyde formation upon methanol adsorption on $TiO_2(110)$-supported vanadia. They report on the formation of V_2O_5 upon concurrent dosing of H_2O and $VOCl_3$, whereby formaldehyde desorption after methanol adsorption is observed at slightly above 500 K [230]. In a subsequent publication [265], it was proposed that methanol may insert into the V-O bond of the V-O-Ti interface; i.e., analogous to V-O-Si discussed above [266]. The stability of the O=V-O-CH_3 moiety is concluded from vanadium monoxide trimethoxide, O=V(-O-CH_3)$_3$, being stable at room temperature [267]. The suggested mechanism is substantiated by the diminished formaldehyde desorption for vanadia coverages between one and two monolayers, where the access to the V-O-Ti interface is exacerbated for adsorbates.

Bronkema *et al.* postulate the same intermediate [268]. They suggest, however, that it decays via desorption of H_2CO and H_2O, and that subsequent re-oxidation restores the original vanadia species. Subsequently, Bronkema and Bell studied the reaction of methanol on zirconia and zirconia-supported vanadia [269]. While the pristine zirconia offers multiple reaction channels including recombinative desorption of methanol from Zr-OCH_3 and Zr-OH, desorption of H_2O from 2 Zr-OH and methoxy decomposition to CO and H_2 at elevated temperatures, zirconia-supported vanadia mainly transforms methanol to formaldehyde via V-OCH_3 and Zr-OH pairs. The authors also report that on zirconia formaldehyde reacts further to formate, which competitively reduces formaldehyde desorption.

The group of Vohs studied the activity of titania-supported vanadium oxide. While $TiO_2(110)$ was inactive for the conversion of methanol to formaldehyde, the presence of a vanadia "monolayer" on the same surface lead to formaldehyde desorption [270]. Multilayer vanadia coverages, however, were also inactive in this respect. Subsequently, the influence of the oxidation state of vanadium on methanol oxidation was investigated [229]. Vanadia with a predominant V_2O_3 stoichiometry exhibited formaldehyde desorption at 615 K, while V_2O_5 showed formaldehyde formation between 485 K and 517 K, depending on the preparation.

Vohs and co-workers further investigated the vanadia/ceria system. The reactivity of vanadia supported on a $CeO_2(111)$ single crystal toward adsorbed methanol is compared to high-surface area, polycrystalline vanadia/ceria. The structure of vanadia on the ceria single crystal has been studied by the same group beforehand [227] (see also Section 5.1.2). On vanadia supported on the ceria single crystal, formaldehyde desorption occurs at $\sim$ 540 K, while on vanadia supported on polycrystalline ceria the temperature is 525 K.

Moreover, the group of Schwarz studied the oxidation of methanol by unsupported (i.e., gaseous) vanadia clusters by means of mass spectrometry and infrared photodissociation spectroscopy. Mass spectrometry studies in the gas phase facilitate the elucidation of reaction mechanisms, because the time-dependent abundance can be monitored simultaneously for reactants and products; i.e., these experiments are ideally suited for the acquisition of kinetic data. The fragmentation of $[OV(OCH_3)_3]^+$ can proceed via intramolecular H transfer from one methoxy group to either the terminal O ligand or the O atom of one of the other two methoxy ligands [271, 272]. Elimination of H_2CO is observed in both cases. If the parent ion is considered as a model for supported vanadia, these observations would correspond to H transfer from V-bound methoxy to either the vanadyl O atom, forming V-OH, or to the V-O-M interface (M = metal cation of the MO_x support), forming M-OH. The addition of methanol as a reaction gas to vanadium oxide clusters shows that a low oxidation state of vanadium leads to a reduction of methanol, while higher oxidation states ((+3) to (+5)) lead to the elimination of formaldehyde or at least to the formation of a formaldehyde ligand [273, 274]. If formaldehyde is (pre-)formed, then intramolecular H transfer must have occurred, just as for the fragmentation of $[OV(OCH_3)_3]^+$. The use of a vibrational spectroscopy combined with mass spectrometry allowed for *in situ* identification of the structures of the reactants and products [275].

5.2 Preparation

A Ru(0001) single crystal was chosen as the substrate for the cerium oxide films grown within this work, along the lines of Mullins *et al.* [175]. Cleaning of the Ru(0001) typically required three cycles of sputtering for 45 min and by annealing at 1300 K for 5 min.

As discussed in Section 5.1.1, previous attempts in the growth of thin cerium oxide films showed that it does not follow a Frank-van der Merwe (i.e., a strict layer-by-layer) mode [164–167]. Quite on the contrary, it is prone to grow in three-dimensional islands, which imposes an obstacle to the growth of a ceria film that wets the entire substrate homogeneously. This could be overcome by an initial cerium deposition at 100 K, which limited the diffusion of ceria on the surface and enhances surface wetting [276]. Meanwhile, the chamber was backfilled with 10^{-7} mbar O_2, which was maintained throughout the entire preparation. The deposition was continued at 700 K, in order to promote complete oxidation. The duration of the deposition stages at 100 K and 700 K was determined by LEED. By trial and error, these times were varied, until Ru(0001) spots could not be detected anymore by LEED. After the Ce deposition was ended, the sample was oxidized for another 30 min at 980 K.

Vanadium oxide was prepared by means of physical vapor deposition of metallic vanadium in an oxygen ambient (10^{-7} mbar O_2). Vanadium was also deposited in UHV. In both cases, the vanadium deposition rate was calibrated at 0.15 Å min^{-1} using the quartz microbalance.

5.3 Characterization of the Ceria Films

5.3.1 LEED and STM

After a successful preparation, LEED was to show a (1.4×1.4) structure with respect to Ru(0001)-(1×1) (Figure 5.2 (a)).

STM data in Figure 5.2 (b) were provided by M. Baron. It is obvious that the film wets the substrate surface completely. The three-dimensional growth mode is concluded from the presence of numerous islands, the shape of which is triangular or composed of several merged triangles. The step height at the island borders is $\sim$ 3 Å. No signs of holes in the film are observed.

5.3.2 PES

Figure 5.3 presents PES data for the Ce 3*d* region of the ceria film (875 eV - 925 eV), which are consistent with the data of Mullins *et al.* [174]. There,

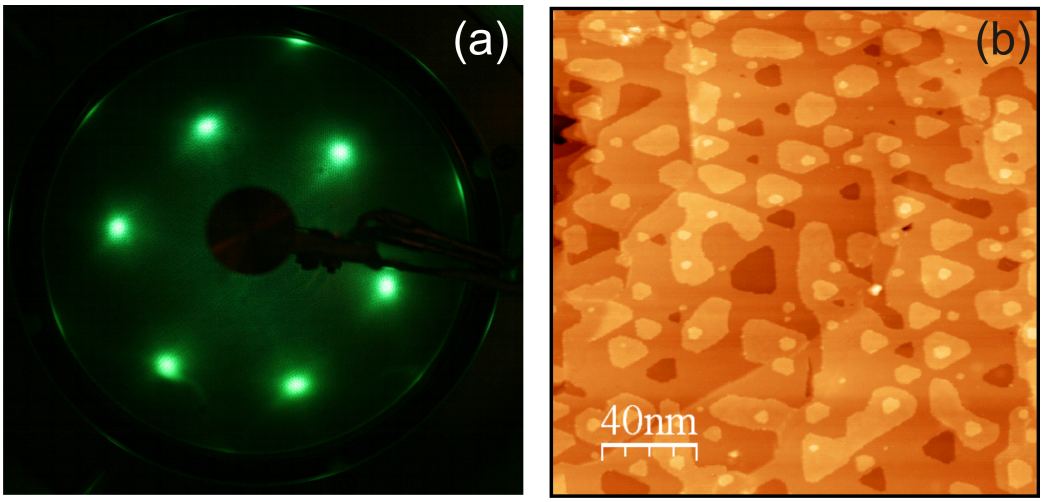

Figure 5.2: (a) LEED pattern of CeO_2/Ru(0001) at 70 eV; (b) STM image of CeO_2/Ru(0001) (provided by M. Baron), 200×200 nm^2, V = 3.1 V, I = 0.1 nA.

cerium was shown to be exclusively Ce^{4+}, which implies CeO_2 stoichiometry for the films prepared in this work. However, the PES results of CeO_2 exhibit a rather complex structure of six peaks in total, and hence, they deserve an extended discussion.

The PES data on rare-earth compounds with a particular emphasis on cerium compounds have been reviewed by Kotani *et al.* [277]. It is, however, instructive to discuss the case of La (electronic configuration of the neutral atom: [Xe] $5d^1$ $6s^2$) before Ce ([Xe] $4f^1$ $5d^1$ $6s^2$). The $3d$ region of La exhibits two peaks, which are too far separated to be explained by multiplet splitting. Instead, they arise from final state effects. The $4f^0$ level of La is located above the Fermi edge, and it hybridizes with the conduction band. In the final state, the attractive potential of the core hole has shifted the $4f$ level below the Fermi edge. Hence, two scenarios are conceivable, in which a conduction band electron either jumps or does not jump to the $4f$ level. In the former case, the new $4f^1$ electron adds to the shielding of the the photo-electron core hole, which becomes more effective. In the latter case, however, no additional shielding is provided. This results in two different binding energies for the photo-electron and thus in two separate peaks in the PE spectra.

The ground state of Ce is a quantum-mechanical mixture of $4f^0$ and $4f^1$ configurations. Again, the $4f$ level is located below the Fermi edge in the final state. However, the contributions of $4f^0$ and $4f^1$ to the ground

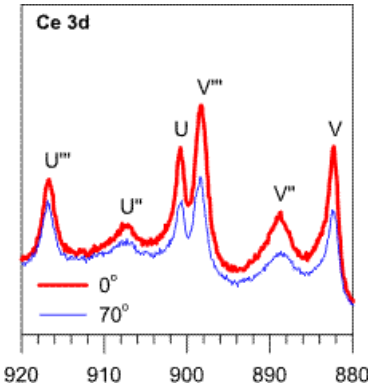

Figure 5.3: PE spectra of the ceria films in the Ce $3d$ range at two angles (0° and 70°).

state must be considered individually, which leads to a total of three possible configurations for the final state: $4f^0$, $4f^1$, and $4f^2$. These three features undergo additional spin-orbit splitting, from which the six PES peaks arise, as observed in Figure 5.3.

5.3.3 IRAS

CO/IRAS experiments were carried out to verify the uniformity of the films; i.e., whether there are holes exposing the substrate. The spectrum is shown in Figure 5.4 (a). As expected from an O-terminated oxide film, the extent of CO adsorption, which occurs in one single IR-detectable state only (2173 cm^{-1}), is very small ($\sim 0.05\%$). Herzberg reports an almost identical reference value of 2170 cm^{-1} [278]. The small extent of CO adsorption substantiates the conclusion drawn from the STM images that the CeO_2 films have a low defectivity. Figure 5.4 (c) presents the spectra of CO adsorption on clean and oxidized Ru(0001), where the oxidation conditions were the same as during the preparation of a ceria film, but without Ce deposition. This intended to prepare a sample that would mimic the surface within potential holes; yet the discrepancy between Figure 5.4 (a) and (c) proves that such holes are absent. This confirms the above STM and PES results.

Figure 5.4 (b) depicts the IR spectrum of CeO_2/Ru(0001) in the phonon range. It is referenced to the clean Ru(0001) substrate. The only peak observed is located at 595 cm^{-1}, and is very strong ($\sim 5\%$). The phonon spectrum of a CeO_2 single crystal reported in the literature [279] also possesses only one single peak, which is located at 542 cm^{-1}.

This spectrum, however, does not exhibit any band between 980 cm^{-1} and

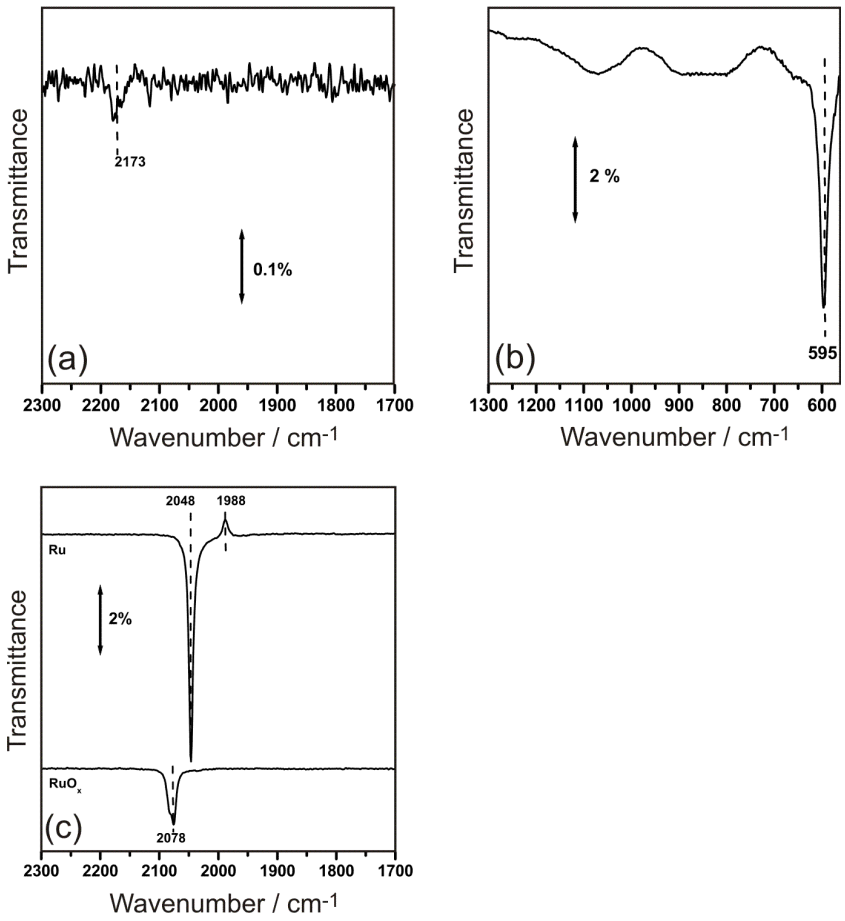

Figure 5.4: IRAS data of CeO_2/Ru(0001). (a) CO adsorption; (b) phonon range; (c) CO adsorption on Ru and oxidized Ru for comparison (spectra offset for clarity). The oxidation procedure was equivalent to the preparation conditions of ceria, but without Ce deposition, in order to mimic the surface within the holes in the film, if any. The strong discrepancy between (a) and (c) clearly shows that there are no such holes.

990 cm^{-1}. Hence, the band observed in this region after deposition of small amounts of vanadium in 10^{-7} mbar O_2 at 100 K (see Figure 5.9) is not a feature of the ceria films.

5.4 Results and Discussion

5.4.1 Structure of Vanadia/Ceria

STM

The STM images of a sample of ceria-supported vanadia ($\sim$ 0.1 Å) shown in Figure 5.5 (a) - (c) are provided by M. Baron, and (d) is provided by J. Sainio ($\sim$ 0.2 Å).

Figure 5.5 (a) shows that the ceria film is decorated by highly dispersed protrusions, which are identified as vanadia. The close-up image in Figure 5.5 (b) show that the vanadia particles are small and all of the same diameter and height. (The less bright double images to the lower right of each particle are attributed to a double tip effect.) The atomic resolution in Figure 5.5 (c) enables to observe that the vanadia species sit on top of the protrusions of the ceria film, and, moreover, that their size does not exceed the size of one atom. Hence, this image clearly shows that vanadia forms monomeric species at this low coverage.

In Figure 5.5 (d) the coverage is about twice as high as in (a) - (c). Yet the image shows that vanadia is still highly dispersed and randomly distributed across the terraces.

PES

Synchrotron PE spectra were measured after vanadium deposition onto the cerium oxide film at 100 K in 10^{-7} mbar O_2 for coverages of 0.1 and 0.7 Å and presented in Figure 5.6. For comparison, the spectra of vanadia films grown on Au(111) are also presented. The spectrum of the low vanadium coverage (0.1 Å) strongly resembles the one of V_2O_5/Au(111), as the peak at 517.5 eV dominates the V $2p_{3/2}$ region, and the shoulder at 516.3 eV is very weak. However, at 0.7 Å, the shoulder has gained intensity relative to the main peak at higher energy (which is now at 517.2 eV).

The V $2p_{3/2}$ signal at 516.3 eV corresponds to V^{3+}, while 517.5 eV relates to fully oxidized V^{5+}. It seems that ceria-supported vanadia, in particular for very low coverages, is fully oxidized, while at higher coverages V^{3+}-containing species become increasingly abundant.

It must be mentioned, however, that Shapovalov and Metiu predict the experimentally observed similarity with V_2O_5 PE spectra in a theoretical study on ceria-supported vanadia, but claim that the supported vanadia contains V^{3+} nevertheless [280]. On the other hand, Wong *et al.*, who studied the oxidation states of vanadia supported on a TiO_2 single crystal, report V(+5) to appear at $\sim$ 517 eV, based on a comprehensive literature review

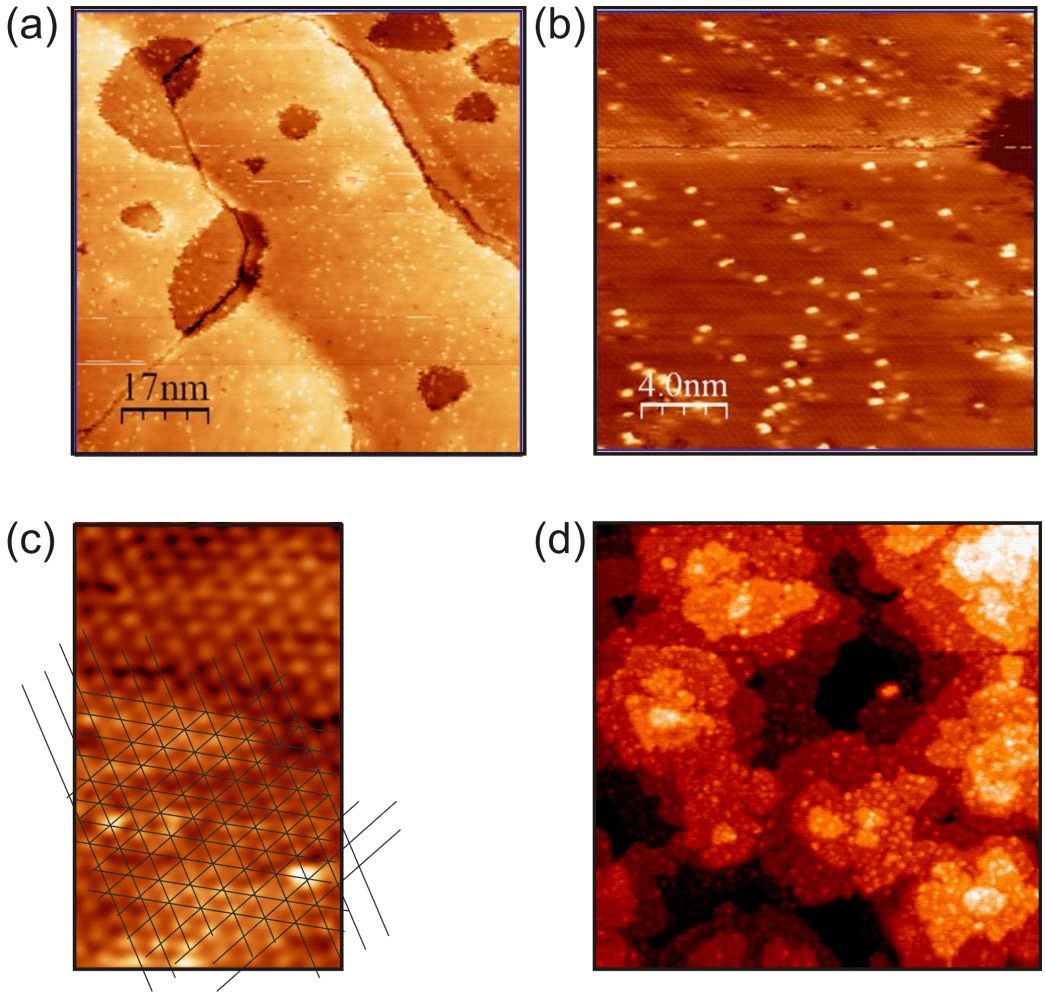

Figure 5.5: STM data of ceria-supported vanadia ((a) - (c) $\sim$ 0.1 Å, provided by M. Baron; (d) $\sim$ 0.2 Å, provided by Jani Sainio). (a) 85×85 nm^2, 2.2 V, 0.2 nA; (b) 20×20 nm^2, 2.6 V, 0.26 nA; (c) 3.5×4.7 nm^2, 1.4 V, 0.17 nA (atomic resolution); (d) 60×60 nm^2, 3 V, 0.1 nA. The fact that each bright protrusion in (b) has an artificial image to its lower right is attributed to a double tip.

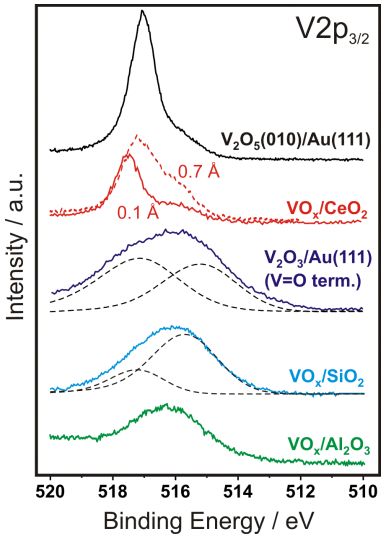

Figure 5.6: PES data of ceria-supported vanadia (this work; solid line: 0.1 Å V, dashed line: 0.7 Å V, both deposited at 100 K in 10^{-7} mbar O_2), of V_2O_3 films [89] and V_2O_5 films [75] grown on Au(111), as well as of vanadia supported on alumina [151] and silica [225]. The spectra are offset for clarity.

[229] (and references therein). The 517.5 eV measured here even slightly exceed this range, which can be, however, attributed to final state effects in highly dispersed vanadia particles. This assumption is corroborated by the shift of the main peak to a slightly lower energy at 0.7 Å V. Therefore, it seems most plausible that deposition of 0.1 Å vanadium on the ceria films at 100 K in 10^{-7} mbar O_2 leads indeed to the formation of fully oxidized vanadia; i.e., a species that contains V^{5+}.

The PE spectra of alumina- and silica-supported vanadia particles, which are also given in Figure 5.6, are in a very good agreement with the spectrum for V_2O_3/Au(111) films. The preparation conditions for all three of these vanadia species were rather mild; i.e., a sample temperature of 300 K and an oxygen pressure of 10^{-7} mbar O_2. It is generally accepted that the sesquioxide (V_2O_3) is the typical stoichiometry of vanadia, if the sample was exposed to $\leq 10^{-6}$ mbar O_2. Formation of V_2O_5/Au(111) films, however, requires oxygen pressures as high as 50 mbar and elevated temperature [75]. Keeping this in mind, it is remarkable that the PE spectra for low vanadium coverage on cerium oxide match V_2O_5 rather than V_2O_3, even though the conditions were far less stringent in the present case than for the V_2O_5 films.

This reflects the well-known fact that ceria may act as an oxygen buffer

[64, 65]. Moreover, the degree of dispersion is typically lower on silica and alumina, due to a weaker interaction of vanadia with these supports. Accordingly, the particle size is larger there than for ceria at comparable coverages. Combining this with the prevalent V^{3+} on silica and alumina, it is concluded that larger particles are more prone to exhibit this lower oxidation state, while in small particles on ceria vanadium is fully oxidized. The peak ratio of the two vanadia/ceria spectra confirms this trend. It seems that there is a duality in the oxidation states of vanadia: at low very coverages (where the STM images in Figure 5.5 reveal isolated vanadia) vanadium is present as V^{5+}, while polymerization seems to occur at higher coverages, leading to an increasing fraction of V^{3+}.

IRAS

IR spectroscopy was used to study the interaction between the ceria film and the vanadium deposits in the phonon range. Deposition parameters to vary were the composition of the gas phase in the chamber (10^{-7} mbar O_2 or UHV), the sample temperature (100 K or 300 K) and the vanadium coverage (ranging from 0.1 Å to 2.0 Å). A flashing series was performed for each sample, with 900 K being the highest temperature for each sample.

The spectra of the as-prepared sample were referenced to the ceria film at the temperature of vanadium deposition. However, the sample needed to be moved from the IR position in front of the vanadium evaporator, and back afterward. This caused the IR base line to deviate from a flat line. Therefore, for subsequent spectra in the same set of experiments, which were taken after flashing to the indicated temperature and cooling to the deposition temperature, the as-prepared vanadia/ceria sample served as the new reference. Since the sample was not moved throughout the flashing series, these spectra exhibit a base line of better quality.

To start, Figure 5.7 presents the case of 2.0 Å vanadium deposited in 10^{-7} mbar O_2 at 300 K. At 300 K, a rather broad peak centered at $\sim$ 1040 cm^{-1} is observed. Comparison with other supported vanadia species [149, 151, 152] and with vanadia films [89, 136, 137] allows for a straightforward assignment to the stretch of the vanadyl groups. Magg *et al.* found a bond order of $\sim$ 2 for the vanadyl groups of alumina-supported vanadia [88]. Upon flashing to 500 K and 700 K, the signal sharpens significantly and shifts to slightly higher wavenumbers, while it strongly gains intensity. The flash to 900 K, however, seems to have induced dramatic morphological changes. Several new bands appeared at 914, 948 and 1018 cm^{-1}, and the 1041 cm^{-1} band is now negative, indicating the disappearance of the related vibration upon heating. Note that the same treatment also promoted particle sintering and

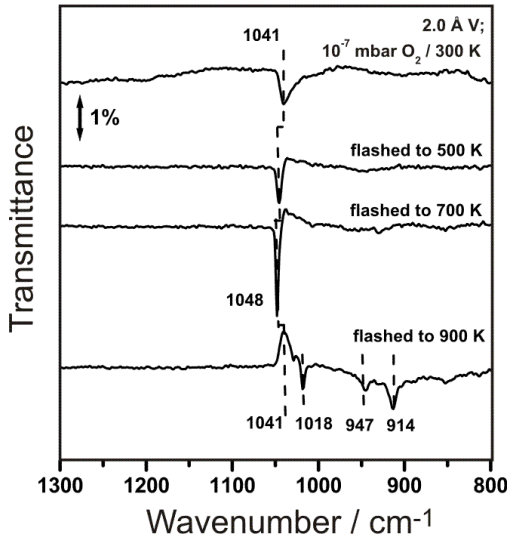

Figure 5.7: Phonon spectra (IRAS) taken after deposition of 2.0 Å vanadium in 10^{-7} mbar O_2 at 300 K. The first spectrum is referenced to CeO_2/Ru(0001). The sample was subsequently flashed to 500 K, 700 K and 900 K, the spectra of which are referenced to as-prepared VO_x/CeO_2/Ru(0001). The spectra are offset for clarity.

even particle migration into the film in the case of alumina-supported niobia, which is subject of Chapter 4. Hence, a similar intermixing between vanadia and ceria is proximate. Note that the new bands are quite sharp, indicating that the "mixed oxide" phase is rather well-defined. This can be rationalized on the basis of the large vanadia coverage forming a coherent mixed V-Ce oxide across the entire surface. The formation of $CeVO_4$ from exposing vanadia/ceria to elevated temperature was reported by Martínez-Huerta *et al.* [281]. Although this literature example exhibits a phonon spectrum that differs from the present case, it demonstrates nevertheless that intermixing is possible indeed. The differences in the phonon spectra can be attributed to different preparation procedures.

As can be seen in Figure 5.8 for 0.4 Å vanadium, deposited under otherwise identical conditions, the spectrum at 300 K looks somewhat different from the 2.0 Å sample. The peak associated with the stretching mode of the vanadyl group is still present at 1036 cm^{-1}, although less intense, reflecting the smaller coverage; however, it is now accompanied by another peak at 1006 cm^{-1}. It is difficult to discern, because the sample had to be moved from the IRAS to the evaporation position and back between taking the reference and the spectrum; however, after flashing the sample to 500 K, 700

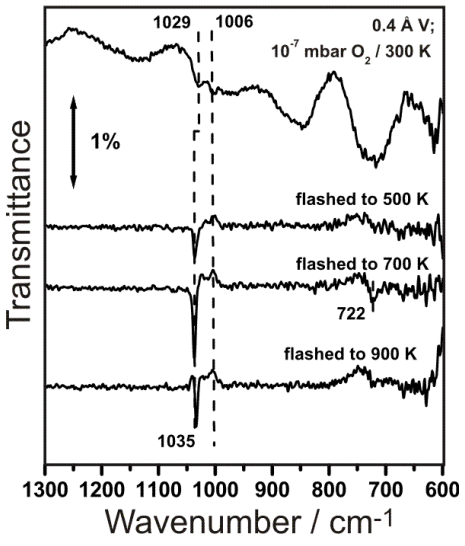

Figure 5.8: Phonon spectra (IRAS) taken after deposition of 0.4 Å vanadium in 10^{-7} mbar O_2 at 300 K. The first spectrum is referenced to CeO_2/Ru(0001). The sample was subsequently flashed to 500 K, 700 K and 900 K, the spectra of which are referenced to as-prepared VO_x/CeO_2/Ru(0001). The spectra are offset for clarity.

K and 900 K, there is a negative peak at the same position, indicating the species was removed by the flashing. As the new peak is still in the range for stretching modes of vanadyl groups [89], it is assumed that it may represent a different kind of vanadyl group.

Since the 1006 cm^{-1} band is apparently related to lower coverages, it is essential to consider the properties of vanadia in this range. As discussed above for the PES results, low vanadium coverages lead to the formation of V^{5+}-containing particles. Tepper *et al.* report the experimental wavenumbers for V=O groups in V_2O_5 single crystals to range from 975 cm^{-1} to 1037 cm^{-1} [282]. The calculated number is 126.4 meV (1019 cm^{-1}) [283]. 1006 cm^{-1} falls well into this range, and hence, it is assigned to the vanadyl stretching mode of fully oxidized vanadia particles.

In the subsequent flashing series, the 1006 cm^{-1} band disappears after heating the sample to 500 K, a behavior that can be explained by vanadia sintering, whereby the V^{5+} species would merge into larger particles. The 1036 cm^{-1} band becomes more pronounced after the flash to 500 K. The latter wavenumber is typical for V_2O_3 [89, 136, 137, 149, 151, 152], which is the suggested stoichiometry at higher coverage, where larger particles should be prevalent. Moreover, a dipole coupling effect, as mentioned in Section 2.6.3,

has to be considered. Since higher temperatures seem to induce particle sintering, the particle surface is enlarged concomitantly. Hence, more vanadyl groups will reside in close proximity on one particle, leading to a stronger dipole coupling between their stretching modes, and eventually to the observed blueshift of the corresponding band. While the explicit influences of the oxidation state and the particle size cannot be reasonably predicted without computational support, the above considerations are self-consistent and suggest that the band at 1006 cm^{-1} is the lower limit for the vanadyl stretching mode on ceria-supported vanadia. Additional combined STM and IR studies show that the STM images shown in Figure 5.5 exhibit a band at 1006 cm^{-1}, which is, therefore, identified as the vibrational signature of monomeric vanadia. Such species have a VO_4 stoichiometry, as discussed at the end of Section 5.1.2. Kim and Wachs report a Raman band at slightly above 1000 cm^{-1} to be the vibrational signature of such monomeric species [252]. This is in almost perfect agreement with the present case, considering additionally the differences between Raman and IR spectroscopy. These authors found vanadia to be fully dispersed up to a coverage of one monolayer; i.e., only at the completion of one monolayer the vanadia species start to polymerize. A similar blueshift to 1031 cm^{-1} with increasing coverage was also observed.

Intermixing between the two oxides at 900 K cannot be unambiguously identified in the present case, as none of the bands observed in Figure 5.7 are detected. However, it may well be that the signal intensity is simply too weak at a coverage as low as 0.4 Å. This assumption is supported by the slight intensity loss in the vanadyl band at 900 K, indicating that the particle structure is indeed somewhat deterioriated, which could be the beginning of oxide intermixing.

Figure 5.9 shows the spectra of deposition of vanadium in 10^{-7} mbar O_2 at 100 K for 0.1, 0.3 and 0.7 Å. All samples were subsequently flashed to 300 K, 500 K, 700 K and 900 K. Comparison with Figures 5.7 and 5.8 reveals both similarities and differences. It is a common feature for all depositions in O_2 that a vanadyl stretch is observed at 300 K, regardless of the deposition temperature. For 0.1 and 0.3 Å, this band is close to 1000 cm^{-1}, which is consistent with the low coverage vanadyl stretch observed for 0.4 Å vanadium deposited in O_2 at 300 K (see Figure 5.8). Flashing the sample induces a similar shift to higher wavenumbers. For 0.7 Å, the vanadyl stretch is located at 1030 cm^{-1} already at 300 K, which corresponds to the high coverage vanadyl peak.

Intermixing is not observed for 0.1 and 0.3 Å; however, for 0.7 Å coverage a new broad band is observed after flashing to 900 K, which is centered at $\sim$ 950 cm^{-1}. The position is consistent with the band at 948 cm^{-1} observed for 2.0 Å (see Figure 5.7). As discussed above, the mixed oxide could cover the

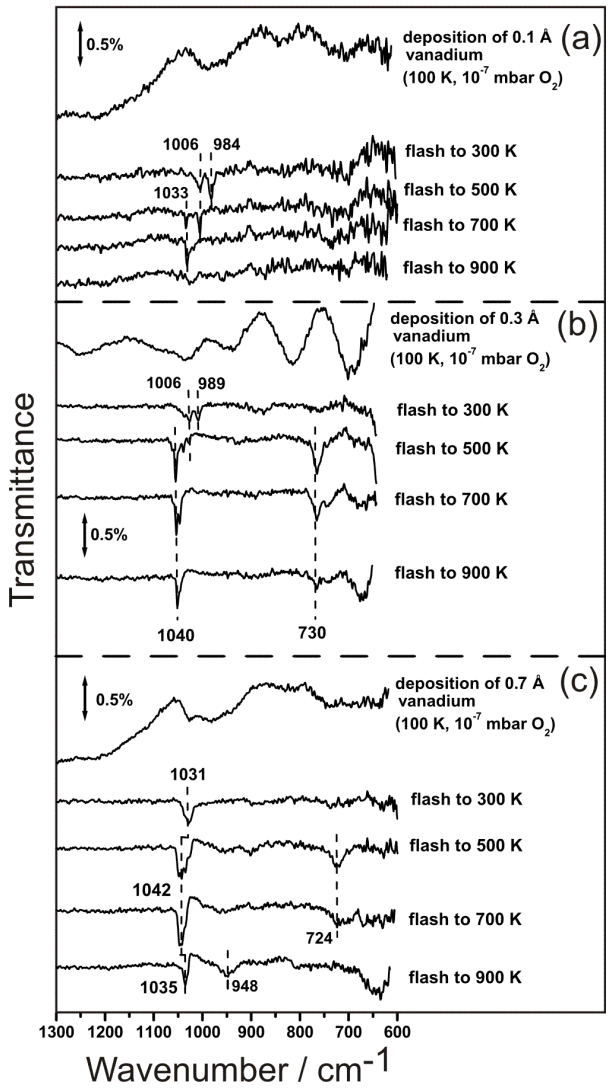

Figure 5.9: IRAS data of deposition of (a) 0.1 (b) 0.3 and (c) 0.7 Å vanadium in 10^{-7} mbar O_2 at 100 K, respectively. The first spectrum in each part is referenced to CeO_2/Ru(0001). Each sample was subsequently flashed to 300 K, 500 K, 700 K and 900 K, the spectra of which are referenced to as-prepared VO_x/CeO_2/Ru(0001). The spectra are offset for clarity.

entire surface at very high coverages, while at 0.7 Å it is more likely to occur in localized areas. It may be speculated that this lack of coherence might result in a less ordered mixed phase, represented by a broader band.

For 0.1 Å and 0.3 Å, a sharp band appears after flashing to 300 K at 984 cm^{-1} and 989 cm^{-1}, respectively. For 0.7 Å, the band is not observed, and neither if the deposition was done in UHV (see Figure 5.10). Hence, this feature must be associated with both the presence of oxygen and a low vanadia coverage. Its exact nature, however, requires an extended discussion. The facts that this peak persisted despite replacing the crucible of the Ce source, the material of which may alloy with Ce after some time of usage, and that no Ce traces could be found on the Ru(0001) crystal by Auger Electron Spectroscopy after three cleaning cycles, allow to rule out an impurity as the explanation.

Three other possible origins for this band are discussed in the following text. First, it may be assigned to V=O species, as it falls still into the range of vanadyl stretching modes. As mentioned above, Tepper *et al.* report this range to be between 975 cm^{-1} and 1037 cm^{-1} for V_2O_5 single crystals [282]. However, the above-presented arguments imply that 1006 cm^{-1} is the lower limit for vanadyl bands in the present work, which belongs to isolated VO_4 species.

Another option is to attribute this peak to a vibration of the V-O-Ce linkage at the interface. A similar band is observed for alumina-supported vanadia, where a peak at 950 cm^{-1} was assigned to vibrations of the corresponding V-O-Al group [151]. Although this number differ from the 984 cm^{-1} of vanadia/ceria by more than 30 cm^{-1}, the range covered by the vibrations at the vanadia/support interface is rather large. For example, the corresponding V-O-Si mode was calculated to be in the range of $\sim$ 1000 cm^{-1} - 1030 cm^{-1} [149]. On the other hand, the assignment of the 984 cm^{-1} band to an interface phonon contradicts the fact that the V-O-Al and V-O-Si bands become more pronounced, as the vanadia coverage increases, while on ceria the intensity between 980 cm^{-1} and 990 cm^{-1} vanishes at a coverage of 0.7 Å V. In fact, interface phonons are expected to be more pronounced at higher coverages, because of the increased particle size. Yet alumina-supported vanadia was not found to undergo a coverage-related transition in the oxidation state, which ceria-supported vanadia does. It could be that the bands at 984 cm^{-1} and 989 cm^{-1} represent the interface vibration of fully oxidized vanadia, but no equivalent band could be identified in the cases of 2.0 Å and even 6.0 Å (not shown), where vanadia is present as the sesquioxide. Hence, this assignment is also questionable.

The third possibility is the assignment to a peroxo, O_2^{2-}, species, as it was observed by Abu al-Haija *et al.* on V_2O_3 films grown on Au(111) [137]. When

the vanadyl termination was removed by means of electron bombardment, adsorption of molecular O_2 on this reduced surface and subsequent heating could restored it, which proceeded via a peroxo precursor. The related IR band for the vanadia films is located at 951 cm^{-1}, and thus substantially lower than in the present case. However, Asmis suggests 995 cm^{-1} as the wavenumber of the peroxo stretching mode in unsupported $V_3O_8^+$ [284]. This gas phase cluster is prepared at 300 K or even slightly above, and hence, a peroxo-vanadium species in vanadia/ceria might exhibit a comparable stability. As both the peroxo-vanadium and the vanadyl group are V/O moieties, it is well conceivable that their formation is impeded by a similar energy barrier. This could explain why neither are formed at 100 K, but at 300 K (see Figure 5.9).

Experiments complementary to those presented in Figure 5.9 were carried out, with a vanadium deposition at 100 K in UHV. Coverages studied were again 0.1 Å, 0.3 Å and 0.7 Å. The spectra are presented in Figure 5.10 (a) to (c). After deposition of vanadium in UHV formation of a vanadyl peak in IRAS is observed after a flash to 500 K. The wavenumber of this feature is $\sim$ 1010 cm^{-1} for 0.1 Å. At 0.3 Å, this peak becomes broader, enveloping another peak at $\sim$ 1030 cm^{-1}. While the band at 1010 cm^{-1} is slightly more intense than the one at 1030 cm^{-1} for the case of 0.3 Å, the situation is reverted for 0.7 Å. Flashing to 700 K shifts all vanadyl peaks to above 1030 cm^{-1}, including a gain in intensity, while flashing to 900 K results in intensity loss and a shift back to slightly lower wavenumbers.

The results are straightforwardly rationalized on the basis of the previous results on vanadium deposition in 10^{-7} mbar O_2. The wavenumbers of the vanadyl peaks follow the same trend here as found upon deposition in O_2. Flashing to 700 K reveals similar sintering tendencies for the particles, and again, flashing to 900 K seems to cause formation of mixed vanadium cerium oxide.

Wong and Vohs report that vanadium deposited on ceria in UHV can be oxidized, whereby ceria gets partially reduced [227]. Since Magg *et al.* observed a similar effect even on alumina [222], which is actually non-reducible, an even stronger interaction between the reducible cerium oxide and the vanadium deposits is expected. Such an interaction would be the migration of oxygen from ceria to atop the vanadium overlayer, which is the only conceivable explanation for the observed formation of V=O in this case.

IRAS data shown in Figure 5.11 could be another indication that the O atoms of vanadia/ceria are somewhat mobile. Spectrum (i) in Figure 5.11 (a) was taken after deposition of 0.2 Å vanadium in UHV on the ceria film at 100 K. Due to the low temperature, the sample adsorbed CO from the background. The wavenumber of 1996 cm^{-1} is typical for CO sitting atop

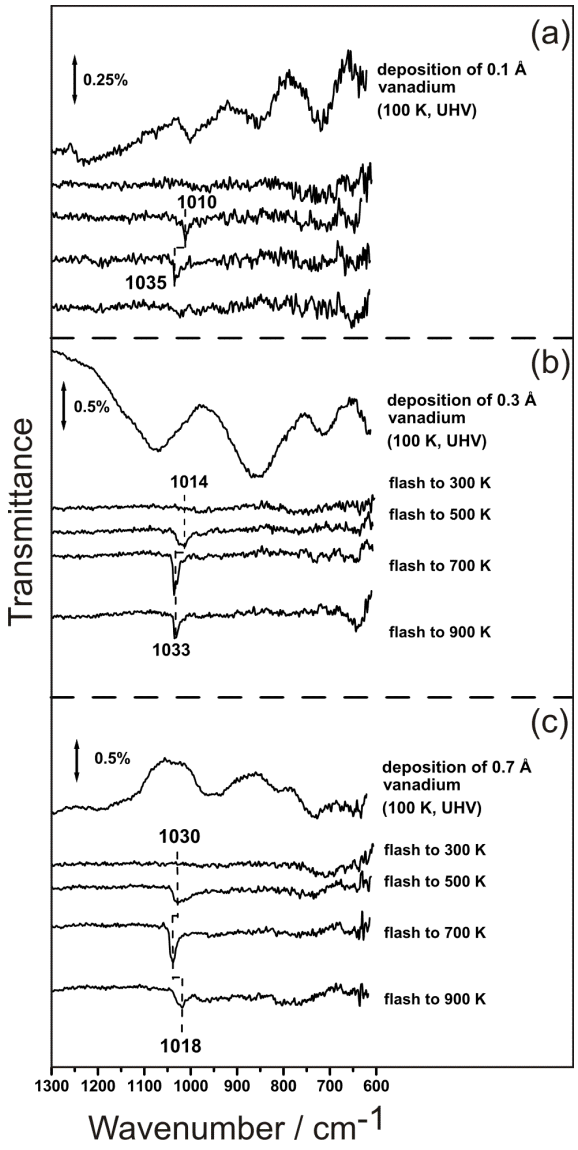

Figure 5.10: IRAS data of deposition of (a) 0.1, (b) 0.3 and (c) 0.7 Å vanadium in UHV at 100 K, respectively. The first spectrum in each part is referenced to CeO_2/Ru(0001). Each sample was subsequently flashed to 300 K, 500 K, 700 K and 900 K, the spectra of which are referenced to as-prepared VO_x/CeO_2/Ru(0001). The spectra are offset for clarity.

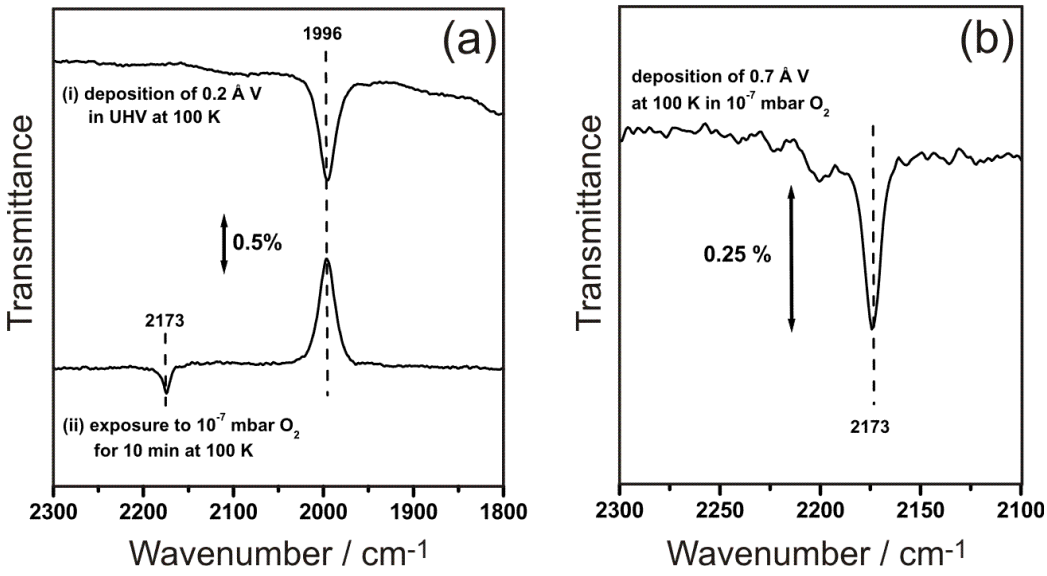

Figure 5.11: (a) IRAS data (background adsorption of CO)) of (i) 0.2 Å vanadium deposited in UHV at 100 K and (ii) subsequently exposed to 10^{-7} mbar O_2 for 10 min at 100 K. For (i), the reference is the spectrum of the pristine CeO_2 film. For (ii), the reference is spectrum (i). (b) IRAS data in carbon monoxide C/O stretching region of 0.7 Å vanadium deposited on CeO_2 in 10^{-7} O_2 at 100 K (referenced to clean ceria). The spectra are offset for clarity.

metallic V [285]. However, after the sample was subsequently exposed to 10^{-7} mbar O_2 for 10 min at 100 K (spectrum (ii)), the integral adsorption of the 1996 cm^{-1} band is now negative, with about the same absolute value as in spectrum (i), where it is positive. Hence, this adsorption state of CO has entirely vanished, while a new and smaller band emerged at 2173 cm^{-1}. Comparison with Figure 5.4 (a) reveals that this band essentially identical to CO adsorption at ceria defects. However, Figure 5.4 (a) shows a saturation coverage of CO on the as-prepared CeO_2/Ru(0001) film, where the peak intensity is found to be $\sim 0.05\%$. In Figure 5.11 (b), on the other hand, a band at the same position is distinctly more intense ($\sim 0.2\%$; i.e., about four times higher), even though it only occurred through re-adsorption from the background.

The identical wavenumbers suggest that the O_2 treatment affected the deposits, such that the defectivity of ceria was enhanced. However, a mere coincidence, albeit not very likely, must be considered as an alternative. Magg *et al.* studied the adsorption of CO on alumina-supported vanadia,

which may serve for comparison with the present case. They found a total of four peaks ($P0$ to $P3$ in their notation) [152]. While $P3$ (2031 cm^{-1}) can be ruled out immediately, because the wavenumber is substantially lower, an analogy to $P0$ ($\sim$ 2180 cm^{-1}), $P1$ (2169 cm^{-1} - 2196 cm^{-1}) or $P2$ (up to 2165 cm^{-1}) must be considered and discussed. $P0$ is related to low coverage, to which the 0.2 Å V of the present experiment certainly belong. However, the band at 2173 cm^{-1} is also present for 0.7 Å V (Figure 5.11 (b)), which is well beyond low coverage. The wavenumbers of $P1$ (2169 cm^{-1} for $\sim$ 0.1 Å V - 2196 cm^{-1} for $\sim$ 1.0 Å V) and $P2$ (2115 cm^{-1} for $\sim$ 0.1 Å V - 2165 cm^{-1} for $\sim$ 0.6 Å V), on the other hand, were found to be strongly coverage-sensitive, while the 2173 cm^{-1} is the same for vanadium coverages of 0.2 Å and 0.7 Å. Moreover, the lower limit of the $P2$ range is quite far from 2173 cm^{-1}. Since all of $P0$ to $P3$ seem to fail to apply, it is concluded that the band at 2173 cm^{-1} should be tentatively assigned to the adsorption of CO on ceria defects, formed upon deposition of vanadium in O_2 or by post-adsorption of O_2.

Defects additionally created by an exposure of vanadia/ceria to O_2 would have to be located at the particle/substrate interface. Given the differences in reactivity of samples (i) and (ii) in Figure 5.11 (a) with respect to the formation of formaldehyde (see Figure 5.15 in Section 5.4.2), it cannot be ruled out that interfacial defects are prerequisite adsorption sites of methanol for the vanadia-related reactivity channels to be observed. On the other hand, it must be stated that defect sites on ceria are commonly accepted to be O vacancies. It is, however, counterintuitive that the supply of additional oxygen from the gas phase would lead to a greater number of missing O atoms in the ceria film. It could be envisioned that the gaseous O_2 can somehow trigger the beginning of the vanadium oxidation, in the course of which lattice O from ceria can then also become mobile and can be incorporated into VO_x. Nevertheless, this is mere speculation and definitely requires additional computational support for the energetics of the described process.

5.4.2 Methanol Oxidation

TPR

The production of formaldehyde on the sample surface was studied by TPR. As outlined in Section 2.8, the mass spectrometer has to ionize the desorbing species in order to monitor them. For methanol and formaldehyde, this process may cause fragmentation, and hence, it is crucial to choose the most appropriate (i.e., the most abundant) fragment ion for each molecule. Alternatively, the ionization potential may be lowered, but this reduces the signal intensity, which is already quite small in the present case.

Methanol adsorption on vanadia/ceria was studied for the cases, where vanadium was deposited in 10^{-7} mbar O_2 at 100 K. Methanol was adsorbed at the same temperature, and a flash to 300 K (mostly) removed the unreacted methanol. Figure 5.12 depicts the TPR spectra (a) from the pristine ceria film, (b) from vanadia/ceria (deposition of 0.3 Å vanadium in oxygen) in the first run, and (c) from vanadia/ceria in the second run.

The pristine ceria film shows formaldehyde formation at 600 K (Figure 5.12 (a)). This peak is found in all TPR experiments. Figure 5.12 (b) shows the first TPR run, which was taken after the deposition of 0.3 Å vanadium in 10^{-7} mbar O_2. In addition to the ceria-related feature at 600 K, two more peaks are observed: one at $\sim$ 510 K, and one at a temperature as low as 340 K. The three peaks are referred to as α (340 K), β (510 K), and γ (600 K), respectively. However, in the second run (Figure 5.12 (c)) the γ signal is maintained, while β is considerably suppressed, and α has vanished completely. This difference between the first and the second TPR has been observed for all vanadia/ceria samples, regardless of the vanadia coverage. Note again that all three samples were pre-flashed to 300 K prior to the TPR run, because α would otherwise be obscured by the tail of the methanol desorption.

Equation 2.24 in Section 2.8 allows to calculate the desorption energy, E_{des}, as a function of the temperature of maximum desorption, T_{max}, and of the heating rate, $\frac{dT}{dt}$. Using $\frac{dT}{dt} = 5$ Ks^{-1} and $\nu = 10^{13}$ s^{-1}, the desorption energies corresponding to the α, β and γ peak are 86 kJ mol^{-1}, 131 kJ mol^{-1}, and 155 kJ mol^{-1}, respectively.

Mullins and co-workers investigated methanol adsorption on thin ceria films [188]. If these films were fully oxidized, formaldehyde formed from methanol desorbed at $\sim$ 560 K. Feng and Vohs found formaldehyde desorbing at 595 K on high-surface area, polycrystalline ceria [286]. This is equivalent to the γ peak presented in this work, which appears at 580 K to 600 K. The β peak, on the other hand, can only be related to literature results concerning vanadia supported on substrates other than ceria. As mentioned above, a similar behavior is observed for vanadia supported on titania. Wang and Madix studied formaldehyde formation on vanadia supported on a $TiO_2(110)$ single crystal. Vanadia was prepared by chemical vapor deposition, CVD, of H_2O and $VOCl_3$ [265]. Similar to the present work, a desorption feature was found at $\sim$ 500 K. Moreover, while Wong *et al.* found $TiO_2(110)$ to be inert in this respect, the addition of one monolayer of vanadia activated the formation of formaldehyde, which desorbed at above 600 K [270]. Interestingly, the vanadia multilayer was inactive again. Subsequently, a more detailed study was published by the same research group (Wong *et al.* [229]), which deals with the oxidation state of the vanadia deposits, and how it relates to the

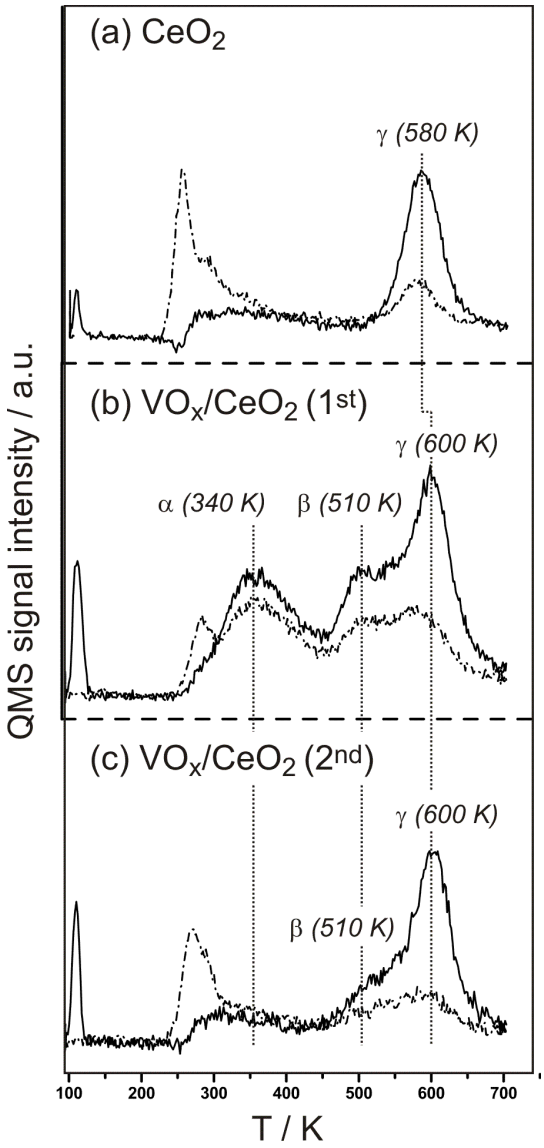

Figure 5.12: Methanol TPR from (a) CeO_2; (b) first run from VO_x/CeO_2 (0.3 Å vanadium); (c) second run from VO_x/CeO_2 (Å vanadium) (solid lines: formaldehyde; dashed lines: methanol).

reactivity. Formaldehyde desorption was discovered at $\sim$ 500 K $\pm$ 20 K, depending on the preparation procedure, which employed PVD as well as the CVD variant introduced by Wang and Madix. The desorption temperature of 500 K found by Wang and Madix as well as by Wong *et al.* coincides with the β peak in Figure 5.12. Vohs *et al.* studied methanol adsorption on vanadia spupported on single-crystalline and on polycrystalline ceria and found formaldehyde desorption at 540 K and 525 K, respectively [287].

The intensity distribution for α, β and γ in the first TPR from each respective sample is a function of the vanadia coverage. Figure 5.13 displays the spectra for 0.1, 0.3 and 0.7 Å. At 0.1 Å, only α and γ are detected. The intensity of γ is indistinguishable from the case of pristine ceria, and α is quite weak. For 0.3 Å, γ is still unchanged, but α has gained intensity, and β has started to grow in. At 0.7 Å, α is slightly weaker than at 0.3 Å, β is again stronger than in the previous spectrum, and γ has started to diminish.

The coverage-dependence of the three peaks is as follows: the intensity of γ stays constant at low coverages, but has started to decrease at 0.7 Å. The intensity of β appears to be a monotonic function of the vanadia coverage. Finally, α seems to have an intensity maximum at intermediate coverages such as 0.3 Å, but is less pronounced for coverages both higher and lower than this value. Since γ originates from ceria, it is assumed that only sufficiently high vanadia coverages will suppress it, but low coverages will not have a visible effect. The monotonic coverage-dependence of the intensity of β and, in particular, its absence at low coverages suggest a connection to a vanadia species that is typical for high coverages. Considering the structural results on ceria-supported vanadia presented in Section 5.4.1, the β reactivity should be related to larger aggregates of vanadia that contain V^{3+} and exhibit vanadyl groups with a stretching wavenumber in the range of 1025 cm^{-1} to 1045 cm^{-1}.

The fact that the intensity of α as a function of vanadia coverage has an apparent maximum indicates that there are two competitive effects that influence the extent of α reactivity. The intensity increases with increasing coverage in the low coverage range (below 0.3 Å), and then decreases for higher coverages (above 0.3 Å). If the range of low coverages (up to 0.3 Å V) is considered only, then the intensity of α appears to be a monotonic function of the vanadia coverage. There, vanadia is present as monomeric VO_4 species that contain V^{5+} and exhibit a vanadyl band at 1006 cm^{-1}, as discussed in Section 5.4.1. There, it is also outlined that a coverage of $\sim$ 0.3 Å vanadium marks the onset of the formation of larger vanadia particles, as judged by IRAS. Since each polymeric particle is an expansion of a monomeric one, the overall number of the latter must decrease with increasing coverage from that point onward. This corresponds exactly to the decrease of α intensity above

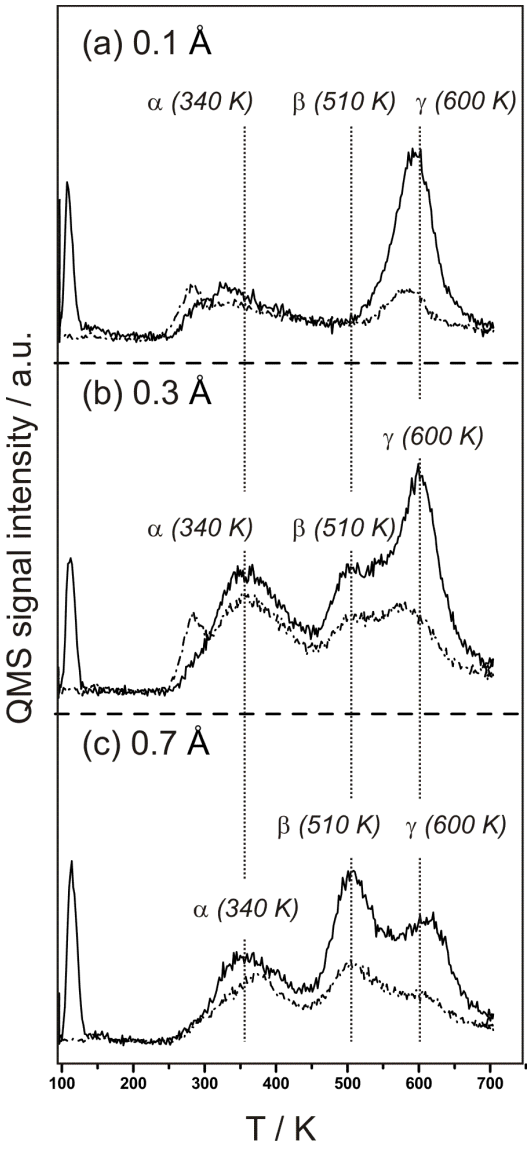

Figure 5.13: Methanol TPR (first run) from VO_x/CeO_2. (a) 0.1 Å vanadium; (b) 0.3 Å vanadium; (c) 0.7 Å vanadium (solid lines: formaldehyde; dashed lines: methanol).

0.3 Å. Therefore, the presence of α seems to be connected with the presence of monomeric and fully oxidized vanadia species, while the observation of β depends on polymeric vanadia, where vanadium is V^{3+} (see PE spectra in Figure 5.6).

Comparision with the findings of Wong *et al.* [229] reveals a difference in the relationship between the oxidation state of vanadium and the reactivity. Wong *et al.* observe a peak that coincides with β on a sample covered with a V_2O_5 monolayer. The presence of V^{5+} is attributed to the strong pre-oxidation ($\sim 10^{-3}$ mbar O_2) of the titania single crystal, which obviously increased its potential to oxidized vanadium. The ceria films, on the other hand, have an intrisically high oxidation potential, because of the oxygen storage capacity [65]. The coverage range used by Wong *et al.* would lead to the observation of the β peak in the present work, and indeed these authors report a formaldehyde TPR peak at $\sim$ 500 K. Apparently, fully oxidized and polymeric vanadia produce β. This suggests that the particle size is possibly the crucial parameter for the observation of α. On the other hand, Kim and Wachs found formaldehyde formation at 490 K in methanol TPR for VO_4/alumina [252]. The desorption temperature in their experiments is also similar to β, despite the presence of monomeric vanadia species. The α peak is not observed. It is possible that a combination of fully oxidized V^{5+} in a monomeric VO_4 species supported on CeO_2 is mandatory for the observation of the α state.

The temperature of 340 K, at which α is observed, is unusually low. A synopsis of the above literature examples for the conversion of adsorbed to methanol to formaldehyde reveals 490 K as the lowest desorption temperature. This suggests that a strong oxidant is needed for low temperature reactivity to occur. The IRAS results in Section 5.4.1 for deposition of small amounts of vanadium in 10^{-7} mbar O_2 include a band between 980 cm^{-1} and 990 cm^{-1}, for which the most plausible explanation is the presence of a peroxo group. The observation of this IR band and of the α peak require the same set of parameters (low vanadia coverage, deposition in O_2 at 100 K). Such a peroxo species would be a logical candidate for the oxidant responsible for the oxidation of methanol at a temperature as low as 340 K. This assumption is supported by Figure 5.23 (a), where it is shown that methanol adsorption is capable of removing the IR band at 984 cm^{-1}. It may be speculated that peroxo and methanol form the precursor of formaldehyde desorbing at 340 K. IRAS data shown in Figure 5.23 (a), where the tentative peroxo band is consumed by methanol adsorption, corroborate this assumption.

As stated previously, the sample was flashed to 300 K after methanol adsorption at 100 K, in order to remove unreacted methanol. Since this flash could induce structural changes, the influence was checked by the adsorp-

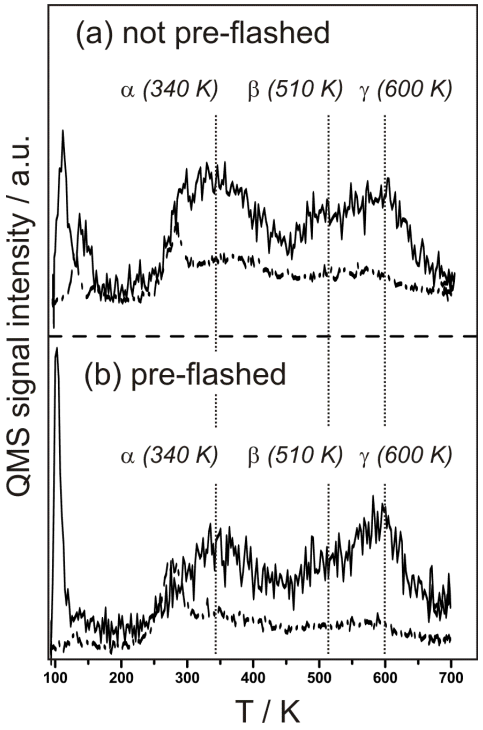

Figure 5.14: Methanol TPR from 0.2 Å VO_x/CeO_2. (a) as-prepared sample; (b) sample pre-flashed to 300 K prior to methanol adsorption (solid lines: formaldehyde; dashed lines: methanol).

tion of smaller amounts of methanol, which were calibrated by reducing the methanol dose, until the tail of the desorption feature between 250 K and 300 K (see Figure 5.12) was no longer observed. In this case, the α peak would not be obscured, given it is still present. For a sample of 0.2 Å vanadium that had not been pre-flashed to 300 K (Figure 5.14 (a)), all three TPR features are observed. Hence, it is concluded that neither originates from a process that is specifically linked to pre-flashing to 300 K. Moreover, the sample that did undergo a flash to 300 K prior to methanol adsorption also shows all three formaldehyde desorption peaks (Figure 5.14 (b)). Since the pre-flashing produced vandadyl groups in agreement with the results presented in Figure 5.9, it is additionally concluded that the presence of a V=O termination does not visibly hamper the reactivity. The interaction of adsorbed methanol with vanadyl groups is discussed below in more detail (see Figure 5.23).

More insight into the reactivity of ceria-supported vanadia is gained by comparison with results for vanadium deposition in UHV. Figure 5.15 (a)

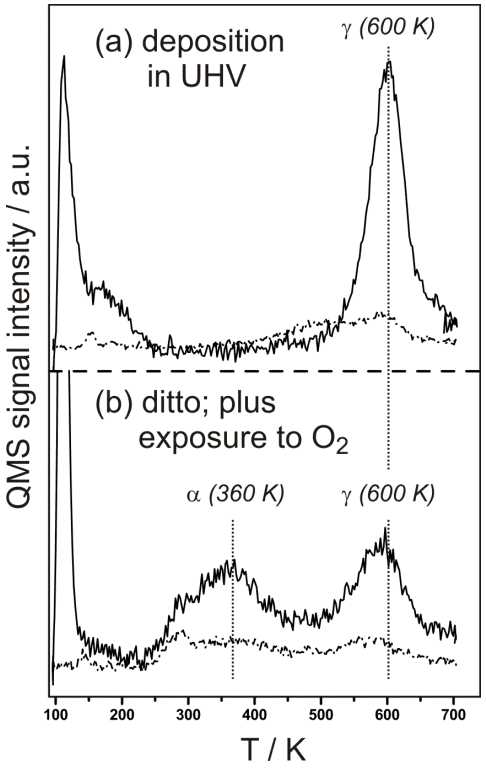

Figure 5.15: Methanol TPR from 0.2 Å vanadium deposited in UHV. (a) as-prepared sample; (b) sample exposed to 10^{-7} mbar O_2 prior to methanol adsorption (solid lines: formaldehyde; dashed lines: methanol).

shows the TPR spectrum taken after the deposition of 0.2 Å vanadium at 100 K in UHV. The sample was subsequently exposed to the equivalent of a monolayer of methanol, and the desorption of methanol and formaldehyde were monitored. Contrary to the deposition of vanadium in oxygen, neither β nor α reactivity could be observed here. The spectrum is dominated by a γ peak (related to ceria), which is the only formaldehyde desorption feature. For comparison, an identical amount of vanadium was deposited in UHV again, but subsequently exposed to 10^{-7} mbar O_2 for 10 min at 100 K. Contrary to the case without this treatment, the α peak could be observed here, although at a slightly higher temperature. Since the two experiments were identical except for the treatment with O_2, it seems that the oxygen content of the VO_x particles is a crucial parameter.

The reaction of methanol to formaldehyde results in the loss of two hydrogen atoms, the further whereabouts of which are important for the understanding of the reaction mechanism. Section 5.1.3 provides several mech-

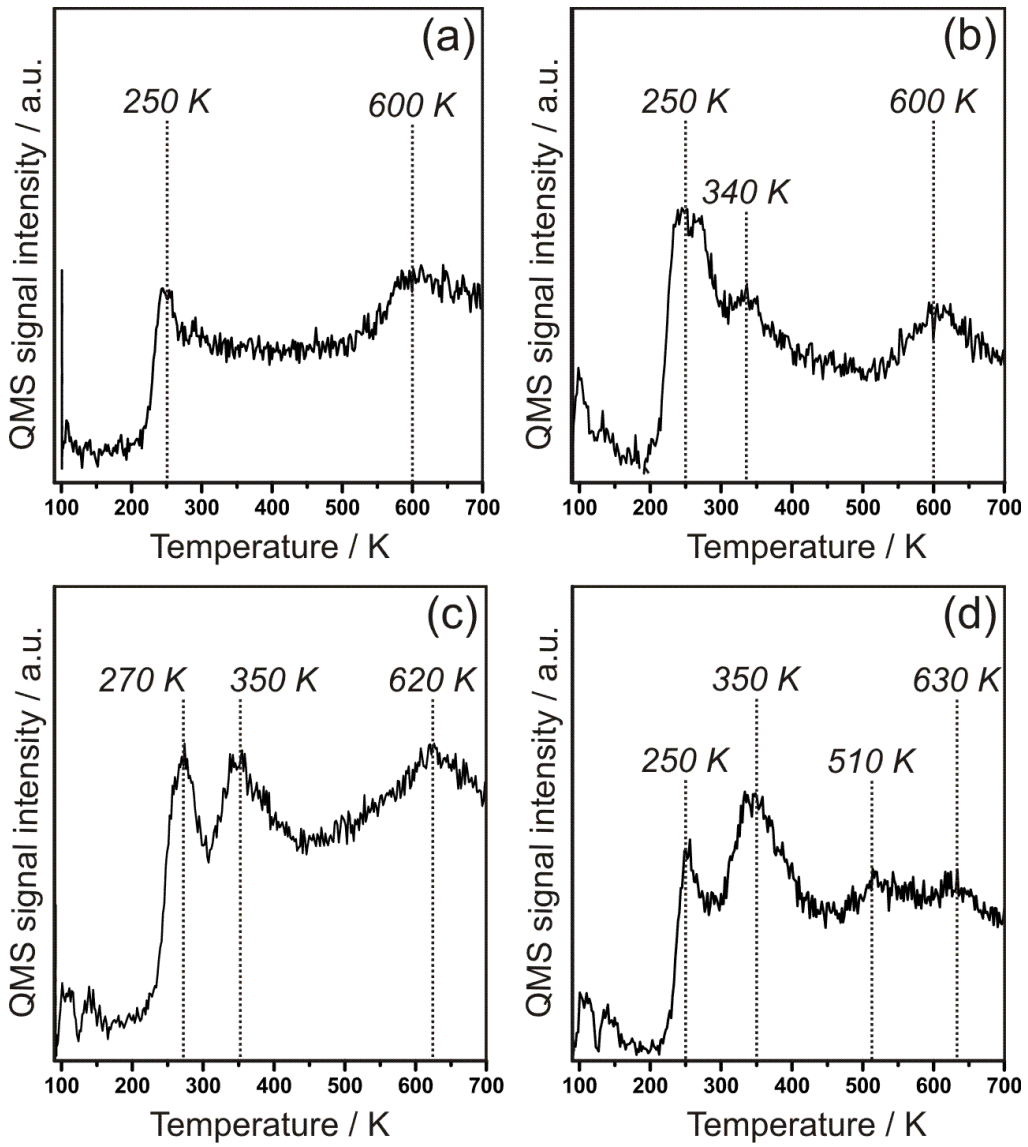

Figure 5.16: Water desorption in the first TPR runs from ceria and vanadia/ceria: (a) ceria, (b) vanadia/ceria (0.1 Å V), (c) vanadia/ceria (0.3 Å V), (d) vanadia/ceria (0.7 Å V).

anisms from the literature, which all consistently report the formation of water from the H atoms detached from methanol, and one surface O atom. Hence, it is no surprise that vanadium deposited in UHV does not exhibit the α and β formaldehyde peaks, as it is oxygen-deficient.

The water desorption during the first TPR runs is shown in Figure 5.16.

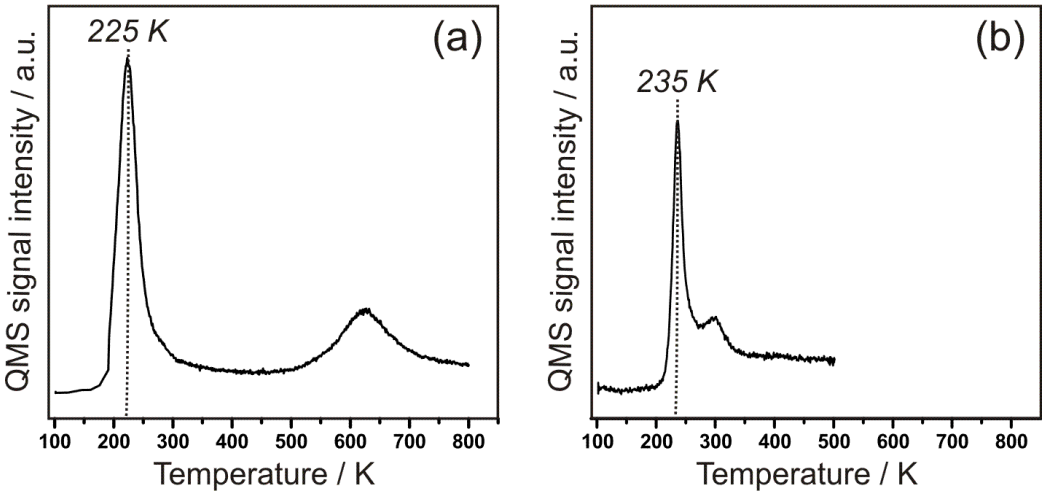

Figure 5.17: Other occurrences of water desorption from ceria, for comparison: (a) adsorption of $\sim$ 1 ML of methanol (*not* pre-flashed; only $\frac{\mathrm{m}}{\mathrm{z}} = 18$ is shown), (b) saturation dose of CO (no water dosed; only $\frac{\mathrm{m}}{\mathrm{z}} = 18$ is shown).

As outlined above, the samples were flashed to 300 K prior to the actual TPR. The onset of H_2O desorption is located at 250 K - 270 K. Note that beyond this temperature the background level of water remains higher than between 100 K and 200 K.

The low temperature peak is somewhat stronger for 0.1 and 0.3 Å V than for clean ceria and for 0.7 Å V. As the samples had been flashed to 300 K prior to the TPR, it is proximate that this feature is mainly due to re-adsorption. However, the complementary experiment, where the desorption of $\frac{\mathrm{m}}{\mathrm{z}} = 18$ after adsorption of $\sim$ 1 ML of methanol shows water desorption at $\sim$ 225 K (see Figure 5.17 (a)). In CO TPD experiments on CeO_2/Ru(0001, on the other hand, a desorption peak of water is observed at $\sim$ 235 K (see Figure 5.17 (b)), which can only be due to adsorption from the background. Romanyshyn *et al.* and Sturm *et al.* report the desorption of water at around 250 K from V_2O_3/Au(111) and V_2O_3/Au(111) films, respectively [263, 264]. There, it is related to the reaction from methanol to formaldehyde. Hence, there are at least three different possible origins for the low temperature water desorption from vanadia/ceria: byproduct of ceria-mediated formation of formaldehyde, byproduct of vanadia-mediated formation of formaldehyde, and adsorption from the background. The proximity in the desorption temperatures impedes a more detailed assignment.

It is striking that the remainder of the water desorption occurs at temperatures that are very similar to the α, β and γ peaks observed in Figure 5.13. This suggests that formaldehyde formation is coupled with the formation of water from recombining surface hydroxyl groups. As mentioned above, the background of water is relatively high beyond 250 K. To some extent, this is explicable by the fact that hydroxyl recombination can be diffusion-limited, as suggested by Kuhlenbeck [288]. Along these lines, it can also be speculated that the water desorption peaks do follow the temperatures of formaldehyde desorption, but not exactly the intensities.

IRAS

The TPR study was complemented by IRAS, in order to identify the surface intermediates of the formaldehyde formation. The vibrational modes of H_3COH expected in IR spectra are depicted in Figure 5.18, along with the wavenumbers of methanol measured in an Ar matrix at 15 K [289], which serves as a reference for the peak assignment in the IRAS data of the adsorption of methanol on the ceria films and the vanadia/ceria model catalyst.

Note that a Fermi resonance must be taken into account for the interpretation of the IR spectra of methanol. In general, Fermi resonances are observed, if vibrational transitions of the same symmetry coincidently possess a very similar transition energy [290]. In the case of H_3COH, the resonance occurs between fundamental ν(C/H) modes and overtones of δ(C/H) [291]. As a result, both the wavenumber and the intensity may be affected. It is generally accepted that the Fermi resonance peak in methanol appears at 2955 cm^{-1}, from a combination of the first overtone 2 δ_s(C/H) and the fundamental ν_s(C/H) [292]. The close proximity to ν_s(C/H) further complicates the interpretation.

Figure 5.19 shows the spectra of a stepwise increased exposure of ceria to methanol. One peak at $\sim$ 2800 cm^{-1} in part (a) and another peak at 1082 cm^{-1} in part (b) emerge almost simultaneously. Huberty and Madix report 2804 cm^{-1} for ν(C/H) of methoxy on Ni(100) [292], while Siokou and Nix found 2808 cm^{-1} on cerium oxide films [167]. Hence, the 2800 cm^{-1} band is understood as an indication for the presence of methoxy on ceria. The exact nature of this peak (ν_s(C/H), ν_s(C/H) or ν_a(C/H)) remains unclear. Its relevance for the present work is due to the fact that it allows to discriminate between methoxy and methanol.

It is concluded that the band at 1082 cm^{-1} represents the ν(C/O) mode of methoxy on ceria. The low conversion temperature (100 K) suggests a defect-mediated process. Another ν(C/O) band, which blueshifts from 1057 cm^{-1} to 1071 cm^{-1} with increasing methanol coverage, is attributed to ν(C/O)

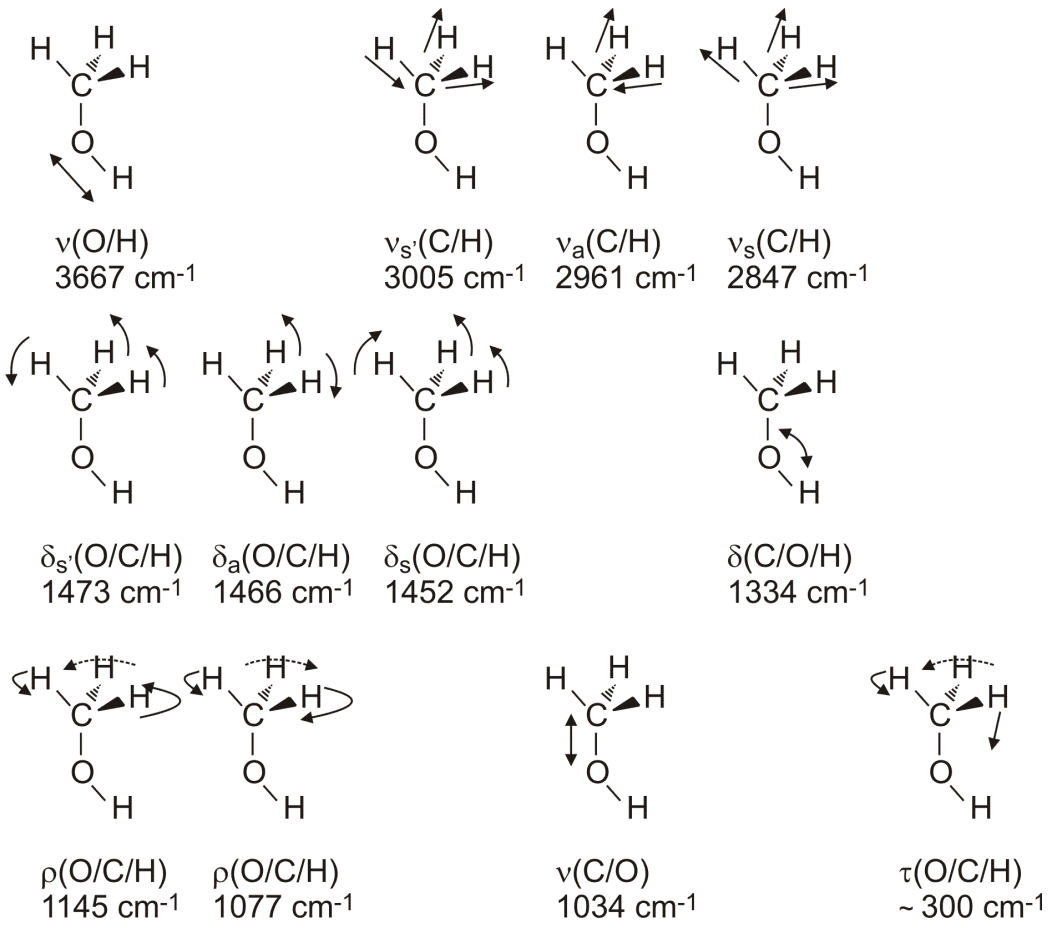

Figure 5.18: Vibrational modes of methanol found in IR spectra. The symbols designating the modes are defined in Section 2.6.1. The wavenumbers indicated refer to methanol in an Ar matrix [289].

of intact methanol. It seems that methoxy is forming, as long as the defect sites are accessible. Beyond this limit, methanol can adsorb only non-dissociatively at 100 K. The 1082 cm^{-1} band dominates the spectrum at low coverages, while it is obscured by the broad 1071 cm^{-1} at higher coverages. The 1082 cm^{-1} band, as long as it can be seen, does not shift its position, which is indicative for methoxy bound to defect sites that are far from each other, such that no intermolecular interaction between two methoxy species occurs. The coverage-sensitivity of the 1057-1072 cm^{-1} peak, on the other hand, is indicative for an intermolecular interaction in the methanol adsorbate phase. As outlined in Section 2.6.3, intermolecular dipole coupling will result in a blueshift of the corresponding IR band. Note that another band in the methanol ν(C/O) region evolved at $\sim$ 1050 cm^{-1} for very high coverages (not shown), which is ascribed to the multilayer of methanol.

After flashing this sample to 200 K, a band at 1112 cm^{-1} is observed next to the methanol band (1072 cm^{-1}). Another band appears at 1015 cm^{-1} after flashing to 250 K. At this temperature, the original methoxy band at 1082 cm^{-1} is no longer obscured by the methanol band, because the methanol band has vanished. The band at 1082 cm^{-1} disappears below 400 K. The species related to the 1112 cm^{-1} and the 1015 cm^{-1} band desorb between 400 K and 500 K, and between 500 K and 600 K, respectively. It is concluded that the latter are also reaction products of the adsorbed methanol, but their formation seems to be hindered by an activation barrier, which results in an elevated formation temperature. However, these species are also thermally more stable.

Tentative interpretations for the spectra of methanol on ceria at room temperature are found in the literature. Siokou and Nix ascribe three bands at 1105 cm^{-1}, 1058 cm^{-1} and 1027 cm^{-1}), which they measured after dosing methanol at 320 K to the surface of a CeO_2 film, to monodentate (linearly atop), bidentate (bridge-bonded) and tridentate (three-fold hollow-site) methoxy species, respectively [167]; i.e., similar to the states of CO adsorption reported by Blyholder [93]. The bi- and tridentate species are postulated to fill O vacancies, while the atop species is assumed to bind through the top O layer to Ce beneath. This assignment is in turn based on a study by Lavalley and co-workers, who observed the three bands at 1104 cm^{-1}, 1057 cm^{-1} and 1013 cm^{-1}, respectively [293–295]. The results in Figures 5.20 and 5.22 reveal close similarities with the literature. Yet the assignments by Lavalley and co-workers must be questioned, for two reasons.

First, a band at 1057 cm^{-1} has been identified as ν(C/O) of adsorbed methanol in the above discussion of Figure 5.19. In Figure 5.20, this band is not unambiguously observed, which corroborates the differing assignment. The acquisition of the TPR spectra in Figure 5.12 (a) - (c) as well as of the

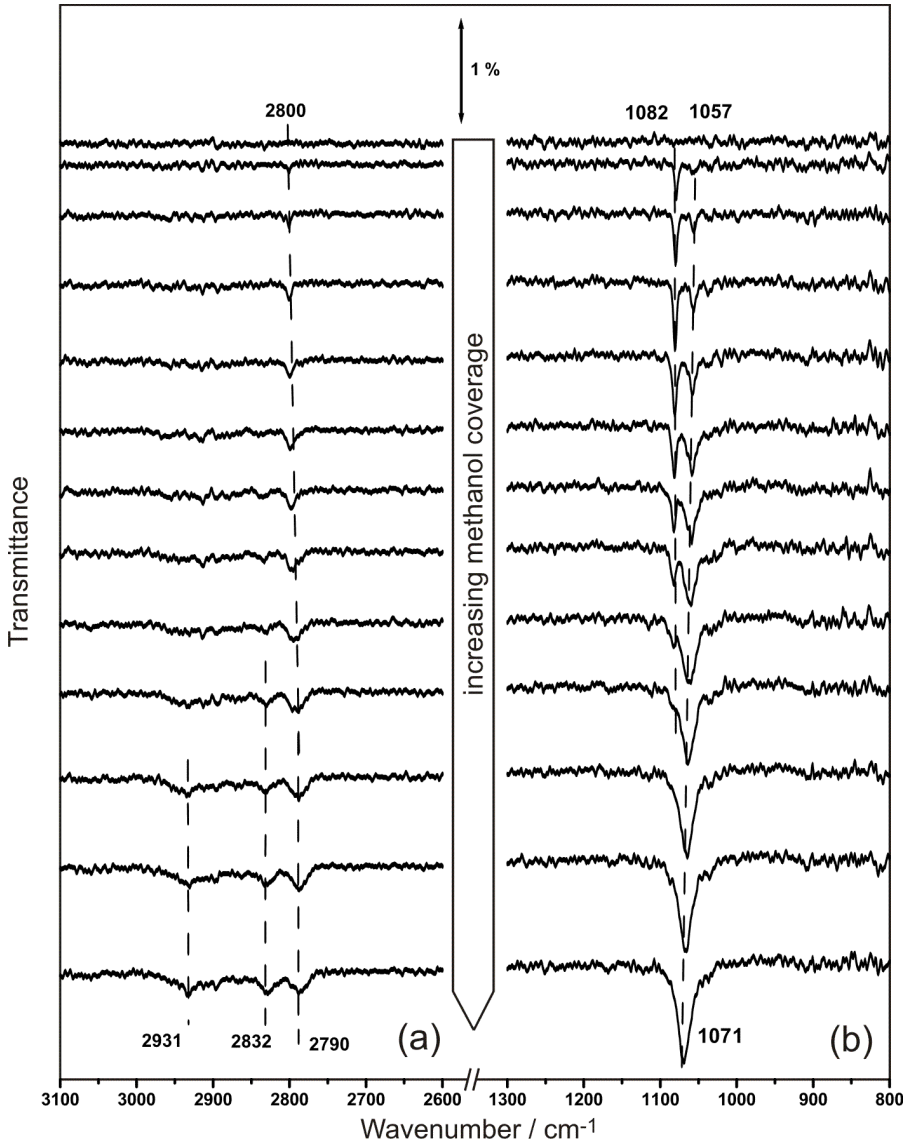

Figure 5.19: Stepwise adsorption of methanol on CeO_2/Ru(0001), studied with IRAS. (a) 3100 cm^{-1} - 2600 cm^{-1}, (b) 1300 cm^{-1} - 800 cm^{-1}. The methanol coverage is $\leq$ 1 ML for all spectra. The spectra are offset for clarity.

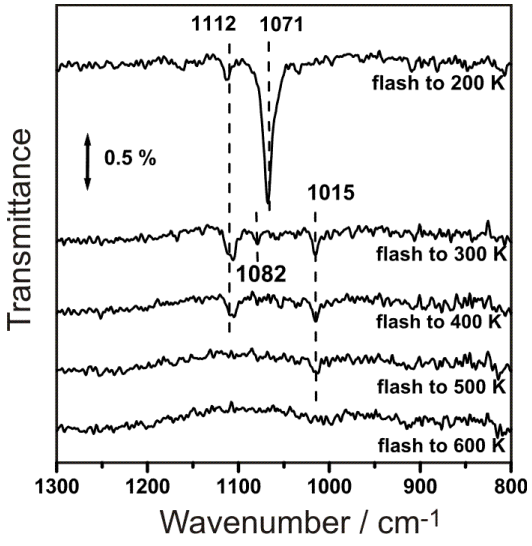

Figure 5.20: Flashing series of methanol on CeO_2/Ru(0001), studied with IRAS. The temperatures are indicated. The spectra are offset for clarity.

IRAS data in Figure 5.22 for clean ceria is preceded by flashing the sample to 300 K. Methanol desorption below this threshold is still observed in TPR, to various extents, which is attributed to re-adsorption after flashing to 300 K. Apparently, in the case of Figure 5.20, the extent of re-adsorption is below the detection limit.

Second, the band at 1082 cm^{-1} is the first to appear, when the ceria films are exposed to methanol at 100 K. Since this band is identified to represent a methoxy species, it would increase the total number of different methoxy species to four, if the literature assignments were correct. Yet a surface with hexagonal symmetry (as observed in Figure 5.5 (c)) cannot accomodate any entity with four different adsorption geometries.

Hence, the literature assignments available do not seem to be appropriate. Yet comparison with the IR spectra of other possible surface intermediates, such as CH_3, CO, CO_2, HCO (formyl), -OCH_2O- (dioxomethylene), CO_3^{2-}, $CO_2^{\delta-}$ (carboxylate), and $HCOO^-$ does not exhibit sufficient matching with the present data. It is concluded that the bands in question do represent three methoxy species (and methanol, at 1057 cm^{-1}), but not as proposed by Lavalley and co-workers. Possible assignments are presented below, among the discussion of Figure 5.22.

The TPR data in Figure 5.13 are acquired after adsorption of methanol onto pristine ceria and vanadia/ceria at three different coverages. The corresponding IR spectra are shown in Figure 5.21. After subsequent flashing to

300 K, the spectra in Figure 5.22 are obtained. The spectra of methanol on ceria are referenced to the clean ceria film, while all others are referenced to the respective as-prepared vanadia/ceria sample.

Figure 5.21 (a) shows four peaks, which are located at 2982 cm^{-1}, 2931 cm^{-1}, 2832 cm^{-1} and 2790 cm^{-1}, respectively. In agreement with the Ar matrix spectrum [289], the first three are assigned to $\nu_{s'}$(C/H), ν_a(C/H) or 2 δ_s(C/H) + ν_s(C/H) (the Fermi resonance), and ν_s(C/H), respectively. Note that the band at 2931 cm^{-1} is substantially broader than the other bands in Figure 5.21 (a), which could mean that it actually envelopes two unresolved peaks corresponding to the two given possible assignments. The fourth band, located at 2790 cm^{-1}, is understood as the redshifted 2800 cm^{-1} (i.e., $\nu_{(}$C/H) methoxy) band found in Figure 5.19.

The C/H bending modes give rise to a broad feature at $\sim$ 1500 cm^{-1} on the ceria films, as seen in Figure 5.21 (b). This band redshifts with increasing vanadia coverage, to $\sim$ 1470 cm^{-1} at 0.7 Å V. Additionally, the δ(C/O/H) mode is observed at 1328 cm^{-1}, but only in the presence of vanadia. The band constantly loses intensity with increasing vanadia coverage, and it is hardly discernible for 0.7 Å. This behavior is understood by taking into account Figure 5.21 (c). With increasing vanadia coverage, the large band at 1071 cm^{-1} shifts to 1057 cm^{-1}; i.e., similar to Figure 5.19 (b) from bottom to top. Presumably, the presence of vanadia on ceria spaces the molecules apart, which weakens the dipole coupling and thus reverses the shift. It is concluded that vanadia and methanol compete for the same sites on ceria.

Similar to this, the intensity loss at 2790 cm^{-1} as a function of the vanadia coverage indicates that vanadia also blocks the sites, on which this methoxy species is formed. The increase of the $\nu_{s'}$(C/H) band at 2982 cm^{-1} could be due to a change in the symmetry, possibly via the interaction of one methyl H atom with vanadia.

While the spectra in Figure 5.21 were taken after the adsorption of methanol, Figure 5.22 represents the situation after flashing the methanol-covered samples to 300 K to remove the overlayer of unreacted methanol. Based on the literature, the peak at 2800 cm^{-1} (which shifts to 2820 cm^{-1} for 0.7 Å VO_x/CeO_2) is assigned to ν_s(C/H) of methoxy [167, 292]. Since the methoxy band (2790 cm^{-1}) is redshifted with respect to the methanol band (2832 cm^{-1}) by $\sim$ 30 cm^{-1}, it is assumed that the same holds true for ν_a(C/H). Therefore, the second band at 2915 cm^{-1} is assigned to the same mode in a methoxy species. The feature at 2962 cm^{-1} found only intermittently at 0.3 Å V is considered to be artificial. The δ(C/H) and δ(O/H) region is now completely featureless. Note that an overall intensity loss is observed with increasing vanadia coverage.

The ν(C/O) region exhibits four peaks for ceria (1112 cm^{-1}, 1082 cm^{-1},

1057 cm^{-1}, and 1015 cm^{-1}). As discussed above, the 1057 cm^{-1} band is related to methanol, while the 1082 cm^{-1} band is due to an initial reaction of methanol with the ceria surface. As mentioned above, this reaction should be mediated by defects; e.g., step edges, kinks, or oxygen vacancies. For the case of 0.1 Å vanadium (deposited in 10^{-7} mbar O_2 at 100 K), the peak at 1082 cm^{-1} almost entirely vanished. As mentioned above, the responsible sites are most probably defects. Since the spectra are taken from two different ceria films, this intensity variation in Figure 5.19 and Figure 5.21, respectively, for identical preparations supports this assignment.

Attributing the bands at 1112 cm^{-1} and 1015 cm^{-1} is not straightforward. If their formation were a reversible process, the thermally most stable species would be populated first upon stepwise adsorption at low temperature and desorbs at the highest temperature. Yet methoxy is a reaction product, which renders the situation more complicated.

Upon vanadia deposition, the bands at 1112 cm^{-1} and 1015 cm^{-1} redshift. It seems that both shift by about equal amounts. For example, at 0.7 Å V in VO_x/CeO_2, the bands are shifted by 17 cm^{-1} and 14 cm^{-1}, respectively, by comparison to CeO_2. This is an indication that the two species have some structural similarities. As it is assumed that both are methoxy species, the similarities (and differences) lie in the sites they are adsorbed at. The formation of methoxy is already observed at 100 K (see Figure 5.19). Therefore, the higher formation temperatures of the species responsible for the bands at 1112 cm^{-1} and 1015 cm^{-1} can be explained by creating new adsorption sites, which are not present on the as-prepared surface. Modifying the morphology is understood as the creation of defects; however, these defects must be different from those that produce the 1082 cm^{-1} band. The nature of the defect sites and, moreover, how exactly they host their respective methoxy species, remains unclear. Nevertheless, it is possible to compare the desorption temperatures observed by TPR in Figure 5.12 (a) and by IRAS in Figure 5.20. Since the 1015 cm^{-1} is the last to vanish, between 500 K and 600 K, it is concluded that this is the one that is (primarily) responsible for the γ desorption peak of formaldehyde.

The additional features at 1040 cm^{-1} and 982 cm^{-1} in Figure 5.22 (b) can be assigned by comparison to methanol on silica-supported vanadia. For this case, Kaya reports one band at 985 cm^{-1} at low methanol exposure and another one at 1044 cm^{-1}, which becomes predominant with increasing methanol exposure, [296]. Based on the order of their appearance, it is concluded that the bands at 1040 cm^{-1} and 982 cm^{-1} represent ν(C/O) of methoxy and methanol, respectively, on vanadia.

The IRAS data of methanol adsorption on vanadia/ceria suggest a strong interaction between the vanadyl groups and methanol. Figure 5.23 (a) shows

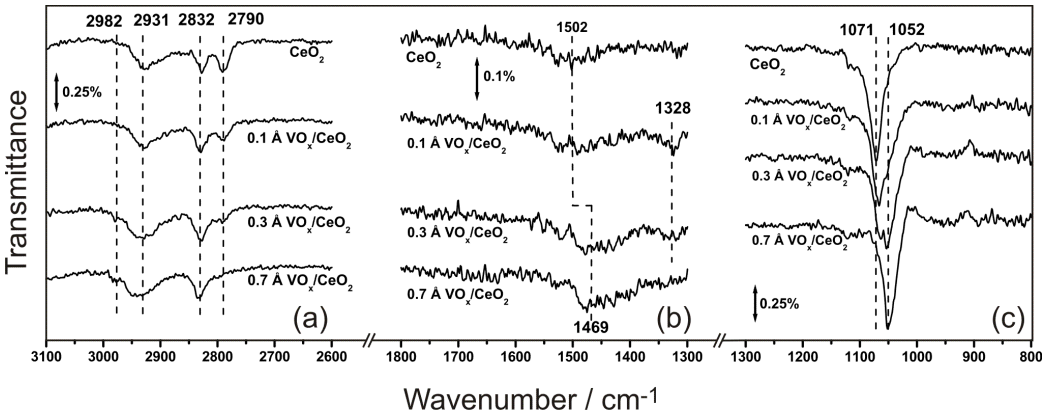

Figure 5.21: IRAS data of $\sim$ 1 ML of methanol adsorbed on CeO_2 and VO_x/CeO_2 at 100 K. (a) 3100 cm^{-1} - 2600 cm^{-1}; (b) 1800 cm^{-1} - 1300 cm^{-1}; (c) 1300 cm^{-1} - 800 cm^{-1}. (Note the change in the scale.) The spectra are offset for clarity.

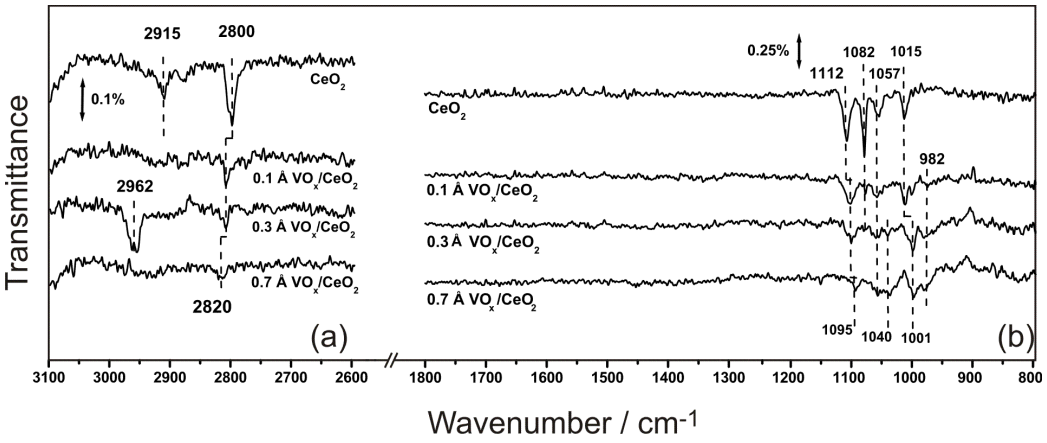

Figure 5.22: IRAS data of Figure 5.21, after a flash to 300 K. (a) 3100 cm^{-1} - 2600 cm^{-1}; (b) 1800 cm^{-1} - 950 cm^{-1}. (Note the change in the scale.) The spectra are offset for clarity.

the IR spectrum of vanadia/ceria (0.3 Å) flashed to 300 K (spectrum (i)). As expected from the results in Figure 5.9 (b), two bands at 1006 cm^{-1} and 989 cm^{-1} are observed. Subsequent methanol adsorption causes both to vanish (spectrum (ii)). The spectra presented in Figure 5.23 (b) were taken for another 0.3 Å V vanadia/ceria sample, (i) after the first TPR run, and (ii) after subsequent methanol re-adsorption at 100 K. Spectrum (i), which is referenced to the spectrum of the as-prepared vanadia/ceria sample, exhibits

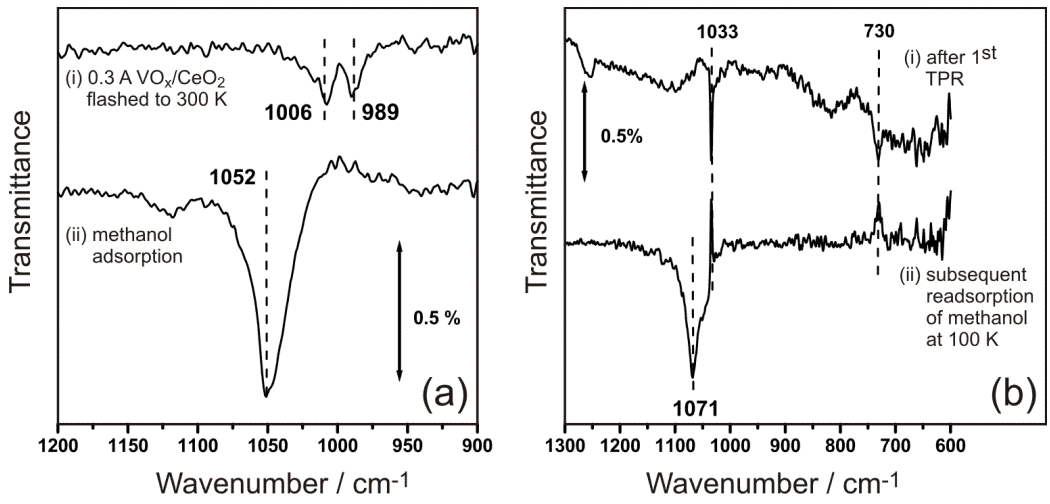

Figure 5.23: IRAS data of the interaction of methanol (a) with vanadyl groups formed by flashing the as-prepared sample to 300 K (0.3 Å, both spectra are referenced to as-prepared vanadia/ceria), (b) with vanadyl groups formed during the first TPR run (0.3 Å, spectrum (i) is referenced to the sample after the first TPR run, spectrum (ii) is referenced to spectrum (i)). The spectra are offset for clarity.

a band at 1033 cm^{-1} related to the stretching mode of the vanadyl groups, which were formed while heating the sample to 700 K in the TPR experiment. Re-adsorption of methanol at 100 K turned this band negative, as shown in spectrum (ii), which is referenced to spectrum (i).

As concluded above from Figure 5.22 (b), adsorption of methanol at 100 K inhibits the formation of vanadyl groups, since no such band could be observed after flashing the methanol-precovered sample to 300 K. The complementary experiment, where methanol is adsorbed on samples with vanadyl groups (1006 cm^{-1} and 1033 cm^{-1}), is even more conclusive (see Figure 5.23). Methanol adsorption interacts strongly with vanadyl groups, such that the IR intensity of their stretching mode disappears. This seems to hold true also for the band at 730 cm^{-1} (spectrum (ii) in Figure 5.23 (b)), which is associated with bridging O atoms on the particle surface, as well as for the band at 989 cm^{-1} (Figure 5.23 (a)), which is observed only after depsotion of vanadium in oxygen. Hence, methanol is capable of interacting with multiple oxygen species in ceria-supported vanadia. The loss of the vanadyl stretching band upon methanol adsorption is also observed by Kaya on silica-supported vanadia [296] and by Romanyshyn et al. on V_2O_3/Au(111) films [264].

5.5 Conclusions

PES results have shown that the cerium oxide film is able to oxidize low coverages of vanadium up to its highest oxidation state, V^{5+}. This is rather unusual, since most previously published results on vanadia suggest that it would favor the V^{3+} state in $\leq 10^{-6}$ mbar O_2). Alumina- and silica-supported vanadia were found to have V_2O_3 stoichiometry [149,151,152,225] under identical conditions, and Guimond *et al.* report the use of elevated O_2 pressures for the growth of V_2O_5 films on Au(111) [75].

IRAS results demonstrate the formation of vanadyl groups in a flashing series. Vanadyl formation is detected, even if vanadium had been deposited in UHV. In this case, the O atom of the V=O group must originate from the ceria support. The wavenumber of the vanadyl stretching mode of ceria-supported vanadia is apparently coverage-dependent. 1025 cm^{-1} to 1045 cm^{-1}, the range found for high vanadium coverages (0.7 Å or more) has been found on vanadia films and particles with V_2O_3 stoichiometry [89,136,137,149,151, 152, 225]. The deposition of low coverages (0.4 Å or less) gives rise to a vanadyl band slightly above 1000 cm^{-1}.

Combined STM/IRAS results demonstrated the connection of the band at 1006 cm^{-1} was shown to represent monomeric vanadia; i.e., orthovanadate, VO_4, species. This result agrees with the findings of Kim and Wachs [252], as well as with the group of Bañares [253] PES results indicate that vanadia in the low coverage range should contain fully oxidized V^{5+}. At elevated temperatures, however, such species sinter and produce larger particles containing V^{+3}, which exhibit the well-known vanadyl stretch at $\sim$ 1040 cm^{-1}.

TPR spectra of methanol on ceria-supported vanadia model catalysts reveal three formaldehyde desorption features, α (340 K), β (510 K) and γ (600 K). While the latter was shown to originate from the ceria support, the two former are related to the presence of vanadia. In particular, they are related to the vanadia coverage, which was shown to govern structural and electronic parameters, such as particle size and the oxidation state of vanadium. The β and γ peaks have been reported in the literature, while α is a novel observation in the oxidation of methanol over oxide catalysts.

As a consequence, the coverage-dependent distinction made for ceria-supported vanadia species is reflected by a difference in reactivity. Monomeric vanadia with a vanadyl stretch slightly above 1006 cm^{-1}, in which fully oxidized vanadium V^{5+} is present, is responsible for α reactivity, while β originates from larger particles, where vanadium is in the V^{3+} state and the vanadyl stretch gives rise to a band at 1030 cm^{-1} to 1040 cm^{-1}.

The IRAS study of methanol adsorption on ceria and vanadia/ceria suggests that the spectral assignments of Lavalley and co-workers for methoxy

species must be revisited. The observed four bands in the ν(C/O) region are more plausibly attributed to methoxy on inequivalent defect sites and to intact methanol.

Another important point is that a surface termination by vanadyl groups does not inhibit adsorption and reaction for ceria-supported vanadia. This is at variance with V_2O_3/Au(111) films, where the V atom of the vanadyl groups had to undergo a selective reduction, by which the O atom was lost, in order enable adsorption and subsequent reaction.

Chapter 6

Summary and Outlook

The present work continued the studies of model catalysts by means of the surface science approach, which is well-established in the Department of Chemical Physics at the Fritz Haber Institute, Berlin. Well-defined model systems containing the oxides of Group 5 metals niobium and vanadium were prepared and studied, including monolayer and multilayer niobia films, cobalt particles supported on niobia monolayer films and vanadia supported on ceria.

The structure of the niobia monolayer films grown on $Cu_3Au(100)$ was determined in a multi-method study. Exhibiting a Nb_2O_5 stoichiometry and hexagonal symmetry, it consists of niobium cations framed by one oxygen layer underneath and another one above. The outmost oxygen atoms sit in bridging positions between niobium. The multilayer Nb_2O_5 films, however, are terminated by niobyl groups; i.e., the outmost oxygen sits atop niobium. The monolayer and the multilayer films differ significantly in their symmetries.

Cobalt interacts strongly with the monolayer niobia films, for which the two-dimensional island growth is indicative. Moreover, oxidation of metallic cobalt at room temperature and even migration into the film at elevated temperature is observed, leading to a mixed phase. These findings indicate strong Co/niobia interaction, which is often observed in niobia-based catalysts.

Cerium oxide films grown on an Ru(0001) single crystal were used for the preparation of vanadia/ceria model catalysts. For deposition of vanadium in UHV, vanadyl groups are detected (after heating the sample to 500 K), which can only be explained by a migration of oxygen from the ceria lattice into vanadia. Vanadium deposited in O_2 formed fully oxidized and isolated VO_4 species at low coverage, while at higher coverages also larger particles consisting of V^{3+} are observed. The different species exhibit different stretching

frequencies for their vanadyl groups. Isolated vanadia (VO_4) species, prevalent at lower coverages, show a wavenumber as low as 1006 cm^{-1}, while at larger coverages a band at $\sim$ 1040 cm^{-1} is observed; i.e., similar to vanadia films.

The reactivity of the VO_x/CeO_2 model catalyst was studied in the reaction of methanol to formaldehyde, using TPR. Apart from the evidence for a reaction channel related to the ceria support, two more vanadia-related desorption features were found. The latter reflect the above-mentioned duality of the vanadia structure. In particular, the VO_4 monomers were found to be active already slightly above room temperature.

However, this species possesses limited thermal stability. It may well be that support effects reported for supported vanadia catalysts are intimately related to the stability of monomeric vanadia species.

Some open questions need still be addressed. The study of the niobia multilayer films is far from being complete. The transition from monolayer to multilayer needs a more thorough investigation. Moreover, the interaction of the multilayer films with metallic cobal deposits should be elucidated and compared to the present results. Nevertheless, first attempts in this direction showed a similar behavior. Further clarification is also needed for the detailed reaction mechanism of the oxidative dehydrogenation of methanol on ceria-supported vanadia. Finally, it is desirable to study the conversion of methanol to formaldehyde over these model systems at conditions that are closer to industrial applications.

List of Figures

1.1 Schematic of a typical surface science compatible model catalyst. 2
1.2 Periodic Table of Elements. 3
1.3 Activity of supported vanadia in methanol oxidation to formaldehyde as a function of the support [63]. 5

2.1 Schematic of the top chamber (top view). 8
2.2 Sample mount (front view). 9
2.3 Basic principles of LEED: Optics and Ewald sphere. 12
2.4 Basic principles of PES and AES. 14
2.5 Schematic of the six simple vibrational modes of a methylene group. 20
2.6 Schematic of the Infrared Reflection-Absorption Spectroscopy setup. 21
2.7 IRAS data. (a) interferogram (with center burst); (b) single channel spectrum (Fourier-transformed interferogram); (c) typical ratio of two single channel spectra. 22
2.8 Illustration of the Metal Surface Selection Rule. 25
2.9 Molecular orbitals of carbon monoxide [94]. 26
2.10 Chemical shifts of IR bands according to Blyholder. 26
2.11 Schematic of the VSI Delta 0.5 HREELS spectrometer [97]. . . 29
2.12 fragmentation pattern of (a) methanol and (b) formaldehyde at an ionization voltage of 70 V (from NIST webbook [104]) . 33

3.1 LEED patterns (70 eV) of (a) clean $Cu_3Au(100)$ and (b) monolayer $Nb_2O_5/Cu_3Au(100)$. 37
3.2 Schematic representation of the (2×7) coincidence structure formed between the square substrate lattice and the hexagonal oxide lattice. 38
3.3 STM of monolayer niobia films. 39
3.4 PES data of monolayer niobia films. 40

3.5 (a) Simulated and (b) experimental STM images of monolayer niobia films; (c) charge difference plot. 43
3.6 HREELS of monolayer $Nb_2O_5/Cu_3Au(100)$ 44
3.7 (a) CO TPD from monolayer niobia films; (b) and (c) CO IRAS on monolayer niobia films. 45
3.8 Structural model of monolayer $Nb_2O_5/Cu_3Au(100)$ films. . . . 48
3.9 LEED patterns (70 eV) of niobia films with increasing coverage, between 1 ML and 2 ML. 50
3.10 Niobia multilayer films grown on $Cu_3Au(100)$. (a) PES (at 0° with respect to surface normal) (data provided by D.E. Starr, spectra are offset for clarity); (b) HREELS (spectra are normalized with respect to the elastic peak). 51
3.11 HREEL spectra of multilayer Nb_2O_5 films: reduction and subsequent oxidation. 53
3.12 STM images of Co deposited on monolayer Nb_2O_5 films at 300 K. 55
3.13 CO TPD+IRAS from cobalt on monolayer Nb_2O_5 films. . . . 57
3.14 PES of cobalt on monolayer niobia films. 59

4.1 (a) - (e) STM images of niobia/alumina as function of niobia coverage. (f) Particle height and particle density as functions of niobia coverage. 63
4.2 IRAS of niobia/alumina. (a) dependence of the phonons on the niobia coverage, (b) dependence of CO adsorption on the niobia coverage. 65
4.3 STM images showing the thermal stability of niobia/alumina. 67
4.4 STM images following the removal and restoration of niobyl groups. 68
4.5 IRAS data of the removal and restoration of niobyl groups. . . 69

5.1 Decay routes of surface methoxy species. 75
5.2 (a) LEED and (b) STM of the ceria films. 80
5.3 PE spectra of the ceria films in the Ce 3*d* range. 81
5.4 IRAS data of $CeO_2/Ru(0001)$. (a) CO adsorption; (b) phonon range; (c) CO adsorption on Ru and oxidized Ru for comparison. 82
5.5 STM data of ceria-supported vanadia ((a) - (c) $\sim$ 0.1 and (d) $\sim$ 0.2 Å). 84

5.6 PES data of ceria-supported vanadia (this work; solid line: 0.1 Å V, dashed line: 0.7 Å V, both deposited at 100 K in 10^{-7} mbar O_2), of V_2O_3 films [89] and V_2O_5 films [75] grown on Au(111), as well as of vanadia supported on alumina [151] and silica [225]. The spectra are offset for clarity. 85
5.7 Phonon spectra (IRAS) taken after deposition of 2.0 Å vanadium in 10^{-7} mbar O_2 at 300 K and after flashing in UHV to 500 K, 700 K, 900 K. 87
5.8 Phonon spectra (IRAS) taken after deposition of 0.4 Å vanadium in 10^{-7} mbar O_2 at 300 K and after flashing in UHV to 500 K, 700 K, 900 K. 88
5.9 IRAS data of deposition of (a) 0.1, (b) 0.3 and (c) 0.7 Å vanadium in 10^{-7} mbar O_2 at 100 K, respectively. Each sample was subsequently flashed to 300 K, 500 K, 700 K and 900 K. . . . 90
5.10 IRAS data of deposition of (a) 0.1, (b) 0.3 and (c) 0.7 Å vanadium in UHV at 100 K, respectively. Each sample was subsequently flashed to 300 K, 500 K, 700 K and 900 K. 93
5.11 IRAS data in carbon monoxide C/O stretching region of (a) 0.2 Å vanadium deposited in UHV at 100 K and subsequently exposed O_2 and (b) 0.7 Å vanadium deposited in 10^{-7} mbar O_2. 94
5.12 Methanol TPR from (a) ceria, (b) ceria-supported vanadia, (c) ceria supported vanadia (repeated) 97
5.13 Methanol TPR from ceria-supported vanadia as function of vanadia coverage. 99
5.14 Methanol TPR without and with pre-flashing to 300 K. 101
5.15 Methanol TPR after vanadium deposition in UHV, without and with post-exposition to O_2. 102
5.16 Water desorption in the first TPR runs from ceria and vanadia/ceria. 103
5.17 Other occurrences of water desorption from ceria, for comparison. 104
5.18 Vibrational modes of methanol found in IR spectra. 106
5.19 Stepwise adsorption of methanol on CeO_2/Ru(0001), studied with IRAS. 108
5.20 Flashing series of methanol on CeO_2/Ru(0001), studied with IRAS. 109
5.21 IRAS data of $\sim$ 1 ML of methanol adsorbed on CeO_2 and VO_x/CeO_2 at 100 K. 112
5.22 IRAS data of Figure 5.21, after a flash to 300 K. 112
5.23 IRAS data of the interaction of methanol with vanadyl groups. 113

Bibliography

[1] G. Ertl, H. Knözinger, and J. Weitkamp, *Handbook of Heterogeneous Catalysis* (Wiley VCH, 1997).

[2] G. Ertl, H. Knözinger, and J. Weitkamp, *Environmental Catalysis* (Viley VCH, 1999).

[3] J. Thomas and W. Thomas, *Principles and Practice of Heterogeneos Catalysis* (Wiley-VCH, 1997).

[4] C. Satterfield, *Heterogeneous Catalysis in Practice* (McGraw-Hill, 1980).

[5] T. Risse, S. Shaikhutdinov, N. Nilius, M. Sterrer, and H.-J. Freund, Acc. Chem. Res. , in press (2008).

[6] H.-J. Freund, phys. stat. sol. (b) **192**, 407 (1995).

[7] S. Street, C. Xu, and D. Goodman, Annu. Rev. Phys. Chem. **48**, 43 (1997).

[8] C. Campbell, Surf. Sci. Rep. **27**, 1 (1997).

[9] C. Henry, Surf. Sci. Rep. **31**, 157 (1998).

[10] J. Niemantsverdriet, *Spectroscopy in Catalysis* (Wiley-VCH, 2000).

[11] I. Wachs, Y.-S. Chen, J.-M. Jehng, L. Briand, and T. Tanaka, Catal. Today **78**, 13 (2003).

[12] M. Ziolek, Catal. Today **78**, 47 (2003).

[13] K. Tanabe, Catal. Today **78**, 65 (2003).

[14] F. Mendes *et al.*, J. Phys. Chem. B **110**, 9155 (2006).

[15] F. Mendes, C. Perez, F. Noronha, and M. Schmal, Catal. Today **101**, 45 (2005).

[16] T. Iizuka, Y. Tanaka, and K. Tanabe, J. Mol. Catal. **17**, 381 (1982).

[17] E. Ko, J. Hupp, and N. Wagner, J. Catal. **86**, 315 (1984).

[18] I. Nowak and M. Ziolek, Chem. Rev. **99**, 3603 (1999).

[19] J.-M. Jehng and I. Wachs, Catal. Today **16**, 417 (1993).

[20] J.-M. Jehng and I. Wachs, Catal. Today **8**, 37 (1990).

[21] J.-M. Jehng and I. Wachs, J. Mol. Catal. **67**, 369 (1991).

[22] J.-M. Jehng and I. Wachs, J. Phys. Chem. **95**, 7373 (1991).

[23] M. Vuurman and I. Wachs, J. Phys. Chem. **96**, 5008 (1992).

[24] H.-C. Hu and I. Wachs, J. Phys. Chem. **99**, 10911 (1995).

[25] I. Wachs, J.-M. Jehng, G. deo, H.-C. Hu, and N. Arora, Catal. Today **28**, 199 (1996).

[26] I. Wachs, Catal. Today **27**, 437 (1996).

[27] L. Burcham, J. Datka, and I. Wachs, J. Phys. Chem. B **103**, 6015 (1999).

[28] D. Aranda, F. Noronha, A. Ordine, and M. Schmal, phys. stat. sol. (a) **173**, 109 (1999).

[29] E. Pereira, M. Pereira, Y. Lam, C. Perez, and M. Schmal, Appl. Catal. A **197**, 99 (2000).

[30] M. Schmal, D. Aranda, R. Soares, F. Noronha, and A. Frydman, Catal. Today **57**, 169 (2000).

[31] F. Noronha, D. Aranda, A. Ordine, and M. Schmal, Catal. Today **57**, 275 (2000).

[32] M. Pereira, E. Pereira, L. Lau, and M. Schmal, Catal. Today **57**, 291 (2000).

[33] F. Noronha *et al.*, Appl. Catal. A **210**, 275 (2001).

[34] V. Alegre, M. da Silva, and M. Schmal, Catal. Comm. **7**, 314 (2006).

[35] M. Schmal *et al.*, Catal. Today **118**, 392 (2006).

[36] T. Hoffer, S. Dobos, and L. Guczi, Catal. Today **16**, 435 (1993).

[37] T. Hoffer and L. Guczi, J. Mol. Catal. **70**, 85 (1991).

[38] L. Guczi, T. Hoffer, and Z. Zsoldos, J. Mol. Catal. **92**, 167 (1994).

[39] G. Bond and S. Flamerz-Tahir, Appl. Catal. A **71**, 1 (1991).

[40] G. Deo, I. Wachs, and J. Haber, Crit. Rev. Surf. Chem. **4**, 141 (1994).

[41] J. Hagen, *Industrial Catalysis: A Practical Approach* (Wiley-VCH, 1999).

[42] H. Rase, *Handbook of Commercial Catalysts* (CRC Press, New York, 2000).

[43] J. Haber, M. Witko, and R. Tokarz, Appl. Catal. A **157**, 3 (1997).

[44] S. Surnev, M. Ramsey, and F. Netzer, Prog. Surf. Sci. **73**, 117 (2003).

[45] G. Centi, Appl. Catal. A **147**, 267 (1996).

[46] I. Wachs and B. Weckhuysen, Appl. Catal. A **157**, 67 (1997).

[47] W. Hanke, R. Bienert, and H.-G. Jerschkewitz, Z. allg. anorg. Chem. **414**, 109 (1975).

[48] J. Miller and L. Lakshmi, Appl. Catal. A **190**, 197 (2000).

[49] R. Khaliullin and A. Bell, J. Phys. Chem. B **106**, 7832 (2002).

[50] S. Irusta, L. Cornaglia, I. Miro, and E. Lombardo, J. Catal. **156**, 167 (1995).

[51] J. Bronkema and A. Bell, J. Phys. Chem. C **111**, 420 (2007).

[52] P. Forzatti, E. Tronconi, A. Elmi, and G. Busca, Appl. Catal. A **157**, 387 (1997).

[53] C. Sorensen and R. Weber, J. Catal. **142**, 1 (1993).

[54] G. Deo and I. Wachs, J. Catal. **146**, 323 (1994).

[55] J.-M. Jehng, H. Hu, X. Gao, and I. Wachs, Catal. Today **28**, 335 (1996).

[56] G. Deo and I. Wachs, J. Catal. **129**, 307 (1991).

[57] C. Hetrick, J. Lichtenberger, and M. Amiridis, Appl. Catal. B **77**, 255 (2008).

[58] J. Liu *et al.*, Catal. Lett. **120**, 148 (2008).

[59] M. Martínez-Huerta, G. Deo, J. Fierro, and M. Bañares, J. Phys. Chem. C **111**, 18708 (2007).

[60] Y.-C. Lina, C.-H. Changa, C.-C. Chena, J.-M. Jehng, and S.-G. Shyu, Catal. Comm. **9**, 675 (2008).

[61] H. Römpp, J. Falbe, and M. Regitz, editors, *Römpp CD-ROM* (Thieme Verlag, 2004).

[62] F. Arena, F. Fusteri, and A. Parmaliana, Appl. Catal. A **176**, 189 (1999).

[63] I. Wachs, Catal. Today **100**, 79 (2005).

[64] A. Trovarelli, Cat. Rev. Sci. Eng. **38**, 439 (1996).

[65] A. Trovarelli, *Catalysis by Ceria and Related Materials* (Imperial College Press, 2002).

[66] J. Kašpar, P. Fornasiero, and M. Graziani, Catal. Today **50**, 285 (1999).

[67] A. Trovarelli, C. de Leitenburg, M. Boaro, and G. Dolcetti, Catal. Today **50**, 353 (1999).

[68] I. Wachs and R. Madix, Surf. Sci. **76**, 531 (1978).

[69] G. Reuss, W. Disteldorf, W. Grundler, and A. Hilt, *Ullmann's Encyclopedia of Industrial Chemistry (Vol. A11)* (Wiley VCH, 2002).

[70] M. Cozzolino, R. Tesser, M. Di Serio, P. D'Onofrio, and E. Santacesaria, Catal. Today **128**, 191 (2007).

[71] S. Wasmus and A. Küver, J. Electroanal. Chem. **461**, 14 (1999).

[72] P. Vollhardt and N. Schore, *Organische Chemie* (Wiley VCH, 1995).

[73] S. Schauermann, J. Hoffmann, V. Johánek, J. Hartmann, and J. Libuda, Phys. Chem. Chem. Phys. **4**, 3909 (2002).

[74] B. Brandt *et al.*, in preparation (2008).

[75] S. Guimond *et al.*, J. Phys. Chem. C , in press (2008).

[76] A. Uhl, J. Sainio, J. Lahtinen, S. Shaikhutdinov, and H.-J. Freund, Surf. Sci. **601**, 5605 (2007).

[77] D. Starr *et al.*, Surf. Sci. **599**, 14 (2005).

[78] P. Ewald, Z. Kristallogr. **56**, 129 (1921).

[79] A. Einstein, Annalen der Physik **132**, 17 (1905).

[80] D. Bonnell, *Scanning Tunneling Microscopy and Spectroscopy. Theory, Techniques and Applications* (Wiley-VCH, 1993).

[81] C. Chen, *Introduction to Scanning Tunneling Microscopy* (Oxford University Press, 1993).

[82] R. Wiesendanger, *Scanning Probe Microscopy and Spectroscopy* (Cambridge University Press, 1994).

[83] G. Binnig and H. Rohrer, Helv. Phys. Acta **55**, 726 (1982).

[84] G. Wedler, *Lehrbuch der Physikalischen Chemie* (Wiley-VCH, 2004).

[85] J. Tersoff and D. Hamann, Phys. Rev. Lett. **50**, 1998 (1983).

[86] J. Tersoff and D. Hamann, Phys. Rev. B **31**, 805 (1985).

[87] F. A. Cotton, *Chemical Applications of Group Theory* (Wiley VCH, 1990).

[88] K. Wolter *et al.*, Chem. Phys. Lett. **320**, 206 (2000).

[89] A. Dupuis, M. A. al-Haija, B. Richter, H. Kuhlenbeck, and H.-J. Freund, Surf. Sci. **539**, 99 (2003).

[90] C. Lemire *et al.*, Phys. Rev. Lett. **94**, 166101 (2005).

[91] M. Sock, S. Surnev, M. Ramsey, and F. Netzer, Top. Catal. **14**, 15 (2001).

[92] F. Hoffmann, Surf. Sci. Rep. **3**, 107 (1983).

[93] G. Blyholder, J. Phys. Chem. **68**, 2772 (1964).

[94] C. Elschenbroich and A. Salzer, *Organometallchemie* (Teubner Studienbücher, 1993).

[95] S. Efrima and H. Metiu, Surf. Sci. **109**, 109 (1981).

[96] P. Hollins, Surf. Sci. Rep. **16**, 53 (1992).

[97] *SPECS Delta 0.5 Ultimate Resolution Electron Energy Loss Spectrometer (version 02a).*

[98] E. Zaremba and W. Kohn, Phys. Rev. B **15**, 1769 (1977).

[99] P. Redhead, Vacuum **12**, 203 (1963).

[100] D. King, Surf. Sci. **47**, 384 (1975).

[101] E. Habenschaden and J. Küppers, Surf. Sci. **138**, L147 (1984).

[102] A. Jong and J. Niemantsverdriet, Surf. Sci. **233**, 355 (1990).

[103] K. Christmann, *Introduction to Surface Physical Chemistry (Topics in Physical Chemistry)* (Steinkopff-Verlag, 1991).

[104] http://webbook.nist.gov/chemistry/.

[105] H. Farrell and M. Strongin, Surf. Sci. **38**, 18 (1973).

[106] A. Darlinski and J. Halbritter, J. Vac. Sci. Technol. A **5**, 1235 (1987).

[107] I. Arfaoui, J. Cousty, and H. Safa, Phys. Rev. B **65**, 115413 (2002).

[108] I. Arfaoui, J. Cousty, and C. Guillot, Surf. Sci. **557**, 119 (2004).

[109] B. An, S. Fukuyama, K. Yokogawa, and M. Yoshimura, Phys. Rev. B **68**, 115423 (2003).

[110] C. Sügers, M. Schöck, and H. van Löhneysen, Surf. Sci. **471**, 209 (2001).

[111] M. Petrucci *et al.*, J. Appl. Phys. **63**, 900 (1998).

[112] L. Xie *et al.*, Surf. Sci. **320**, 62 (1994).

[113] T. Ushikubo *et al.*, Catal. Today **28**, 59 (1996).

[114] H. Niehus, R.-P. Blum, and D. Ahlberendt, phys. stat. sol. (a) **187**, 151 (2001).

[115] H. Niehus, R.-P. Blum, and D. Ahlberendt, Surf. Rev. Lett. **10**, 353 (2003).

[116] J. Middeke, R.-P. Blum, M. Hafemeister, and H. Niehus, Surf. Sci. **587**, 219 (2005).

[117] O. Warren and P. Thiel, J. Chem. Phys. **100**, 659 (1994).

[118] K. Kishi, Y. Hayakawa, and K. Fujiwara, Surf. Sci. **356**, 171 (1996).

[119] S. Shaikhutdinov, M. Ritter, and W. Weiss, Phys. Rev. B **62**, 7535 (2000).

[120] J. Halbritter, Appl. Phys. A **43**, 1 (1987).

[121] D. Morris *et al.*, Phys. Rev. B **61**, 13445 (2000).

[122] J. Mendialdua, R. Casanova, and Y. Barbaux, J. Electr. Spectr. Relat. Phenom. **71**, 249 (1995).

[123] P. Tasker, J. Phys. C **12**, 4977 (1979).

[124] H. Kuhlenbeck and H.-J. Freund, *Landolt-Börnstein NewSeries* (Springer Verlag, 2006).

[125] A. Cabrera and J. Espinosa-Gangas, J. Mater. Res. **17**, 2698 (2002).

[126] S. Vollmer, G. Witte, and C. Wöll, Catal. Lett. **77**, 97 (2001).

[127] J. Cook and E. McCash, Surf. Sci. **371**, 213 (1997).

[128] G. Graham, Surf. Sci. **187**, 490 (1987).

[129] F. Höbel, A. Bandara, G. Rupprechter, and H.-J. Freund, Surf. Sci. **600**, 963 (2006).

[130] M. Sierka, private communication (2007).

[131] S. Benedetti, H. Bénia, N. Nilius, S. Valeri, and H.-J. Freund, Chem. Phys. Lett. **430**, 330 (2006).

[132] R. Pittman and A. Bell, J. Phys. Chem. **97**, 12178 (1993).

[133] T. Ikeya and M. Senna, J. Non-Cryst. Solids **105**, 243 (1988).

[134] J.-M. Jehng and I. Wachs, Chem. Mater. **3**, 100 (1991).

[135] F. Gervais, Phys. Rev. B **23**, 6580 (1981).

[136] M. Abu al-Haija, S. Guimond, A. Uhl, H. Kuhlenbeck, and H.-J. Freund, Surf. Sci. **600**, 1040 (2006).

[137] M. Abu al-Haija *et al.*, Surf. Sci. **600**, 1497 (2006).

[138] T. Hill *et al.*, Chem. Phys. Lett. **292**, 524 (1998).

[139] A. Carlsson, M. Bäumer, T. Risse, and H.-J. Freund, J. Chem. Phys. **119**, 10885 (2003).

[140] T. Beutel, V. Siborov, B. Tesche, and E. Knözinger, J. Catal. **167**, 397 (1997).

[141] *XPS and AES Database*, Thermo Electr. Corp.

[142] G. Mestl and T. Srinivasan, Catal. Rev. Sci. Eng. **40**, 451 (1998).

[143] F. Roozeboom *et al.*, J. Phys. Chem. **84**, 2783 (1980).

[144] M. Nischimura, K. Asakura, and Y. Iwasawa, J. Chem. Soc. Chem. Commun. , 1660 (1986).

[145] Y.-C. Li *et al.*, Appl. Catal. A **272**, 305 (2004).

[146] Y.-C. Li *et al.*, Catal. Lett. **95**, 163 (2004).

[147] Y.-C. Li *et al.*, J. Mol. Catal. A **226**, 285 (2005).

[148] Y.-C. Li *et al.*, J. Catal. **241**, 173 (2006).

[149] N. Magg *et al.*, J. Catal. **226**, 88 (2004).

[150] J. van Lingen, O. Gijzeman, B. Weckhuysen, and J. van Lenthe, J. Catal. **239**, 34 (2006).

[151] N. Magg, J. B. Giorgi, T. Schröder, M. Bäumer, and H.-J. Freund, J. Phys. Chem. B, **106**, 8756 (2002).

[152] N. Magg *et al.*, J. Phys. Chem. B **107**, 9003 (2003).

[153] M. Bäumer and H.-J. Freund, Prog. Surf. Sci. **61**, 127 (1999).

[154] M. Heemeier *et al.*, Surf. Sci. **523**, 103 (2003).

[155] M. Frank *et al.*, Surf. Sci. **492**, 270 (2001).

[156] M. Bäumer, J. Biener, and R. Madix, Surf. Sci. **432**, 189 (1999).

[157] S. Shaikhutdinov *et al.*, Surf. Sci. **501**, 270 (2002).

[158] A. Pfau and K.-D. Schierbaum, Surf. Sci. **321**, 71 (1994).

[159] K. Fukui, Y. Namai, and Y. Iwasawa, Appl. Surf. Sci. **188**, 252 (2002).

[160] Y. Namai, K. Fukui, and Y. Iwasawa, Catal. Today **85**, 79 (2003).

[161] S. Gritschneder, Y. Namai, Y. Iwasawa, and M. Reichling, Nanotechn. **16**, S41 (2005).

[162] S. Gritschneder and M. Reichling, Nanotechn. **18**, 044024 (2007).

[163] S. Torbrügge, M. Reichling, A. Ishiyama, S. Morita, and Ó. Custance, Phys. Rev. Lett. **99**, 056101 (2007).

[164] J. Warren, X. Zhang, J. Andersen, and R. Lambert, Surf. Sci. **287-288**, 222 (1993).

[165] C. Hardacre, G. Roe, and R. Lambert, Surf. Sci. **326**, 1 (1995).

[166] M. Alexandrou and R. Nix, Surf. Sci. **321**, 47 (1994).

[167] A. Siokou and R. Nix, J. Phys. Chem. B **103**, 6984 (1999).

[168] S. Eck, C. Castellarin-Cudia, S. Surnev, M. Ramsey, and F. Netzer, Surf. Sci. **520**, 173 (2002).

[169] S. Eck *et al.*, Surf. Sci. **536**, 166 (2003).

[170] E. Wilson, W. Brown, and G. Thornton, Surf. Sci. **600**, 2555 (2006).

[171] K.-D. Schierbaum, Surf. Sci. **399**, 29 (1998).

[172] U. Berner *et al.*, Surf. Sci. **467**, 201 (2000).

[173] S. Overbury, D. Huntley, D. Mullins, K. Ailey, and P. Radulovic, J. Vac. Sci. Technol. A **15**, 1647 (1997).

[174] D. Mullins, S. Overbury, and D. Huntley, Surf. Sci. **409**, 307 (1998).

[175] D. Mullins, P. Radulovic, and S. Overbury, Surf. Sci. **429**, 186 (1999).

[176] S. Overbury, D. Mullins, D. Huntley, and L. Kundakovic, J. Catal. **186**, 296 (1999).

[177] D. Mullins and S. Overbury, J. Catal. **188**, 340 (1999).

[178] S. Overbury, D. Mullins, D. Huntley, and L. Kundakovic, J. Phys. Chem. B **103**, 11308 (1999).

[179] L. Kundakovic, D. Mullins, and S. Overbury, Surf. Sci. **457**, 51 (2000).

[180] D. Mullins, L. Kundakovic, and S. Overbury, J. Catal. **195**, 169 (2000).

[181] D. Mullins, J. Electr. Spectr. Relat. Phenom. **114-116**, 333 (2001).

[182] S. Overbury, D. Mullins, and L. Kundakovic, Surf. Sci. **470**, 243 (2001).

[183] D. Mullins and K. Zhang, J. Phys. Chem. B **105**, 1374 (2001).

[184] D. Mullins and S. Overbury, Surf. Sci. **511**, L293 (2002).

[185] D. Mullins and K. Zhang, Surf. Sci. **513**, 163 (2002).

[186] D. Mullins, Surf. Sci. **556**, 159 (2004).

[187] J. Zhou and D. Mullins, Surf. Sci. **600**, 1540 (2006).

[188] D. Mullins, M. Robbins, and J. Zhou, Surf. Sci. **600**, 1547 (2006).

[189] J. Zhou and D. Mullins, J. Phys. Chem. B **110**, 15994 (2006).

[190] S. Senanayake, J. Zhou, A. Baddorf, and D. Mullins, Surf. Sci. **601**, 3215 (2007).

[191] D. Mullins and T. McDonald, Surf. Sci. **601**, 4931 (2007).

[192] A. Beste, D. Mullins, S. Overbury, and R. Harrison, Surf. Sci. **602**, 162 (2008).

[193] D. Mullins and T. McDonald, Surf. Sci. **602**, 1280 (2008).

[194] J. Zhou, A. Baddorf, D. R. Mullins, and S. Overbury, J. Phys. Chem. C **112**, 9336 (2008).

[195] S. Senanayake and D. Mullins, J. Phys. Chem. C **112**, 9744 (2008).

[196] J.-L. Lu, H.-J. Gao, S. Shaikhutdinov, and H.-J. Freund, Surf. Sci. **600**, 5004 (2006).

[197] J.-L. Lu, H.-J. Gao, S. Shaikhutdinov, and H.-J. Freund, Catal. Lett. **114**, 8 (2006).

[198] Z.-X. Yang, T. Woo, M. Baudin, and K. Hermansson, J. Chem. Phys. **120**, 7741 (2004).

[199] B. Herschend, M. Baudin, and K. Hermansson, Surf. Sci. **599**, 173 (2005).

[200] C. Müller, C. Freysoldt, M. Baudin, and K. Hermansson, Chem. Phys. **318**, 180 (2005).

[201] B. Herschend, M. Baudin, and K. Hermansson, Chem. Phys. **328**, 345 (2006).

[202] Z.-X. Yang, T. Woo, and K. Hermansson, Surf. Sci. **600**, 4953 (2006).

[203] Z.-X. Yang, Z.-S. Lu, G.-X. Luo, and K. Hermansson, Phys. Lett. A **369**, 132 (2007).

[204] D. Sayle, S. Maicaneanu, and G. Watson, J. Am. Chem. Soc. **124**, 11429 (2002).

[205] M. Nolan, S. Parker, and G. Watson, Surf. Sci. **595**, 223 (2005).

[206] M. Nolan, S. Parker, and G. Watson, Surf. Sci. **600**, L175 (2006).

[207] M. Nolan and G. Watson, J. Phys. Chem. B **110**, 16600 (2006).

[208] M. Nolan, J. Fearon, and G. Watson, Solid State Ionics **177**, 3069 (2006).

[209] M. Sambi, M. Della Negra, and G. Granozzi, Surf. Sci. **470**, L116 (2000).

[210] M. Della Negra, M. Sambi, and G. Granozzi, Surf. Sci. **494**, 213 (2001).

[211] S. Agnoli *et al.*, Surf. Sci. **562**, 150 (2004).

[212] A. Vittadini, M. Casarin, M. Sambi, and A. Selloni, J. Phys. Chem. B **109**, 21766 (2005).

[213] C. Kolczewski, K. Hermann, S. Guimond, H. Kuhlenbeck, and H.-J. Freund, Surf. Sci. **601**, 5394 (2007).

[214] A. Bandara *et al.*, Topics Catal. **46**, 223 (2007).

[215] J. Schoiswohl *et al.*, Phys. Rev. B **69**, 155403 (2004).

[216] J. Schoiswohl *et al.*, Surf. Sci. **580**, 122 (2005).

[217] J. Schoiswohl *et al.*, Phys. Rev. B **71**, 165437 (2005).

[218] T. Todorova, M. Ganduglia-Pirovano, and J. Sauer, J. Phys. Chem. B **109**, 23523 (2005).

[219] V. Brázdová, M. Ganduglia-Pirovano, and J. Sauer, J. Phys. Chem. B **109**, 23532 (2005).

[220] T. Todorova, M. Ganduglia-Pirovano, and J. Sauer, J. Phys. Chem. C **111**, 5141 (2007).

[221] J. Biener *et al.*, Surf. Sci. **449**, 50 (2000).

[222] N. Magg *et al.*, J. Am. Chem. Soc. **126**, 3616 (2004).

[223] J. Biener, J. Wang, and R. Madix, Surf. Sci. **442**, 47 (1999).

[224] N. Price, J. Reitz, R. Madix, and E. Solomon, J. Electr. Spectr. Relat. Phenom. **98-99**, 257 (1999).

[225] S. Kaya *et al.*, J. Phys. Chem. C **111**, 5337 (2007).

[226] S. Guimond *et al.*, Topics Catal. **38**, 117 (2006).

[227] G. Wong and J. Vohs, Surf. Sci. **498**, 266 (2002).

[228] J. Biener, M. Bäumer, and R. Madix, Surf. Sci. **432**, 178 (1999).

[229] G. Wong, M. Concepcion, and J.M.Vohs, Surf. Sci. **526**, 211 (2003).

[230] Q.-G. Wang and R. Madix, Surf. Sci. **474**, L213 (2001).

[231] S. Chan, I. Wachs, L. Murrell, L. Wang, and W. Hall, J. Phys. Chem. **88**, 5831 (1984).

[232] I. Wachs, S. Chan, and R. Saleh, J. Catal. **91**, 366 (1985).

[233] G. Went, S. Ted Oyama, and A. Bell, J. Phys. Chem. **94**, 4240 (1990).

[234] C. Cristiani, P. Forzatti, and G. Busca, J. Catal. **116**, 586 (1989).

[235] I. Wachs, J. Catal. **124**, 570 (1990).

[236] G. Deo and I. Wachs, J. Phys. Chem. **95**, 5889 (1991).

[237] L. Le Costumer *et al.*, J. Phys. Chem. **92**, 1230 (1988).

[238] J.-M. Jehng, A. Turek, and I. Wachs, Appl. Catal. A **83**, 179 (1992).

[239] R. Kozlowski, R. Pettifer, and J. Thomas, J. Phys. Chem. **87**, 5176 (1983).

[240] J. Haber, A. Kozlowska, and R. Kozlowski, J. Catal. **102**, 52 (1986).

[241] H. Eckert and I. Wachs, J. Phys. Chem. **91**, 6796 (1989).

[242] G. Busca, G. Centi, L. Marchetti, and F. Trifiro, Langmuir **2**, 568 (1986).

[243] R. Brjorklund, C. Odenbrand, J. Brandin, L. Andersson, and B. Liedberg, J. Catal. **119**, 187 (1989).

[244] A. Turek, I. Wachs, and E. DeCanio, J. Phys. Chem. **96**, 5000 (1992).

[245] M. Vuurman, I. Wachs, and A. Hirt, J. Phys. Chem. **95**, 9928 (1991).

[246] G. Bond, J. Zurita, and S. Flamerz-Tahir, Appl. Catal. **27**, 353 (1986).

[247] Z. Liu, Z. Lin, H. Kan, and F. Li, Appl. Phys. A **45**, 159 (1988).

[248] X. Gao, S. Bare, J. Fierro, and I.E.Wachs, J. Phys. Chem. B **103**, 618 (1999).

[249] X. Gao and I. Wachs, J. Phys. Chem. B **104**, 1261 (2000).

[250] M. Bañares, M. Martínez-Huerta, X. Gao, J. Fierro, and I. Wachs, Catal. Today **61**, 295 (2000).

[251] A. Khodakov, B. Olthof, A. Bell, and E. Iglesia, J. Catal. **181**, 205 (1999).

[252] T. Kim and I. Wachs, J. Catal. **255**, 197 (2008).

[253] M. Bañares, private communication (2008).

[254] M. Barteau, Chem. Rev. **96**, 1413 (1996).

[255] K. Kim and M. Barteau, Surf. Sci. **223**, 13 (1989).

[256] P. Dilara and J. Vohs, Surf. Sci. **321**, 8 (1994).

[257] V. Gercher, D. Cox, and J. Themlin, Surf. Sci. **306**, 279 (1994).

[258] D. Cox and K. Schulz, J. Vac. Sci. Technol. A **8**, 2599 (1990).

[259] J. Tatibouet, Appl. Catal. A **148**, 213 (1997).

[260] J. Vohs and M. Barteau, Surf. Sci. **176**, 91 (1986).

[261] X. Peng and M. Barteau, Langmuir **7**, 1426 (1991).

[262] Y. Namai, K. Fukui, and Y. Iwasawa, Nanotechn. **15**, S49 (2004).

[263] J. Sturm, D. Göbke, H. Kuhlenbeck, and H.-J. Freund, in preparation (2008).

[264] Y. Romanyshyn *et al.*, in preparation (2008).

[265] Q.-G. Wang and R. Madix, Surf. Sci. **496**, 51 (2002).

[266] Y. Romanyshyn *et al.*, Topics Catal. , submitted (2008).

[267] W. Prandtl and L. Hess, Z. Anorg. Allg. Chem. **82**, 117 (1913).

[268] J. Bronkema, D. Leo, and A. Bell, J. Phys. Chem. C **111**, 14530 (2007).

[269] J. Bronkema and A. Bell, J. Phys. Chem. C **112**, 6404 (2008).

[270] G. Wong, D. Kragten, and J. Vohs, Surf. Sci. **452**, L293 (2000).

[271] D. Schröder *et al.*, Inorg. Chem. **43**, 1976 (2004).

[272] D. Schröder *et al.*, Inorg. Chem. **45**, 6235 (2006).

[273] M. Engeser, D. Schröder, and H. Schwarz, Chem. Eur. J. **11**, 5975 (2005).

[274] S. Feyel *et al.*, J. Phys. Chem. A **111**, 3278 (2007).

[275] S. Feyel *et al.*, ChemPhysChem **8**, 1640 (2007).

[276] R.-P. Blum, private communication (2006).

[277] A. Kotani, T. Jo, and J. Parlebas, Adv. Phys. **37**, 37 (1988).

[278] G. Herzberg, *Infrared and Raman Spectra of Polyatomic Molecules* (Van Nostrand Reinhold, 1945).

[279] J. Stubenrauch and J. Vohs, Catal. Lett. **47**, 21 (1997).

[280] V. Shapovalov and H. Metiu, J. Phys. Chem. C **111**, 14179 (2007).

[281] M. Martínez-Huerta *et al.*, J. Catal. **225**, 240 (2004).

[282] B. Tepper *et al.*, Surf. Sci. **496**, 64 (2002).

[283] H. Poelman, L. Fiermans, J. Vennik, and G. Dalmai, Solid State Commun. **84**, 811 (1992).

[284] K. Asmis, private communication (2008).

[285] B. Immaraporn *et al.*, Chem. Phys. Lett. **392**, 127 (2004).

[286] T. Feng and J. Vohs, J. Catal. **221**, 619 (2004).

[287] J. Vohs, T. Feng, and G. Wong, Catal. Today **85**, 303 (2003).

[288] H. Kuhlenbeck, private communication (2008).

[289] A. Serrallach, R. Meyer, and H. Günthard, J. Molec. Spec. **52**, 94 (1974).

[290] N. Colthup, L. Daly, and S. Wiberley, *Introduction to Infrared and Raman Spectroscopy* (Academic Press, 1975).

[291] J. Lavalley and N. Sheppard, Spectrochim. Acta **28A**, 2091 (1972).

[292] J. Huberty and R. Madix, Surf. Sci. **360**, 144 (1996).

[293] J. Lamotte, V. Morávek, M. Bensitel, and J. Lavalley, React. Kinet. Catal. Lett. **36**, 113 (1988).

[294] C. Binet, A. Jadi, and J.-C. Lavalley, J. Chim. Phys. **89**, 1441 (1992).

[295] A. Badri, C. Binet, and J.-C. Lavalley, J. Chem. Soc. Faraday Trans. **93**, 1159 (1997).

[296] S. Kaya, *Structural and Catalytic Investigations on Vanadium Oxide Nanoparticles Supported on Silica Films Grown on an Mo(112) Substrate*, PhD thesis, Humboldt-Universität Berlin, Mathematisch-Naturwissenschaftliche Fakultät I, 2007.

Abbreviations

Acronym	Full Name
A	Ampere
Å	Ångström
AES	Auger Electron Spectroscopy
AFM	Atomic Force Microscopy
a.m.u.	atomic mass unit
a.u.	arbitrary units
CVD	Chemical Vapor Deposition
DFT	Density Functional Theory
DMFC	Direct Methanol Fuel Cell
DRS	Diffuse Reflectance Spectroscopy
EXAFS	Extended X-ray Absorption Fine Structure
FT	Fourier Transform
FWHM	Full Width at Half Maximum
HOMO	Highest Occupied Molecular Orbital
HREELS	High Resolution Electron Energy Loss Spectroscopy
IR(R)AS	Infrared Reflection-Absorption Spectroscopy
L	Langmuir
LEED	Low Energy Electron Diffraction
m	meter
MBE	Molecular Beam Epitaxy
ML(E)	Monolayer (Equivalent)
NEXAFS	Near-Edge X-ray Absorption Fine Structure
nm	nanometer
NMR	Nuclear Magnetic Resonance
ODH	Oxidative Dehydrogenation
PES	Photoelectron Spectroscopy
PVD	Physical Vapor Deposition
RAIRS	Reflection/Absorption Infrared Spectroscopy
RHEED	Reflection High Energy Electron Diffraction

Acronym	**Full Name**
STM	Scanning Tunneling Microscopy
TDS	Thermal Desorption Spectroscopy
TPD	Temperature-Programmed Desorption
TPR	Temperature-Programmed Reaction
UHV	Ultrahigh Vacuum
UPS	Ultraviolet Photoelectron Spectroscopy
W	Watt
XAS	X-ray Absorption Spectroscopy
XPS	X-ray Photoelectron Spectroscopy

Acknowledgements

I would like to thank Prof. Hans-Joachim Freund for the opportunity to join his group at the Department of Chemical Physics of the Fritz Haber Institute, Berlin, and to work at the world-renowned FHI. I am very grateful that I was allowed to work with both highly talented colleagues and state-of-the-art scientific equipment under Prof. Freund's ever complaisant supervision.

I gratefully acknowledge that Prof. Helmut Schwarz agreed to act as the co-supervisor to my work, and that he even gave me the opportunity to practice scientific presenting on a regular basis within the framework of his group seminar. Similarly, I am thankful to Prof. Christian Limberg and Prof. Reinhard Schomäcker for being the external referee for my dissertation and the chairman of the defense examination committee, respectively.

I am particularly indebted to Dr. Shamil Shaikhutdinov, who was my scientific advisor on a daily basis throughout this work on behalf of Prof. Freund. His valuable guidance paved the way to a successful graduation. In short, Shamil's impact may be expressed by the following equation:

$$\hat{S}\ Alex = Dr.\ Alex$$

where $\hat{S}$ is the Shamiltonian operator, and *Dr.* is the final state.

I had the pleasure to collaborate with several colleagues during this work. Dr. Céline Lemire introduced me to the scientific equipment I had been entitled to use for several years. The acquisition of the IRAS and TPR data for the thin niobia films and the niobia-supported cobalt particles was done in a joint effort with Dr. Fabiana M.T. Mendes. Dr. David E. Starr contributed the STM and PES data of the same projects. Dr. Doron Lahav performed the computations on the monolayer niobia films. The STM images of alumina-supported niobia and of ceria-supported vanadia (higher coverage) were obtained together with Dr. Jani Sainio. Martin Baron and Dr. Darío J. Stacchiola assisted in the PES measurements on ceria and ceria-supported vanadia and contributed the related STM images (lower coverage). Dr. Heather L. Abbott helped with the IRAS and TPR experiments on this system. Moreover, I also fruitfully collaborated with Dr. Mohammad Abu

al-Haija on vanadia films and with Dr. Neetha Khan on alumina-supported PdAg particles, two projects that are not incorporated into my dissertation. Dr. Helmut Kuhlenbeck was very helpful in getting the HREEL spectrometer started. Uwe Härtel, Matthias Naschitzki and Klaus-Peter Vogelgesang must be named for tireless help and advice on technical issues. Several colleagues had the kindness of proof-reading this work. All of the above people made very important contributions to my thesis. Thank you!

Moreover, I have to thank all past and present members of FHI's CP department, for a truly feel-good ambience at work. In particular, this applies to my office mates, Dr. Mohammad Abu al-Haija, Dr. Tobias Schalow, Jan-Henrik Fischer and Wiebke Ludwig, in the order of (expected) graduation, to the above-mentioned collaborators, to the entire Structure and Reactivity group, and also to the various people I spent my lunch breaks with, and some of my free time as well. Thank you for countless conversations that were profound and funny alike. Thanks also for cheering me up whenever work was a drag!

A very special Thank You be addressed to my former advisor, Dr. David Lennon, who introduced me to the fascinating world of surface science and catalysis.

Last, but not least, I must thank my parents, who took care that I could enjoy an excellent education and have always encouraged me to pursue my dreams. I know I cannot take this for granted!

... Let's not forget the administration of Rheinland-Pfalz, who cut academic funding at the very moment when I meant to become a PhD student within their realm; thus being ultimately responsible that I was at the "Fritz", when Prof. Gerhard Ertl was awarded the Nobel prize in Chemistry. I will be eternally grateful!

Publikationen

Die folgenden Publikationen entstammen der vorliegenden Arbeit:

"Preparation and characterization of well-ordered, thin niobia films on a metal substrate", D.E. Starr, F.M.T. Mendes, J. Middeke, R.-P. Blum, H. Niehus, D. Lahav, S. Guimond, A. Uhl, T. Kluener, M. Schmal, H. Kuhlenbeck, S. Shaikhutdinov, and H.-J. Freund, Surf. Sci. **599**, 14 (2005).

"Strong metal support interaction on Co/niobia model catalysts", F.M.T. Mendes, A. Uhl, D.E. Starr, S. Guimond, M. Schmal, H. Kuhlenbeck, S. Shaikhutdinov, and H.-J. Freund, Catal. Lett. **111**, 35 (2006).

"Preparation and structure of alumina supported niobia model catalysts", A. Uhl, J. Sainio, J. Lahtinen, S. Shaikhutdinov, and H.-J. Freund, Surf. Sci. **601**, 5605 (2007).

"Linking the Structure and Reactivity of H_3COH Oxidative Dehydrogenation by Vanadia Particles Supported on Ceria Thin Films", A. Uhl, H.L. Abbott, M. Baron, D.J. Stacchiola, S. Shaikhutdinov, and H.-J. Freund, *in preparation*.

Ich erkläre hiermit, dass die Anmeldung der Promotionsabsicht ausschließlich an der Technischen Universität Berlin eingereicht wurde, und dort nur bei der Fakultät II (Mathematik und Naturwissenschaften).

Berlin, 15. August 2008

Erklärung an Eides statt

Ich versichere an Eides statt, dass ich die vorliegende Arbeit selbständig verfasst und nur die angegebenen Hilfmittel und Quellen benutzt habe.

Berlin, 15. August 2008